Coffin, M.F., Frey, F.A., Wallace, P.J., et al., 2000
Proceedings of the Ocean Drilling Program, Initial Reports Volume 183

8. SITE 1140[1]

Shipboard Scientific Party[2]

BACKGROUND AND OBJECTIVES

Site 1140 lies on the northernmost part of the Kerguelen Plateau, ~270 km north of the Kerguelen Archipelago (Fig. **F1**). Flanked to the north and east by Eocene and younger oceanic crust of the Australian-Antarctic Basin, and to the west by Cretaceous oceanic crust of the Crozet and Enderby basins, the northern Kerguelen Plateau (NKP) is believed to have formed since 40 Ma via Kerguelen hot spot magmatism (Royer and Sandwell, 1989; Royer and Coffin, 1992). The Kerguelen Archipelago is part of the NKP; its igneous rocks yield dates from 39 Ma to the Holocene (Nicolaysen et al., 1996, in press). However, submarine igneous basement of the NKP has never been sampled, so its age and composition, as well as its relationship to the central and southern plateau sectors and to Skiff and Elan Banks, are unknown. We located Site 1140 on *Marion Dufresne* multichannel seismic (MCS) line MD109-06 (Fig. **F2**). Site 1140 lies at a depth of 2394 m on the northern flank of the NKP. We chose this location as representative of the NKP on the basis of its relatively simple structural setting and thin sedimentary section (Fig. **F3**). The top of acoustic basement is flat lying, and overlying basement is a sediment sequence ~350 m thick. The boundary between the NKP and the Australia-Antarctic Basin lies ~5 km north of Site 1140 and offsets basement by ~400 m.

Summary of Objectives

The main objectives at this site were to

1. Characterize the petrography and compositions of the lavas;
2. Determine the age of the lavas, testing the hypothesis that the uppermost igneous basement of the NKP is ~40 Ma, the age of

F1. Satellite-derived free-air gravity map of the Kerguelen Plateau, **p. 36.**

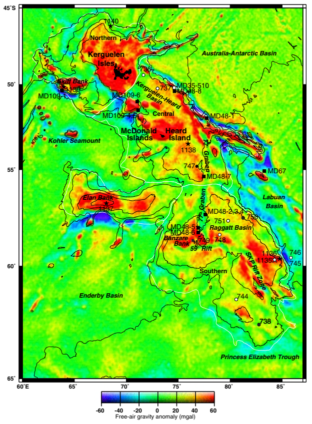

F2. Location of Site 1140 and site-survey data, **p. 38.**

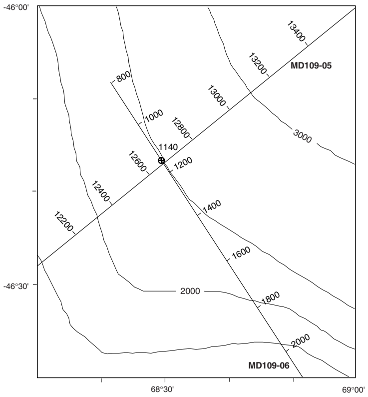

F3. *Marion Dufresne* MD109-06 multichannel seismic profile across Site 1140, **p. 39.**

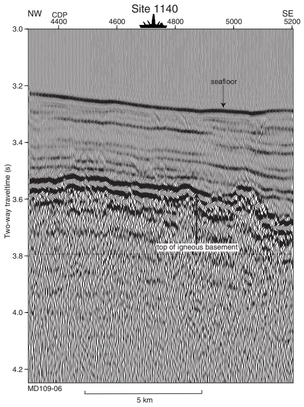

---

[1] Examples of how to reference the whole or part of this volume.
[2] Shipboard Scientific Party addresses.

Ms 183IR-108

the oldest known igneous rock from the Kerguelen Archipelago (Giret and Lameyre, 1983; Giret and Beaux, 1984), or younger;

3. Determine the physical characteristics of the lava flows;
4. Identify the environment of eruption (subaerial or submarine);
5. Obtain minimum estimates for the age of basement from overlying sediment;
6. Estimate the duration of possible subaerial and shallow marine environments from the sedimentary and igneous record;
7. Determine the facies of the seismic stratigraphic sequences;
8. Define the ages of seismic sequence boundaries; and
9. Determine the paleoceanographic history of this mid-latitude site.

OPERATIONS

Site 1140

The 550-km transit to Site 1140 was made in 27.5 hr at an average speed of 10.8 kt. The ship arrived on location the evening of 22 January 1999. Weather conditions were excellent upon arrival. At 2015 hr on 22 January 1999, we deployed a beacon on the precise Global Positioning System coordinates for Site 1140.

Hole 1140A

We spudded Hole 1140A at 0315 hr on 23 January 1999. The seafloor depth adjusted to the rig floor was estimated at 2406.0 m below rig floor (mbrf) based on a hard "tag" indication by the driller. This yields a seafloor depth of 2394.1 m below sea level. The 3.5-kHz precision depth recorder had indicated an adjusted seafloor depth of 2410.4 mbrf.

Continuous wireline coring proceeded in diatom-bearing nannofossil ooze and foraminifer-bearing nannofossil ooze through Core 183-1140A-14R to a depth of 131.4 meters below seafloor (mbsf). Recovery was problematic. Low circulation rates led to core jamming, and increased circulation rates tended to wash the material away. Recovery for this interval averaged 26.3%, and the average rate of penetration (ROP) was 33.8 m/hr. The formation then graded into nannofossil chalk to a depth of 237.3 mbsf. The average recovery improved through this interval to 65.2%, whereas the average ROP dropped to 24.7 m/hr. At the base of Core 183-1140A-25R, the first igneous rock was recovered. Based on the driller's measured depth, the top of igneous basement was estimated to be at ~234.0 mbsf. Coring continued through pillow basalts with glass rims to a total depth of 321.9 mbsf. The ROP varied from 0.9 to 4.9 m/hr. The average ROP in basement was 2.0 m/hr. Recovery in basement also varied considerably, ranging from 0% to 111%, and averaging 52.0%. Coring was terminated with the recovery of Core 183-1140A-37R from a depth of 321.9 mbsf ~88 m into basement. Coring was suspended to leave enough time for wireline logging and to depart the site no more than 1 day behind schedule. A total of 144.86 m of core was recovered at this site for an overall average of 45.0%. Recovery in basement was slightly better at 52.0%. Summaries of core numbers, depths, and recovery are given in Tables T1 and T2.

T1. Coring summary, p. 101.

T2. Expanded coring summary, p. 102.

During the coring operation, 20- to 25-bbl sepiolite mud sweeps were initiated when igneous rock was reached and were pumped during every core. A wiper trip was made to a depth of 90.2 mbsf and back to prepare the hole for wireline logging. No problems were encountered during the wiper trip, and no drag or overpull was noted by the driller. On bottom, the hole was swept with a 30-bbl sepiolite mud pill, and the bit was released. The hole was then displaced with sepiolite mud, and the end of the pipe was placed at a depth of 98.5 mbsf for logging.

The wireline logging program at this site was very successful. The first logging run included the dual induction–spherically focused resistivity tool (DITE-SFR), high-temperature lithodensity sonde (HLDS), accelerator porosity sonde (APS), hostile environment natural gamma-ray sonde (HNGS), and the Lamont-Doherty Earth Observatory (LDEO) temperature/acceleration/pressure tool (TAP). This run was successful reaching the bottom of the hole at ~322 mbsf. Because of downhole computer failure, the TAP data were lost. The next run was with the Formation MicroScanner (FMS) and long-spaced sonic (LSS) tools. A natural spectral gamma-ray tool (NGT) was included for calibrating between runs. This deployment was also successful in reaching the bottom of the hole. Two passes were made in basement (~88 m). The third run was with the well seismic tool (WST). This tool was also successful in reaching the bottom of the hole. Seismic check shots were done at 10-m intervals in basement, and two stations, at 149 and 109 mbsf, were completed in the sedimentary column. The logging data showed a maximum 5° hole deviation.

Contrary to our experience on earlier sites, the weather remained good for the Site 1140 logging operation. By 1815 hr on 27 January 1999, the logging line and sheaves were rigged down, and the remaining pipe was tripped out of the hole. The seafloor was cleared at 1845 hr. While the drill string was being tripped, the positioning beacon was released and recovered. The mechanical bit release reached the rig floor at 0320 hr. By 0330 hr, the ship was secured for transit, and we immediately got under way for Site 1141.

LITHOSTRATIGRAPHY

Introduction

Site 1140 is located north of the Kerguelen Archipelago in 2394 m of water on the northern edge of the Kerguelen Plateau. Hole 1140A was rotary cored continuously to a depth of 321.9 mbsf. Sediments were recovered from 0 to 234.52 mbsf. Pillow basalts and three minor sedimentary beds were recovered from the lower 87.38 m of the hole (Fig. F4; Table T3). The sedimentary section above igneous basement consists entirely of pelagic oozes and chalks and appears to rest unconformably on the underlying submarine basalt flows. We recognize only one sedimentary lithologic unit in the upper part (0–234.52 mbsf) of Hole 1140A. The basement volcanic rocks are designated lithologic Unit II and are subdivided into basement Units 1–6 (Fig. F4; Table T3) (see "Physical Volcanology," p. 12, "Igneous Petrology and Geochemistry," p. 16, and "Alteration and Weathering," p. 19, for description). Core recovery was generally poor throughout the sedimentary section of Hole 1140A, except for the topmost and lower portions (Fig. F4).

F4. Composite stratigraphic section for Site 1140, p. 40.

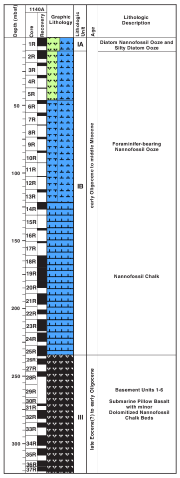

T3. Summary of lithologic units, p. 106.

Unit I

Interval: 183-1140A-1R-1, 0 cm, to 25R-5, 92 cm
Depth: 0 to 234.52 mbsf

Age: middle Miocene to early Oligocene

Unit I predominantly consists of light greenish gray foraminifer-bearing nannofossil ooze and nannofossil chalk. We divide this unit into two subunits (Subunits IA and IB) based on the presence of diatom ooze in the uppermost part of the unit (Fig. F4; Table T3).

Subunit IA (interval 183-1140A-1R-1, 0 cm, to 2R-1, 61 cm; 0–10.01 mbsf) consists of predominantly white diatom nannofossil ooze with interbeds of dark brown silty diatom ooze (intervals 183-1140A-1R-1, 0–25 cm and 40–65 cm; 1R-2, 33–89 cm; 1R-3, 73–80 cm; 2R-1, 0–9 cm), light brown silty foraminifer-bearing diatom ooze (intervals 183-1140A-1R-1, 25–40 cm; 1R-3, 80–89 cm; 1R-5, 0–10 cm) and yellowish brown nannofossil-bearing diatom ooze (interval 183-1140A-2R-1, 29–54 cm) of middle Miocene age (Fig. F4; Table T3). The $CaCO_3$ content is only 2 wt% in the dark brown layer in interval 183-1140A-1R-1, 0–25 cm, but ranges from 23 wt% to 53 wt% in the white layers below (Table T4). X-ray diffraction (XRD) analysis shows opal-A, feldspar, quartz, clay minerals, and maghemite as major components of the dark brown layers and calcite and opal-A with only traces of feldspar and clay minerals in the white layers. The organic carbon content varies from 0.03 wt% in Sample 183-1140A-1R-1, 11–12 cm, to 0.51 wt% in Sample 183-1140A-2R-1, 38–39 cm. Cores 183-1140A-1R and 2R contain a few rock pebbles up to 4 cm long scattered throughout the sediments. Much of the sediment in the top core is highly disturbed to soupy from drilling; thus, true thicknesses and stratigraphic positions of some individual beds are uncertain.

T4. XRD results, organic carbon, and carbonate contents, p. 107.

Subunit IB (interval 183-1140A-2R-1, 61 cm, to 25R-5, 92 cm; 10.01–234.52 mbsf) comprises most of the sedimentary section at Site 1140 and is predominantly light greenish gray foraminifer-bearing nannofossil ooze and nannofossil chalk of early Oligocene to middle Miocene age (Fig. F4; Table T3). The sediments become progressively stiffer downhole below ~75 mbsf (Core 183-1140A-9R) and are semilithified by 120 mbsf (Core 183-1140A-14R); below this depth the sediments are classified as chalk. The upper part of Subunit IB (interval 183-1140A-2R-1, 61 cm, to 5R-CC, 50 cm) is slightly burrowed light greenish gray diatom-bearing nannofossil ooze. White intervals are present at 183-1140A-20R-1, 34–51 cm, and 23R-1, 0–89 cm. Interval 183-1140A-23R-4, 0 cm, to 23R-CC, 29 cm, consists of white nannofossil chalk. A thin layer of brown diatom-bearing nannofossil chalk is present in interval 183-1140A-21R-1, 45–50 cm. A dark greenish gray volcanic ash layer, with vesicular basaltic glass shards, is present in interval 183-1140A-18R-6, 102–107 cm. The basal portion of Subunit IB (interval 183-1140A-24R-1, 0 cm, to 25R-5, 92 cm) is light pale brown because of disseminated yellow orange altered lithic grains (basalt?).

Clear rhombic dolomite crystals are disseminated throughout the sediments at the base of Subunit IB in Sections 183-1140A-25R-4 and 25R-5. XRD analyses indicate that the dolomite content increases from below detection limit in Section 183-1140A-24R-1 to about 5% in Section 25R-1, 10% in Sample 183-1140A-25R-5, 37–38 cm, and >95% in Sample 183-1140A-25R-5, 90–92 cm (Table T4). The position of the major dolomite XRD peak at 2.901 Å suggests an iron-rich composition.

The carbonate content in Subunit IB ranges from 51 wt% to 91 wt% $CaCO_3$ (average = 77%). The organic carbon content is very low (0.00 to 0.09 wt%) and averages 0.03 wt% (Table T4). XRD analyses show calcite and some opal-A throughout most of Subunit IB. Sample 183-1140A-

14R-1, 90–92 cm ($CaCO_3$ = 51 wt%) also contains some clay minerals and K-feldspar. Clay minerals were also detected in Core 183-1140A-25R-1 (Table T4).

Most sediments of Subunit IB are extensively burrowed; burrows include *Zoophycos* and *Chondrites*. Scattered black silt- and rare sand-sized particles of volcanic material are disseminated in some intervals. Steeply dipping faults are present in intervals 183-1140A-21R-1, 45–50 cm, and 23R-4, 110–125 cm. The presence of slickensides argues for faults, as opposed to drilling disturbance.

Unit II

Interval: 183-1140A-25R-5, 92 cm, to 37R-4, 35 cm
Depth: 234.52 to 321.90 mbsf
Age: early Oligocene or older

Lithologic Unit II is composed of pillow basalts with three thin sedimentary beds (Fig. F4; Table T3). Unit II is subdivided into six basement units, which are described in **"Physical Volcanology,"** p. 12, **"Igneous Petrology and Geochemistry,"** p. 16, and **"Alteration and Weathering,"** p. 19. The top of basement Unit 3 (interval 183-1140A-31R-1, 134–140 cm) is a thin bed of well burrowed greenish white nannofossil chalk of latest Eocene age.

Basement Unit 4 is a sedimentary bed (interval 183-1140A-32R-3, 41–115 cm). Intervals 183-1140A-32R-3, 41–91 cm, and 32R-3, 91–115 cm, at the top and bottom of this bed are composed of rusty brown to rusty orange dolomite, which consists of cemented medium sand-sized dolomite crystals. The dolomite content of these beds (Sample 183-1140A-32R-3, 83–84 cm) (Table T4) is close to 100%; no calcite was detected and clay is common. These dolomite beds are separated by well-burrowed, very pale brown dolomitic nannofossil chalk. Some burrows are filled with black manganese oxides. The top interval of basement Unit 6 (interval 183-1140A-34R-4, 0–6 cm) is composed of a thin bed of rusty brown dolomite similar in appearance to that of basement Unit 4.

Discussion

Submarine pillow basalts with thin interbeds of dolomitized nannofossil chalk in Unit II indicate that during the late Eocene(?) into the early Oligocene Site 1140 was in bathyal water depths and that pelagic deposition accompanied extrusion of the lava flows. Pelagic deposition in a bathyal environment continued uninterrupted from early Oligocene to at least middle Miocene time. The site most likely remained at bathyal depths until the present. A seismic profile across this drill site shows that a substantial portion of the uppermost strata of the seafloor has been removed by erosion.

BIOSTRATIGRAPHY

Site 1140, on the northern tip of the Kerguelen Plateau, penetrated 234.5 m of Miocene to lowermost Oligocene sediments similar to those encountered at Site 1139, plus a small amount of upper Eocene chalk intercalated with basalt. The major biostratigraphic objectives were to obtain minimum ages for basalts (presumed Cenozoic) and to determine the paleoceanographic history of the NKP.

Quaternary and upper Neogene sediments were not recovered. The uppermost 46.5 m consists of middle Miocene, diatom-bearing nannofossil ooze containing common planktonic foraminifers. Well-preserved diatoms and silicoflagellates provide age control in the diatom-bearing nannofossil ooze but are less abundant and highly fragmented in the lower Miocene and Oligocene chalks. Nannofossil and planktonic foraminifer assemblages in middle Miocene Sample 183-1140A-5R-CC contain species typical of lower latitudes that have not been previously found on the Kerguelen Plateau, indicating warmer water conditions on the NKP during parts of the middle Miocene. Unfortunately, recovery in this interval is very poor.

Beneath the light-colored ooze lies an apparently complete succession of lower middle Miocene to lower Oligocene foraminifer-bearing nannofossil ooze and chalk. Preservation of microfossils in these sediments is variable and diminishes downhole, particularly in dolomitized chalks in the vicinity of the sediment-basalt contact (Core 183-1140A-26R). Minor dolomitized chalk beds within submarine basalts at the bottom of Hole 1140A yielded nannofossils and microfossils of late Eocene age (planktonic foraminifer Zone AP12). Sediments directly above the basalts are early Oligocene in age. Paleomagnetic and biostratigraphic evidence suggest an unconformity in the basal Oligocene, but poor recovery of the uppermost basalts underlying the upper Eocene intercalated chalks reduces the possibility of confirming an unconformity or of identifying the Eocene/Oligocene boundary using paleomagnetic methods.

An age-depth summary based on examination of core-catcher samples shows a mean sedimentation rate for the section of 12 m/m.y (Fig. F5). We attribute higher sedimentation rates in chalks of similar age at Site 1139 (~16 m/m.y. in the Miocene and 20 m/m.y. in the Oligocene) to the input of significant amounts of clay derived from nearby Skiff Bank.

F5. Site 1140 age-depth plot, p. 41.

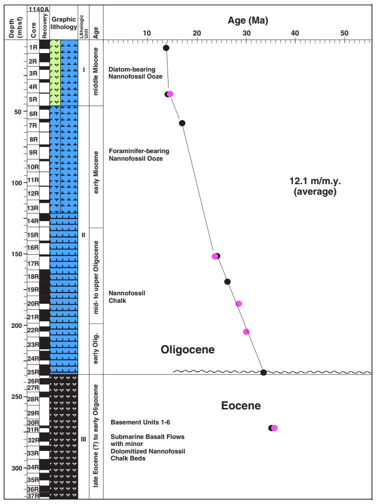

Calcareous Nannofossils and Diatoms

Nannofossils and diatoms were well to moderately well preserved throughout the sequence at Site 1140, except near the bottom, where they were absent in smear slides. Because the site was drilled at ~46°S at the northern edge of the Kerguelen Plateau, some nannofossil assemblages reflect a warmer environment than nannofossils of similar age recovered from more southerly domains of the plateau. For that reason, this is the first finding of some taxa on the Kerguelen Plateau. The downslope, downcurrent position of the site, however, made it more vulnerable to the deposition of reworked microfossils, a complication that has not been a factor at the previous sites drilled during Leg 183.

Sample 183-1140A-1R-CC contains common *Discoaster exilis,* few *Cyclicargolithus floridanus, Cyclicargolithus abisectus, Sphenolithus moriformis,* and *Calcidiscus leptoporus/macintyrei,* and abundant *Coccolithus pelagicus* and *Reticulofenestra perplexa*. The latter taxon constitutes ~90% of the assemblage. We assign the sample to the combined CN5a–CN3 Zone. Rare to few *Reticulofenestra bisecta* and *Chiasmolithus altus* are reworked from the Oligocene. This is the first record of *D. exilis* from the Kerguelen Plateau. Diatoms include *Denticulopsis hustedtii, Actinocyclus ingens,* and *Crucidenticula kanayae* but *Nitzschia denticuloides* is absent. These diatoms belong to the *D. hustedtii–Nitzschia grossepunctata* Zone (= 13.5–14 Ma or mid-middle Miocene in age). We also assigned the next three core-catcher samples (183-1140A-2R-CC through 4R-CC) to these zones. *Coccolithus pelagicus* constitutes 90% of the assemblage in Sample 183-1140A-3R-CC, a dominance reversal that is characteristic of assemblage changes induced by climatic/paleoceanographic cycles in this region (Wei and Wise, 1992). Sample 183-1140A-4R-CC contains abundant *D. hustedtii* and the silicoflagellates *Bachmannocena paulschulzii* and *B.* sp. cf. *B. diadon.*

Sample 183-1140A-5R-CC contains few *D. exilis* and abundant *D. veriabilis,* some of which are overgrown. As a group, discoasters, like sphenoliths, prefer warmer waters. No *D. hustedtii* are present among the diatoms, but *A. ingens* v. *nodus* is, rendering an age assignment to the zone of the same name (14.18 Ma).

The warm water–loving *Sphenolithus heteromorphus,* another nannofossil observed for the first time on the plateau, is common in Sample 183-1140A-6-CC; it ranges from Zones CN4 to CN3 of the early middle Miocene. *Helicosphaera granulata* is rare, and *Discoaster variabilis* exhibit strong overgrowths, causing it to resemble *Discoaster deflandrei.* Among the diatoms, we found rare *Eucampia antarctica* and *Coscinodiscus lewisianus.* Sample 183-1140A-7-CC exhibits a similar assemblage, except *S. heteromorphus* is absent. *S. moriformis* is common and we noted *C. kanayae* among the diatoms.

Well-preserved *D. deflandrei* in Sample 183-1140A-8-CC indicates an age of 16.2 Ma or greater. A few *Ch. altus* are present as a reworked Oligocene taxon.

In-place *C. leptoporus/macintyrei* are absent in Sample 183-1140A-9R-CC, which we assign to the combined nannofossil Zone CN2–CN1 with a minimum age of about 18 Ma. *Discoaster deflandrei* are abundant and pristine in preservation. *Zyghrablithus bijugatus* are common and well-preserved *R. bisecta* represent reworked Oligocene taxa, indicating continued downslope or along-slope transport of eroded older material.

We also assign Samples 183-1140A-9R-CC to 12R-CC to the lower Miocene Zones CN2–CN1. *Discoaster deflandrei* is common to abundant, with *Coronocyclus nitescens, S. moriformis,* and *H. granulata* found in Sample 183-1140A-12R-CC, along with a few reworked *R. bisecta.* The central area of *H. granulata* is so thin that it appears absent in phase contrast light, showing up only in cross-polarized light; in this way, it superficially mimics *Helicosphaera ampliaperta,* a form not seen in this material.

The nannoflora is similar to the above in Samples 183-1140A-13R-CC to 15R-CC except for more reworked Oligocene taxa. For instance, well-preserved *R. bisecta,* including large forms (up to 15 µm), are common in Samples 183-1140A-13R-CC and 14R-CC but are rare to few in 15R-CC. Other taxa we consider reworked are *Discoaster tanii, Ch. altus* (no central cross preserved), and rare *Reticulofenestra umbilica* (lower Oligocene). Among the taxa considered to be in place, nannofloras in Samples 183-1140A-14R-CC to 15R-CC are dominated by *C. abisectus* and *C. floridanus* (about 60%) plus *C. pelagicus* (about 35%). Among the diatoms, we noted *Coscinodiscus rhombicus* (Oligocene to lower Miocene) in Sample 183-1140A-13R-CC, and, in the silicoflagelates, *Distephanus crux longispinus* was found in Sample 183-1140A-14R-CC.

Sample 183-1140A-16R-CC is somewhat problematic in that it could be dated as Oligocene considering the number of older nannofossil taxa in it, but we consider all of them to be reworked. They include rare to few *Ch. altus* (many intact), few *R. bisecta,* and rare to few *R. umbilica* and *Reticulofenestra samodurovii* (both lower Oligocene). Forms considered indigenous are common *D. deflandrei* and *Coccolithus miopelagicus* (up to 18 µm). Diatom floras include *Bogorovia veniamini* and *C. rhombicus* (Oligocene to lower Miocene).

There is no uncertainty as to the Oligocene age of Sample 183-1140A-17R-CC because large *R. bisecta* and *D. deflandrei* are abundant. *Bogorovia veniamini* fragments are present among the diatoms, and *Distephanus speculum pentagonus* among the silicoflagellates.

We noted the top of the nannofossil mid-Oligocene *Ch. altus* Zone in Sample 183-1140A-18R-CC, where the nominate taxon is very abundant; about 60% have complete central crosses. *Cyclicargolithus* are abundant and *Clausicoccus fenestratus* is present. *R. samodurovii* is reworked.

The last occurrence (LO) of *Z. bijugatus* is noted in Sample 183-1140A-19R-CC in about the same stratigraphic position as at Site 1139. *Discoaster tanii* and *C. fenestratus* are few, as is the diatom *C. rhombicus.*

Samples 183-1140A-20R-CC to 23R-CC are all included in the *Ch. altus* Zone. *Bachmannocena apiculata* prominent among the silicoflagellates. Sample 183-1140A-24R-CC is somewhat problematic in that it contains few *Reticulofenestra hillae* and *R. umbilica* (both up to 16 µm), very abundant *C. fenestratus,* two specimens of *Coccolithus formosus,* and a single specimen of *Isthmolithus recurvus.* We presume that the latter two taxa are reworked, and we tentatively assign the sample to the *Reticulofenestra daviesii* Zone. The sample includes abundant *Blackites spinosus,* common *D. deflandrei,* few *Discoaster tanii nodifer* (with large central bosses as in *Dictyocha ornata*), abundant *Ch. altus,* rare *Chiasmolithus oamaruensis* (reworked?), common *R. bisecta*, and few *S. moriformis*. We observed no siliceous microfossils.

Isthmolithus recurvus, D. tanii nodifer, and *R. umbilica/hillae* are abundant and *C. formosus* is common in the last recovered sediment (Sample 183-1140A-25R-5, 90 cm) above the first basalt encountered in the hole. Otherwise, the assemblage is similar to that in the superjacent core catcher. The possible age range represented by the last occurrence of *C. formosus* (32.8 Ma) and the first occurrence of *I. recurvus* (35.7-36.3 Ma at these latitudes according to Wei, 1992) spans the Eocene/Oligocene boundary. The high abundance of *C. fenestratus,* however, would suggest an earliest Oligocene age (~CP16a/b) when compared with the Eocene/Oligocene sequence at Deep Sea Drilling Project (DSDP) Site 511 (Leg 71) on the Falkland Plateau and Ocean Drilling Program (ODP) Site 737B (Leg 119) on the SKP (Wise, 1983, table 1A; Wei and Thierstein, 1991, table 3).

Beneath the first basalt encountered, some subjacent flows contained sediments apparently trapped between or within the flows (see **“Lithostratigraphy,”** p. 3, and **“Physical Volcanology,”** p. 12). Among these are a piece of greenish chalk in interval 183-1140A-31R-1, 135–139 cm, and 1-m-thick orangish, partly dolomitized nannofossil chalk found in Samples 183-1140A-32R-3, 61–63 cm, and 32R-3, 115 cm. Both intervals contained essentially the same nannofloral assemblage with excellent preservation in the greenish chalk (better than at the base of the sedimentary sequence overlying basalt in Core 183-1140A-25R) and moderate preservation in orange chalk below. As both assemblages from the intercalated chalks have essentially the same compositions, we describe here the better preserved assemblage in the greenish chalk (Sample 183-1140A-31R-1, 135–139). This assemblage consists of many of the same forms as in Core 183-1140A-25R, which overlies the basalt; however, there are some important differences. The assemblage is composed of abundant *I. recurvus, C. oamaruensis, Ch. altus, C. formosus, C. pelagicus, R. umbilica/samodurovii, Z. bijugatus,* and *B. spinosus;* common

Discoaster tanii nodifer (five- and six-rayed, with large central area knobs), and *D. deflandrei,* few *S. moriformis, R. daviesii,* and *Coccolithus eopelagicus* (up to 21 µm); and rare *Helicosphaera compacta* (a single small [9-µm] specimen). Noticeably absent are *C. fenestratus,* which are abundant in Core 183-1140A-25R. Other differences include a higher percentage of *C. oamaruensis* (approximately equal in number to its evolutionary descendant, *Ch. altus*), a larger number of *C. formosus,* and a smaller size range among the *R. bisecta* (maximum size = 12 vs. 14 µm in Core 183-1140A-25R). Of these differences, the larger percentage of the ancestral form *C. oamaruensis* vs. *Ch. altus* indicates an older assemblage. This, plus the absence of *C. fenestratus,* indicates that the assemblage is latest Eocene (~CP15b) rather than earliest Oligocene (cf. Eocene/Oligocene boundary sequence on the Falkland and southern Kerguelen plateaus [Wise, 1983, table 1A; Wei and Thierstein, 1991, table 3]).

Planktonic Foraminifers

Planktonic foraminifer assemblages consist of species characteristic of the Southern Ocean, and, in places, species associated with the low latitudes. The Miocene fauna can be mostly characterized in terms of the Neogene Kerguelen (NK) zonal scheme (see **"Biostratigraphy,"** p. 10, in the "Explanatory Notes" chapter), but in intervals where warmer water species are present, we refer to the Transitional Miocene (Mt) zonation of Berggren et al. (1995).

We examined planktonic foraminifers in core-catcher samples from the 234.5-m pelagic succession (Cores 183-1140A-1R to 25R) and from the dolomitized chalk beds that occur between submarine basalt flows of Unit III (Cores 183-1140A-31 and 32R). We examined additional samples within cores to locate major stratigraphic boundaries. Preservation is good in the Miocene but diminishes downhole in Paleogene cores because of dissolution and, in Core 183-1140A-25R, because of dolomitization of carbonate. Minor carbonate laminae between lavas of Unit III occasionally show signs of thermal alteration.

Planktonic foraminifers are generally sparse in the biosiliceous sediments of the middle Miocene (Cores 183-140A-1R to 5R), becoming more common in the early Miocene (Cores 183-140A-6R to 14R) as the biogenic carbonate content increases. Foraminifers are never abundant in the >63-mm size fraction of Unit II greenish gray, foraminifer-bearing nannofossil chalk and ooze, because of dilution by carbonate grain aggregates that did not break down during sample processing. Planktonic foraminifers are extremely rare in Sample 183-1140A-25R-CC and absent in Sample 183-1140-32R-CC as a result of abundant sand-sized, rhombic dolomite crystals that dominate the >63-µm size fraction. In places, reworked Oligocene forms are in low abundance in the Miocene section.

Neogene

The youngest planktonic foraminifers found at Site 1140 are of late middle Miocene age. Samples 183-1140A-1R-CC and 2R-CC contain occasional *Globigerina bulloides, Globigerina falconensis, Globorotalia scitula, Globorotalia miozea,* and *Neogloboquadrina nympha,* an assemblage characteristic of upper middle Miocene Zone NK5. Planktonic foraminifer abundance is variable in the subjacent few cores downhole. Examination of Sample 183-1140A-3R-CC reveals that the Last Appearance Datum (LAD) of *N. nympha* is in Core 183-1140A-3R. This sample contains *Globigernia woodi, Globigerina praebulloides,* common tenuitellids, *G. miozea,* and *G. praescitula,* in addition to *N. nympha,* the nominate taxon of lower middle Miocene Zone NK4, to which we assign this sample.

A similar fauna occurs in Samples 183-1140A-4R-CC and 5R-CC. In addition to globorotalids and globigerinids characteristic of Zone NK4, the latter sample also contains low numbers of *Orbulina* spp., indicating a maximum age for this sample of 15.1 Ma (First Appearance Datum (FAD) *Orbulina*) and confining it to the upper part of NK4. This species is usually restricted to tropical and temperate waters and has never been recorded previously from the Kerguelen Plateau. Its occurrence at Site 1140, the most northerly Kerguelen Plateau locality drilled, suggests that this area experienced warmer conditions than other regions of the Kerguelen Plateau during the middle Miocene. In Sample 183-1140A-6R-CC, *G. praescitula* occurs with less angular globorotalids such as *Globorotalia zealandica* and *Paragloborotalia incognita,* species associated with Zones NK3–NK4.

Catapsydracids appear for the first time in radiolarian-rich Sample 183-1140A-7R-CC and are abundant in the subjacent sample. They occur in this interval with *P. incognita, G. zealandica, G. praescitula,* and common tenuitellids. In the absence of *G. miozea,* we assign this assemblage to Zone NK3.

The next interval of cores (Cores 183-1140A-9R to 12R) is characterized by common *P. incognita,* catapsydracids, *Tenuitella munda, Globigerina brazieri,* and a large, evolute globigerinid with a distinctive rimmed aperture comparable to Berggren's (1992) *Globoturborotalia* sp. cf. *Globigerina labiacrassata.* We do not find large globorotalids below Core 183-1140A-8R; therefore, we assign the assemblage to early Miocene Zone NK2.

Quality of preservation and abundance of planktonic foraminifers diminish in the greenish gray nannofossil clay of cores downhole as a result of the increasing effects of dissolution and dilution by abundant carbonate grain aggregates. Preservation is particularly poor in Samples 183-1140A-9R-CC to 15R-CC. In these cores, we recognize an early Miocene fauna composed of small, dissolution-resistant forms, including *P. incognita, Paragloborotalia opima, T. munda,* catapsydracids, and small indeterminate globigerinids that are not zone-specific. In addition, Sample 183-1140A-14R-CC contains a large angular form of possible globoquadrinid affinities. Rare and sporadic *Chiloguembelina cubensis* in these cores are probably reworked from older sediments.

Paleogene

The first indisputable Oligocene sediments are indicated by *Globigerina euapertura* in Sample 183-1140A-20R-CC. *Paragloborotalia opima, Globorotaloides suteri, Catapsydrax dissimilis, Catapsydrax unicavus,* and *Tenuitella* spp., species characteristic of the upper Oligocene Zones AP15 and AP16, are also present in this and the subjacent sample. We located the downhole LAD of *C. cubensis* in Core 183-1140A-20R. In the absence of *Subbotina angiporoides,* the marker for Zone AP13, we assign this sample to the AP14–AP15 zonal range. Poor preservation of foraminifers in overlying Sample 183-1140A-20R-CC prevents delineation of these two zones. This sample contains a rather impoverished fauna composed of rare paraglobrotalids, catapsydracids and *T. munda,* and lacks *G. labiacrassata,* the AP14–AP15 boundary maker. We also assign the core catcher of Core 183-1140A-21R, containing a similar assemblage of foraminifers, to the same range of biozones.

The downhole LAD of *S. angiporoides* occurs in Sample 183-1140A-22R-CC. In addition to *S. angiporoides,* this sample and the sample below (Sample 183-1140A-23R-CC) contain *C. cubensis, T. munda,* and *Tenuitellinata angustiumbilicata* species characteristic of the early Oligocene Zone AP13 age. *Subbotina utilisindex* is also present in these samples, although, as noted in the Site 1137, 1138, and 1139 chapters, this species is often difficult to distinguish from the Eocene species *Subbotina linaperta*. *Subbotina linaperta* is normally confined to the middle and upper Eocene, so its possible occurrence in lower Oligocene sediments at Sites 1140 and 1139 is noteworthy. The Leg 119 Shipboard Scientific Party (1989) recorded *S. linaperta* ranging into the early Oligocene at Kerguelen Plateau Site 737 (Leg 120).

Core-catcher samples from the final two cores of Unit II, which overlie submarine basalts (Cores 183-1140A-24R and 183-1140A-25R), contain increasing amounts of dolomite with only sparse planktonic foraminifers. Preservation and abundance is still moderate to good in Sample 183-1140A-24R-CC, but deteriorate rapidly within Core 183-1140A-25R. Sample 183-1140A-25R-4, 135–139 cm, is the oldest sample examined above the first basalts that contains recognizable planktonic foraminifers. A fauna composed of *S. angiporoides, C. cubensis, C. unicavus,* and *S. utilisindex* is present, suggesting these sediments are also of early Oligocene (Zone AP13) age. The basalt-sediment contact occurs at the base of Core 183-1140A-25R.

Minor interbeds of nannofossil chalk were recovered in the basalt cores and were apparently deposited between basalt flows. A small (>10 cm) piece of greenish-gray nannofossil chalk occurs in interval 1140A-31R-1, 134–139 cm. It contains very well-preserved planktonic foraminifers including *C. cubensis, Paraglobrotalia nana, S. angiporoides, C. unicavus, S. linaperta/utilisindex,* possible *Praetenuitella insolita,* and common *Globigerinatheka index,* which are characteristic of middle to late Eocene Zones AP11–AP12. The Eocene/Oligocene boundary would appear to occur between Cores 183-1140A-25R and 31R. Foraminifers were extremely sparse within 1.03 m of rusty brown and pale brown dolomitized chalk in Section 183-1140A-32R-3. Rare and poorly preserved specimens of *G. index, C. cubensis,* and *P. nana* in the pale brown chalk, Sample 183-1140A-32R-3, 111–114 cm, indicate a similar middle to late Eocene age. Low recovery in intervening Cores 183-1140A-26R to 30R makes it impossible to locate the position of the Eocene/Oligocene boundary more precisely using biostratigraphic evidence alone.

At high latitudes, in the absence of *Hantkenina* spp. (the LAD of which denotes the Eocene/Oligocene boundary at low latitudes [Coccioni et al., 1988; Berggren et al., 1995]), the LAD of *G. index* provides a proxy for the Eocene/Oligocene boundary. This useful index species and zonal maker for the top of Zone AP12 is apparently absent from sediment samples above the basalt. Preservation problems and low foraminifer abundance may account for the absence of *G. index,* although this seems unlikely as it is usually a fairly robust species. An early Oligocene, rather than a latest Eocene age, is also supported by the nannofossils (see **"Calcareous Nannofossils and Diatoms,"** p. 6). We therefore estimate from foraminifers a minimum age of 34.3 Ma for the first basalts encountered in Hole 1140A based on the maximum sediment age.

Eocene/Oligocene Boundary Biomagnetostratigraphic Correlation

Biostratigraphic evidence for an Oligocene age of strata above the basalt contact and a late Eocene age of sediments below, is consistent with the paleomagnetic reversal record in the cores (see **"Paleomagnetism,"** p. 22). Sediments below interval 183-1140A-25R-4, 0–30 cm, which are assigned to lower Oligocene foraminiferal Zone AP13 and nannofossil Zone ~CP16a/b, are of a reversed polarity that can probably be correlated with C13r of the geomagnetic reversal time scale (GRTS) in the earliest Oligocene. Above interval 183-1140A-25R-4, 0–30 cm, sediments exhibit normal polarity, possibly C13n.

The first basalts beneath the chalk succession are of a normal polarity, whereas the intercalated chalks beneath the contact (Sample 183-1140A-31R-1, 134–139 cm) lie within basalts of a reversed polarity. As noted above, we assigned these sediments to late Eocene, high-latitude Biozone AP12, which, based on approximate correlations to the Berggren et al. (1995) GRTS, spans C13–C17.

Silicoflagellates

Diverse silicoflagellates are common in nearly all core-catcher samples from Site 1140A, and are sometimes abundant and well preserved. Beginning in Sample 183-1140A-2R-CC with two species of the genus *Distephanus* Stohr and ending in Sample 1140A-22R-CC with the genus *Corbisema* Hanna, we found that the amount of debris at the bottom of the sequence was higher than the number of undamaged skeletons. In the last few sediment cores, intact silicoflagellates appear to be absent.

Preliminary results show that the silicoflagellates range in age from late Miocene to late Oligocene. The data support the foraminifer and the calcareous nannofossil biostratigraphy.

Among the age-diagnostic species, we observed the last occurrence of *Corbisema tricantha tricantha* (Ehrenberg) Hanna together with a high number of *Distephanus crux crux* (Ehrenberg) Haeckel in Sample 183-1140A-7R-CC. The former seems to be a good marker for the middle Miocene.

Corbisema archangelskiana (Schulz) Frenguelli, which we found only in Sample 183-1140A-21R-CC, is a characteristic upper Oligocene species. Also of importance in this sample is the first uphole occurrence of *Naviculopsis bipaculata* (Lemmermann) Frenguelli. More detailed results and a correlation with diatom biostratigraphy will be the objective of shore-based studies.

PHYSICAL VOLCANOLOGY

Introduction

Hole 1140A recovered 43.4 m of interbedded pillow lavas and sediments in the basement. These have been divided into 6 units (Table **T5**), which were divided on the basis of inferred time breaks. This includes 5 distinct packages of pillow and massive basalts and a dolomite interbed. In this section, we provide detailed descriptions of the volcanic features in each unit followed by their interpretation. There is a very small amount of disseminated volcanic detritus, including alkali feldspar crystals, lithic fragments, and glass shards, throughout the over-

T5. Basement units, **p. 108.**

lying sediments (see **"Lithostratigraphy,"** p. 3), but only one discrete, basaltic glass shard-rich tephra horizon (interval 183-1140A-18R-6, 102–107 cm) was identified at Site 1140.

Basement Unit Descriptions

Unit 1 (Interval 183-1140A-25R-6, 0 cm, to 31R-1, 0 cm)

Recovered rock from Unit 1 consists of 12.46 m of ~0.5-m diameter pillows of aphyric to sparsely plagioclase-phyric basalt with metamorphosed calcareous sediments between many of the pillow margins. However, in the middle of the pillow pile (interval 183-1140A-27R-1, 70 cm, to 27R-4, 51 cm), 3.9 m of massive lava was recovered. Elsewhere, glassy pillow lobe margins are present at 5- to 50-cm intervals. Metamorphosed sediments in contact with the pillow margins commonly contain ≤5-mm angular glass fragments and well-preserved foraminifers (see Fig. **F20**) (see **"Igneous Petrology and Geochemistry,"** p. 16). Where recovered, the glassy rinds are consistently very close to 1 cm thick (Fig. **F6**). Rinds that appear wider than 1 cm on the open face of the core are cut obliquely; they are not thicker than other rinds. Inward from the glassy rind, there is an ~1-cm-thick zone with a very fine grained to glassy groundmass and sparse vesicles. In Unit 1, these vesicles make up ~3 vol% of the lava and have irregular angular shapes elongated normal to the margin of the pillow. The remainder of the interior of each pillow contains 0.03–0.07 spherical vesicles/cm^2 with 0.5- to 0.8-mm diameters (~0.01 vol%). The vesicle distribution in the 3.9-m-thick lobe is shown in Figure **F7.**

F6. Close-up photograph of interval 183-1140A-26R-1, 0–10 cm, **p. 42.**

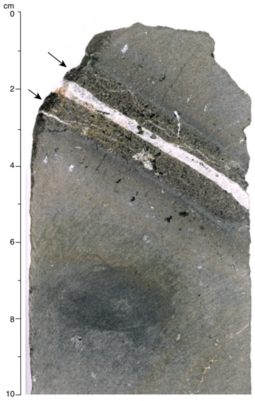

F7. Vesicle distribution in the thickest lobe of basement Unit 1, **p. 43.**

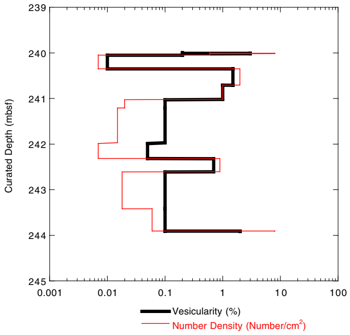

Unit 2 (Interval 183-1140A-31R-1, 0–134 cm)

Recovered rock from Unit 2 consists of three pillows of highly plagioclase-phyric basalt. The first lobe (interval 183-1140A-31R-1, 0–30 cm) has radial and concentric joints that suggest a 40-cm-diameter pillow. The second lobe (interval 183-1140A-31R-1, 34–67 cm) has a margin with a curvature that would indicate a 50- to 70-cm-diameter pillow, if it has a near cylindrical shape. The third lobe (interval 183-1140A-31R-1, 67–134 cm) has no recovered basal chill, indicating that it is >67 cm in diameter. Unlike Unit 1, the margins and pillow interiors of Unit 2 have a similar vesicularity. Unit 2 contains 2%–3% spherical vesicles 3.5–0.3 mm in diameter, with ~1 mm being the most common vesicle size. Vesicle number density varies from 2.5 to 4.5 vesicles/cm^2, with higher number densities where vesicles are smaller.

Unit 3 (Interval 183-1140A-31R-1, 134 cm, to 32R-3, 43 cm)

Recovered rocks from Unit 3 consist of four lobes of aphyric to sparsely-plagioclase-phyric basalt topped by a piece of green calcareous chalk (see **"Lithostratigraphy,"** p. 3). The recovery of the upper part of Unit 3 is poor, with only 1- to 11-cm loose pieces. The pieces midway through Section 183-1140A-31R-2 contain a pillow margin, suggesting a lower part of one lobe and the uppermost part of a second in this poorly recovered portion. Core 183-1140A-32R has better recovery and starts with the interior of a large lobe with a well-preserved basal chill in interval 183-1140A-32R-1, 143–144 cm. Neither the upper nor lower chill on the third lobe were recovered, but the top of the fourth lobe is well preserved in interval 183-1140A-32R-2, 73–77 cm. Unit 3 ends with the basal chill of this lobe. The vesicularity within Unit 3 is distinct from both Units 1 and 2; long, irregular pipe vesicles are the most striking feature (Fig. F8). Figure F9 shows the distribution of vesicles in the central part of Unit 3. In addition, the last lobe has an unusually thick upper chill zone, with 2 cm of fine-grained groundmass followed by >7 cm of a vesicular top. This zone has 2 vol% vesicularity with a mix of both spherical and irregular angular shapes ranging in size from 0.15 to 4 mm. Below this vesicular top, the lava is massive with only the long irregular pipe vesicles, except for a short interval (interval 183-1140A-31R-2, 107–113 cm), where the vesicularity is identical to the vesicular zone at the top of the lobe. The massive lava contains ~1.5% irregular angular vesicles 0.1–5 mm in size in addition to the larger pipe vesicles.

Unit 4 (Interval 183-1140A-32R-3, 43 cm, to 32R-4, 0 cm)

Unit 4 is a dolomite to dolomitic-nannofossil-chalk that is more highly dolomitized toward the top and bottom. This unit is described in more detail in the "Lithostratigraphy," p. 3, and "Alteration and Weathering," p. 19.

Unit 5 (Interval 183-1140A-32R-4, 0 cm, to 34R-4, 0 cm)

Recovered rock from Unit 5 consists of thick lobes of moderately plagioclase-phyric basalt. The top of the unit is altered to grayish orange (10YR 7/4) and was relatively poorly recovered. Only two pillow margins are present in intervals 183-1140A-33R-1, 19–20 cm and 37–39 cm, suggesting that the recovered portion of Unit 5 is composed of only three lobes. The second margin has a very fine grained orange (palagonitized) rim followed by a zone with irregular, ill-formed pipe vesicles up to 3 cm long (Fig. F10). Downhole measurements indicate the presence of a sedimentary interbed in the upper part of Unit 5 (see "Downhole Measurements," p. 29). This probably overlies the orange pillow rim, but there is insufficient change in the recovered rocks to justify the subdivision of Unit 5. The lava is significantly more vesicular than Units 1 and 2; point counting within the "massive" lava yields 3.9 vol% vesicles. These vesicles are generally 0.2–2.2 mm in diameter, irregular subangular in shape, and at a density of ~20 vesicles/cm^2. Figure F11 shows the details of the vesicle distribution within the upper part of the third lobe of Unit 5. Note in particular the occurrence of pods with as much as 70 vol% vesicles and the thin sheet-like vesicular regions.

Unit 6 (Interval 183-1140A-34R-4, 0 cm, to 37R-4, 34 cm)

The recovered rock from Unit 6 is a sequence of pillows of aphyric to moderately-plagioclase-phyric basalts overlain by a 6-cm piece of orange dolomite (see "Lithostratigraphy," p. 3). The morphology of the pillows is similar to those in Unit 1, with a ~1-cm glassy rim, followed by a vesicular zone with some irregular ~1-mm-diameter pipe vesicles elongated perpendicular to the chill margin and a generally nonvesicular interior. Unlike Unit 1, the vesicular zone is up to 5 cm thick with ~2 vol% vesicles. Figure F12 shows the vesicle distribution through one pillow in Unit 6. Another feature that was present in Unit 1 but better preserved in Unit 6 is pieces of the chill margin that have been pushed 2–3 cm back into the pillow lobe with metamorphosed sediments filling the resulting space (Fig. F13). Also, similar to Unit 1, Unit 6 con-

F8. Close-up photograph of interval 183-1140A-32R-2, 126–140 cm, **p. 44.**

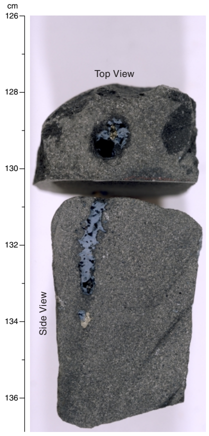

F9. Vesicle distribution through a segment of basement Unit 3, **p. 45.**

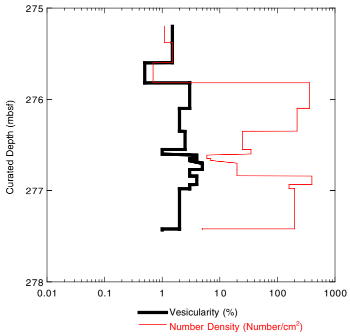

F10. Close-up photograph of interval 183-1140A-33R-1, 31–45 cm, **p. 46.**

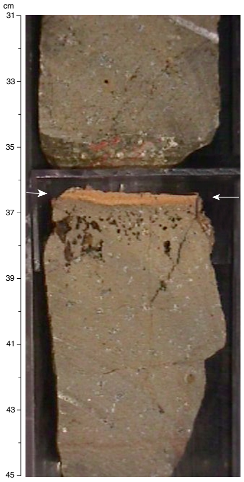

tains one >4-m-thick massive lobe. This thick lobe has a coarser groundmass texture. The upper 30 cm of the lobe has ~0.5% round vesicles ~0.5 mm in diameter. Glassy mesostasis blebs are wispy in interval 183-1140A-36R-2, 65–105 cm and distinct in interval 183-1140A-36R-4, 43–77 cm. The zone with distinct mesostasis appears completely devoid of vesicles, but the remainder of the lobe has 0.2 round vesicles/cm² with diameters ≤0.5 mm. These vesicles may be distributed in ~10-cm-thick more-vesicular layers and 10-cm-denser layers, but the vesicles are too rare for confident statistics across a 5- to 6-cm-diameter core. There is also a region of extreme alteration and clay-filling in Section 183-1140A-35R-1 at 116–123 cm.

Interpretation

Unit Distinctions

The placement of basement unit boundaries in Hole 1140A was relatively straightforward. The dramatic increase in phenocryst content after >20 m of no recovery (Cores 183-1140A-29R and 30R) required separating Units 1 and 2. Logging data indicates the presence of an unrecovered 2.2-m-thick sediment package at the top of Unit 2, and a magnetic reversal confirms a significant time gap between the emplacement of these two lava packages (see **"Downhole Measurements,"** p. 29, and **"Paleomagnetism,"** p. 22). A sedimentary interbed and decrease in phenocryst content marks the change from Unit 2 to Unit 3. Unit 4 was a well-recovered >1-m-thick sediment package that was designated as a separate unit, and a package of dolomite marks the Unit 5/6 boundary.

Lobe Sizes

Two effects make lobe-size determinations from the recovered rocks of Site 1140 imprecise. First, the core recovery is incomplete, and glassy margins are the most likely material to be lost. Second, the core produces a random vertical cut through the cylindrical pillows. However, plots of the estimated average thickness of the lobes in the recovered rocks show some interesting differences in the units (Fig. **F14**). In particular, Unit 5 has an average lobe thickness three to five times greater than the other units. Downhole logging shows that Unit 5 includes an ~10-m-thick massive lobe. Units 1 and 6 each contain one lobe ≥3 m thick that is also visible in the downhole measurements (see **"Downhole Measurements,"** p. 29). The size of these lobes suggests that they were produced differently than the stacks of 0.5–1-m-thick pillows.

The thicker lobes of Unit 5 and the isolated thick lobes in Units 1 and 6 probably have sheet-like cross-sectional shapes. The low strength of basaltic lava does not allow for unsupported subaqueous cylinders much greater than 1 m in diameter. The sides of "megapillows" are usually supported by sediments or hyaloclastites. Abundant hyaloclastites are not present in Hole 1140A, nor is there any evidence that the lobes were intruding to many meters depth into the sediments. Production of sheet flows implies relatively high effusion rates and low slopes (Gregg and Fink, 1995).

F11. Vesicle distribution through a segment of basement Unit 5, **p. 47.**

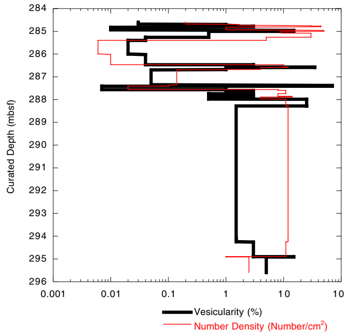

F12. Vesicle distribution through a segment of basement Unit 6, **p. 48.**

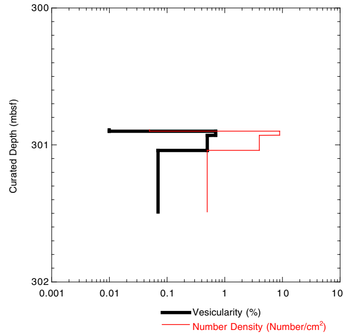

F13. Close-up photograph of interval 183-1140A-35R-2, 37–47 cm, showing a fractured chill margin in basement Unit 6, **p. 49.**

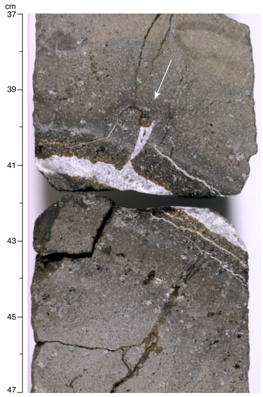

F14. Graph of average lobe thickness in recovered rocks from Hole 1140A, **p. 50.**

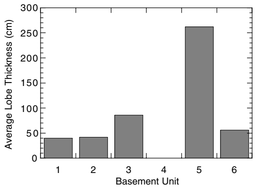

Vesicularity and Vesicle Distribution

The changes in vesicularity between the units and within individual lobes provide important information about the emplacement of these lavas. The generally low vesicularity of all the lava and the lack of significant hyaloclastite formation suggest that the lava was emplaced in a deep marine setting. Vesiculation is suppressed at depths below a 1-km water depth for all except the most H_2O-rich basaltic magmas. Fragmentation caused by steam generation is also suppressed below ~1 km of water depth. The lack of extensive talus or hyaloclastite rubble also suggests low to moderate slopes. The enhanced vesicularity associated with the margins of pillows is probably the result of volatile exsolution during crystallization of anhydrous phases.

Summary

The lavas of Site 1140 were emplaced in a deep marine setting and consist of a mix of pillow and sheet flows. Moderate slopes and variable eruption rates are implied.

IGNEOUS PETROLOGY AND GEOCHEMISTRY

Lithology

Basement recovered at Site 1140 consisted of 86.7 m of submarine igneous rocks and upper Eocene interbedded pelagic sediments at depths from 234.5 to 321.2 mbsf, with 50% recovery (see Fig. **F15**; Table **T6**). In contrast to previous sites (Sites 1136 to 1139), where the principal criteria for division of basement sequences into units were volcanological, at Site 1140 we used (1) the presence of interbedded sedimentary layers and (2) notable downhole changes in phenocryst abundance or type. On this basis, we divided the section into five basaltic units and one sedimentary unit. Unit thicknesses are presented in Table **T5** (see **"Physical Volcanology,"** p. 12), and we report a summary of the mineralogy, petrology, and igneous texture in Table **T6.** Information on the volcanic features and on alteration are provided in other sections (see **"Physical Volcanology,"** p. 12, and **"Alteration and Weathering,"** p. 19).

F15. Interpretative summary of the lithology, morphology, and mineralogy of basaltic lava flows sampled in the basement units at Site 1140, **p. 51.**

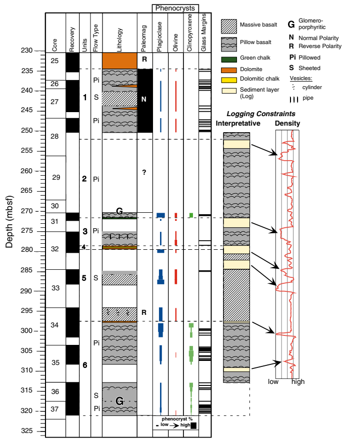

All igneous units are pillow basalts. Recovered parts of Units 2 and 3 consist entirely of small (40–100 cm) basaltic pillows. Units 1 and 6 also have <1-m pillows but also contain large ~5-m massive lobes. Unit 5 is more massive and probably composed of only three large lobes (>3 m thick). Unit 4 consists of pale brown to orange dolomite, of which we recovered 0.8 m, including both upper and lower contacts (see **"Lithostratigraphy,"** p. 3).

T6. Petrographic summary of igneous units with mineralogies, **p. 109.**

An ~3-cm-thick piece of pale green, poorly laminated, sheared nannofossil chalk separates Units 2 and 3 and another ~4-cm-thick piece of pink to orange, well-indurated, fine- to medium-grained dolomite separates Units 5 and 6. These two thin sedimentary layers are grouped with the underlying basaltic units. We interpret the units separated by sedimentary interbeds (Units 2 and 3 and Units 5 and 6) to represent separate eruptions. Even though there was no recovery in the cores that separate Units 1 and 2 (Cores 183-1140A-29R and 30R), a probable sedimentary interlayer was recorded in logging data, and magnetic polarity changes (see **"Downhole Measurements,"** p. 29, and **"Paleomag-**

netism," p. 22). We therefore interpret Units 1 and 2 as separate eruptions. All recovery from Unit 2 was in a single 140-cm-thick section (Section 183-1140A-31R-1), but it is likely that this is only the basal portion of a thicker unit (see Fig. **F15**). Some units may, however, contain more than one eruption of lithologically similar lava, as suggested, for example, by isolated pockets of sedimentary material between several pillow margins in Unit 1.

Petrography

With the exception of regions adjacent to pillow margins, particularly where sediment is intercalated or in regions of veining, the basalt recovered is very fresh. The glass at pillow margins shows little sign of hydration or devitrification, and minerals in pillow interiors are commonly unaltered. In the freshest parts of Units 1 and 2, alteration is limited to replacement of interstitial glass by clay and the filling of vesicles by clay and carbonate (see **"Alteration and Weathering,"** p. 19). The Site 1140 basalts are unique among those recovered during Leg 183 in that they contain fresh olivine and glass.

Anorthite-rich plagioclase ($An_{60–70}$) is the dominant phenocryst phase in all units; it is accompanied by olivine (Fig. **F16**), except in Unit 6, and by clinopyroxene in Units 2 and 6. Units 1 and 2 are petrographically distinct: Unit 1 contains <1% phenocrysts (except in pillow margins), whereas Unit 2 contains ~20% phenocrysts (Table **T6**). Many phenocrysts of plagioclase and clinopyroxene in these units are strongly zoned (Figs. **F17A, F17B, F18A**), and clinopyroxene also displays sector zonation (Fig. **F18B**). Although most of the olivine phenocrysts are partially to completely altered to brown green clay (Fig. **F19**), some are fresh.

Although the mineralogy does not differ greatly from that of basalts recovered at previous sites, submarine eruption has produced distinctive textures. To preserve glass for shore-based study, only two thin sections of pillow margins were made. The outermost 1–2 cm of pillow rims are composed of dark brown glass, which in thin section appears unaltered, except adjacent to interpillow sediment, where it is replaced by brown clay (Fig. **F20A, F20B**). Pillow margins are sparsely porphyritic with a very fine grained to glassy (vitrophyric) groundmass (Figs. **F16, F21, F22**) that contains extremely fine grained plagioclase microlites or small laths with ragged or swallow-tailed terminations (Fig. **F21**). Olivine forms subequant euhedral phenocrysts. In the glassy rinds, some of the olivine phenocrysts contain numerous inclusions of unaltered glass and rare inclusions of chromite (Figs. **F16, F22**). Irregular patches of laminated, foraminifer-bearing dolomitic chalk, and thin (1–2 mm wide) carbonate veins, fill sutures and interstices between some pillows (Figs. **F6, F20B, F23**).

The main mineral phases of the massive interiors of pillows and lobes are similar to those of the chilled margins (Table **T6**). The massive interiors of pillows and lava lobes are, however, more crystalline and coarser grained than the pillow margins, reflecting slower cooling rates in the flow interiors. The textures range from intersertal to intergranular, but unlike other Leg 183 sites, subophitic (Fig. **F24A, F24B**) to locally ophitic textures are present in some of the thicker lobes and pillows. Subophitic texture is most apparent in interiors of the thick lava lobes in Units 5 and 6, where the maximum clinopyroxene and plagioclase grain size reaches 0.7 mm. Flow interiors appear less porphyritic than the margins, probably because phenocrysts of the type

F16. Photomicrograph of the glass from a chilled pillow margin from Unit 1, **p. 52.**

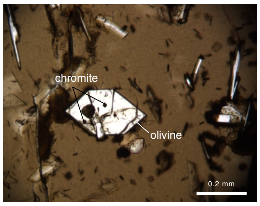

F17. Photomicrographs of plagioclase phenocrysts from a plagioclase-clinopyroxene-olivine-phyric pillow basalt (Unit 2), **p. 53.**

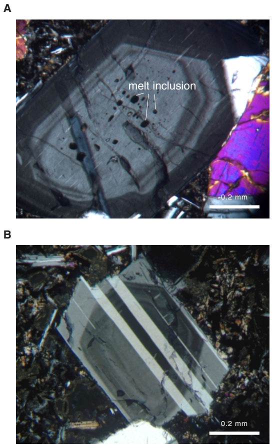

F18. Photomicrograph of clinopyroxene phenocrysts and a glomerocryst, **p. 54.**

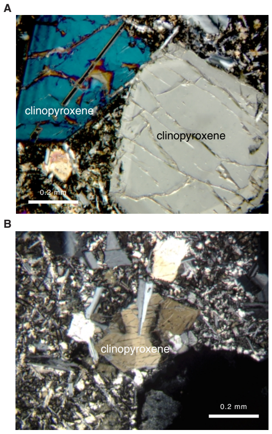

F19. Photomicrograph of a partially altered olivine phenocryst, **p. 55.**

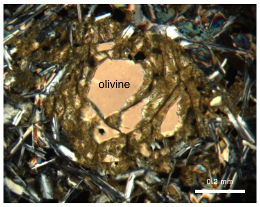

preserved in fine-grained pillow margins became surrounded by late-formed crystals of similar size during slow cooling. Clinopyroxene and plagioclase are major groundmass phases in crystalline areas; minor phases are titanomagnetite (≤5%) and intersertal glass, some of which is still fresh. In some samples, glass has partially crystallized to cryptocrystalline clinopyroxene and opaque minerals. The olivine in the groundmass is partially altered (Fig. F25). Titanomagnetite is generally skeletal. Sulfide of possible magmatic origin is present as minute (<0.01 mm) inclusions in primary minerals and fresh glass (Fig. F26A). Although the small size precludes a positive identification, its optical characteristics suggest that it is pentlandite or pyrite with minor chalcopyrite. Units 2, 3, 5, and 6 (Fig. F8) contain secondary pyrite in veins and as small disseminated grains that replace residual glass (Fig. F26B). Further information on the pyrite is given in **"Alteration and Weathering,"** p. 19.

Major and Trace Element Compositions

We list X-ray fluorescence (XRF) analyses of major and trace elements in 11 basalts in Table T7. Basalt compositions are all tholeiitic (Fig. F27). They are olivine normative in Unit 1 and quartz normative in Units 2, 3, 5, and 6 (Table T7). The low loss on ignition values (<1.8 wt%) support the petrographic evidence that the pillow interiors and the massive portions of these units are relatively unaltered. Except for samples from Units 2 and 3, major element abundances are relatively uniform, with narrow ranges in MgO (6.3 to 8.1 wt%; Mg# from 0.54 to 0.63) and SiO_2 (48.9 to 50.7 wt%) (Fig. F28). However, systematic changes downhole are illustrated in major element abundances. Overall, SiO_2 and Na_2O increase slightly downhole (Fig. F29). In addition, there is a very strong break at Units 2 and 3, which have much higher K_2O, P_2O_5, and TiO_2 and lower Mg#. The major element trends are mirrored by variations in trace element abundances and ratios (Fig. F30). Units 2 and 3 have higher Ba, Zr, Nb, and lower Cr contents and also exhibit the highest $[Nb/Zr]_N$ and $[Zr/Y]_N$ ratios (Figs. F30). Units 1, 5, and 6 define downhole trends of increasing Na_2O content and $[Nb/Zr]_N$ and decreasing Cr, Ni, $[Zr/Ti]_N$, and $[Zr/Y]_N$ (Figs. F30, F31).

Although the compositional variations of Site 1140 lavas reflect variable degrees of crystal fractionation, essentially olivine and plagioclase as observed in thin sections, variations in Nb/Zr and Zr/Y ratios indicate that the whole sequence cannot have been derived from fractional crystallization of a single parental magma composition. In particular, the enrichment in incompatible element abundances and high Nb/Zr and Zr/Y of lavas from Units 2 and 3 could not be derived by fractional crystallization of the higher Mg# lavas in Units 5 and 6. Finally, the magnetic field reversal between Units 1 and 2 (see **"Paleomagnetism,"** p. 22) indicates a significant time break between eruptions of Units 1 and 2.

Comparison with Other Kerguelen Plateau Sites

Units 1, 5, and 6 have relatively low concentrations of incompatible trace elements and almost chondritic ratios of Nb/Zr and Zr/Y (Fig. F31). In a primitive mantle–normalized diagram, Units 1, 5, and 6 are between Site 749 and 750 basalts for most elements, but they are distinguished by Rb and K depletion (or Ba enrichment?). Relative to Units 1, 5, and 6, Units 2 and 3 are more enriched in incompatible elements by

F20. Photomicrographs of boundaries in Unit 1, **p. 56.**

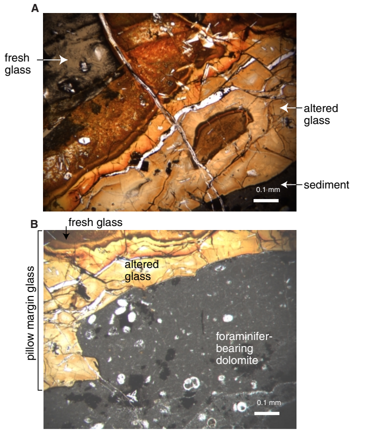

F21. Photomicrograph of a glassy margin of a pillow lava from Unit 1, **p. 57.**

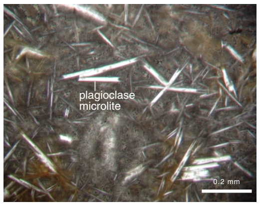

F22. Photomicrograph of the glass from a chilled margin of a pillow lava from Unit 1, **p. 58.**

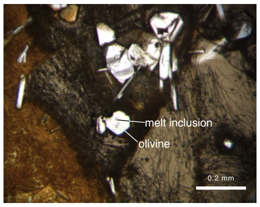

F23. Close-up photograph of a pillow contact breccia from Unit 1, **p. 59.**

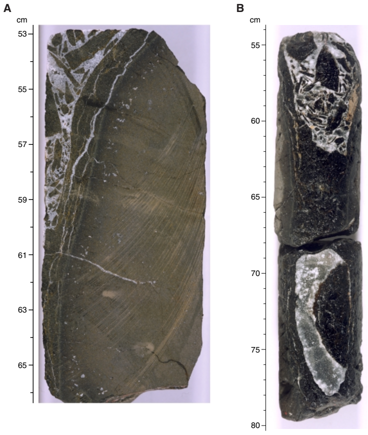

a factor of 5 (Fig. **F31**). Site 1140 lavas are among the most incompatible element-depleted lavas from the Kerguelen Plateau (Figs. **F27, F31**).

Trace element discriminants such as $(Zr/Ti)_N$ vs. Zr illustrate that the Site 1140 basalts fall within the range of central and southern Kerguelen Plateau basalts (Fig. **F32**). The $(Zr/Ti)_N$ values for Units 1, 5, and 6 are within the range of those for Site 749 basalts and are lower than those of basalts from Sites 1136, 1137, and 1138. With regard to Nb/Y vs. Zr/Y, basalts from Units 1, 5, and 6 are again similar to the Site 749 basalts, whereas Units 2 and 3 basalts are similar to the lower series lavas of Site 1138 (Fig. **F33**). Site 1140 tholeiites plot within the field defined by basalts derived from the Iceland mantle plume being distinct from mid-ocean ridge basalts (MORB) (Fitton et al., 1997, 1998). In this respect, they are similar to basalts from Sites 749 and 750, which do not show other evidence of continental crustal assimilation (Fig. **F33**). There is no evidence from shipboard data that Site 1140 magmas assimilated any continental crustal material.

Summary

The following features distinguish Site 1140 basalts from those of other Leg 183 sites:

1. Submarine eruption, as indicated by their pillowed structure and intercalated nannofossil-bearing calcareous marine sediments;
2. Relative absence of posteruptive alteration, as indicated by the preservation of fresh glass at pillow margins and the lack of alteration in massive sections;
3. Tholeiitic basalts with higher MgO (up to 8.1 wt%) and Ni (up to 100 ppm) than other basalts from Leg 183 drill sites on the Kerguelen Plateau; and
4. An age between 33.1 and 35.4 Ma, as indicated by the paleomagnetic and biostratigraphic time constraints (see **"Paleomagnetism,"** p. 22, and **"Biostratigraphy,"** p. 5).

Site 1140 basalts exhibit some important geochemical features. Two of the five basalt units were derived from a geochemically distinct parental magma that had higher abundances of highly incompatible elements. Despite large differences in age and location, basalts from Units 1, 5, and 6 at this NKP site and basalts from Site 749 and 750 on the southern Kerguelen Plateau (SKP) have some significant geochemical similarities; they are slightly enriched tholeiites (i.e., with higher Nb/Y and Zr/Y than MORB). Site 749 and 750 basalts have the highest $^{143}Nd/^{144}Nd$ and lowest $^{87}Sr/^{86}Sr$ ratios of the Kerguelen Plateau (see Fig. **F9,** p. 59, in the "Leg 183 Summary" chapter). These isotope ratios have been interpreted as reflecting the presence of a MORB component in Kerguelen plume-derived magmas. It will be interesting to establish with shore-based isotope studies if Site 1140 basalts show the same features. In contrast to basalts from Site 1137 on Elan Bank, there is no indication that Site 1140 basalts were contaminated by continental crust.

ALTERATION AND WEATHERING

Drilling of basement in Hole 1140A recovered submarine-erupted pillow lavas with lesser and more massive lobes, intercalated with minor dolomitized chalk and brittlely deformed pale green mudstone. Unam-

F24. Photomicrographs of two examples of subophitic texture, **p. 60.**

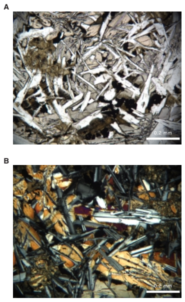

F25. Photomicrograph of a partially altered groundmass olivine, **p. 61.**

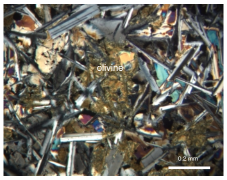

F26. Photomicrographs of skeletal titanomagnetite and secondary pyrite, **p. 62.**

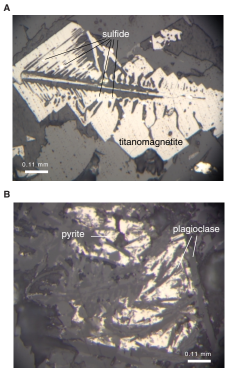

T7. X-ray fluorescence analyses of major and trace elements for igneous units, **p. 110.**

F27. Site 1140 igneous rock and basalt samples, **p. 63.**

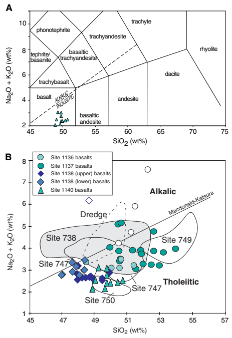

biguous lava pillows indicate that these lavas were erupted on top of the sediments as flows instead of emplaced as sills. The absence of overlying terrestrial sediments indicates that the basement was not subjected to subaerial weathering.

The basement rocks were subdivided into six units; five are composed primarily of basaltic flows. The smaller sedimentary pieces recovered were not recorded as separate basement units (e.g., Sample 183-1140A-31R-1 [Piece 9, 133–139 cm]); Sample 183-1140A-34R-4 [Piece 1, 0–5 cm]) except for Unit 4, which is an ~1-m-thick bed of dolomitized chalk (see **"Igneous Petrology and Geochemistry,"** p. 16). The flows are aphanitic to medium-grained, aphyric to sparsely plagioclase-phyric basalts and mostly only sparsely vesicular. The downhole variation of alteration in the basement (Fig. **F34**) is recorded in the alteration and vein/structure logs for this site (see the **"Supplementary Materials"** contents list). Time constraints precluded detailed analyses of structural data, but orientations were measured for most planar features observed in these cores and were recorded in the vein/structure log. We identified selected secondary minerals by XRD (Table **T8**).

On the margins of lava pillows, vitreous glass abounds (see Fig. **F34**). The glassy margins (~5–10 mm) are macroscopically fresh and isotropic in thin section with only minor alteration along wispy brown clay veins. Highly altered glass is rare, and we recorded only a few occurrences of orange-brown clay with relict fragments of altered glass or hyaloclastite (e.g., Sample 183-1140A-33R-1 [Piece 7, 37–39 cm]; see Fig. **F34**). Most occurrences of altered glass are in Unit 5 (see **"Igneous Petrology and Geochemistry,"** p. 16). Irregular patches (0.5–5.0 mm) of black manganese minerals (manganite and pyrolusite; Table **T8**) in the altered pillow margins possibly suggest an extended duration of exposure of these rocks to ocean currents.

The glassy margins are crosscut by numerous dolomite and/or calcite veins that developed concentrically to the pillow rinds both externally and within the glass itself. The outer veins are generally thick (2–3 mm), and both carbonate minerals exhibit dog-tooth sparry habits indicating mineral precipitation from fluids into voids in the pillow interstices. Commonly, angular fragments of fresh glass have spalled off the quenched rind; these pieces are now preserved in a cement of dolomite and/or calcite (Fig. **F35**). Carbonate veins (<2 mm) within and parallel to the glassy margin are commonly slightly offset by fine clay- or calcite-filled fractures that have developed radially from the pillow margins.

Baked, highly indurated foraminifer-bearing chalk and mudstone are commonly preserved adjacent to the pillow margins and in the interstices (Fig. **F23B**). Rare indenters of these sediments have apparently penetrated through the glassy margins while the basalt was still molten, resulting in internal glassy quenched zones in the pillow interiors. These zones are offset from the quenched rind by a sharp, brittle boundary (Fig. **F36**).

Immediately interior to the glassy margins, we observed a transition from glass to dark gray-brown, variole-rich aphanitic rocks. This zone grades into an orange-brown stained groundmass with sparse vesicles partly filled with brown clay, iron oxyhydroxides, and minor calcite. Mafic groundmass phases (clinopyroxene) are pseudomorphically replaced by brown clay minerals and iron oxyhydroxides. These oxidized halos typically extend 2–5 cm from the pillow margins, but oxidation halos are also developed within the wall rock to brown clay-filled radial fractures that penetrate the interior of the pillows. Large portions of the

F28. Major element abundances plotted vs. Mg#, **p. 64.**

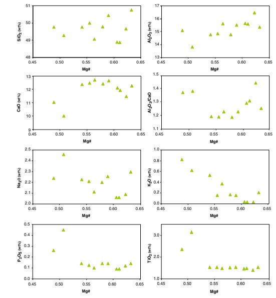

F29. Downcore variations in major element composition for Site 1140 basalts, **p. 65.**

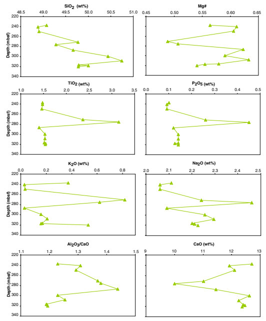

F30. Downcore variations in trace element abundances and primitive mantle–normalized ratios, **p. 66.**

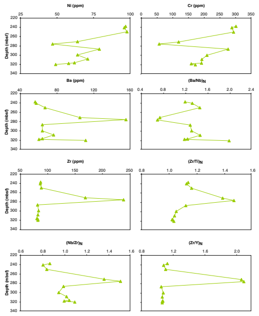

F31. Trace element and basalt patterns for Site 1140, **p. 67.**

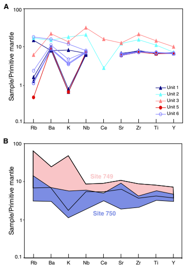

rocks display brown staining and oxidation. The most intense orange-brown staining is common at the edge of the oxidation halo adjacent to the gray basalt (Fig. **F37**).

Away from the pillow margins and vein halos, the groundmass of the crystalline interiors of the lavas are slightly to moderately altered. The fine- to medium-grained interiors of the more massive units are dark gray to greenish dark gray, reflecting alteration of the commonly prominent mesostasis to green clay (Fig. **F34**). Rare, large elongate pipe vesicles (1–2 cm) are partly filled with green or blue clay and coarse-grained pyrite. Pyrite is also common in the groundmass of the fine- to medium-grained basalts, outside the brown oxidation halos.

Carbonates and clay are the most abundant vein fillings, and they are in several morphologies and compositions. Green clay is most common in the gray portions of the basalts, but brown clay (± iron oxyhydroxides) is present within the oxidized halos (Fig. **F37**). Blue clay is abundant, commonly with stringers of pyrite-filled veins in parts of basement Units 2 and 3 (Sections 183-1140A-31R-1 through 32R-3). Open-space filled calcite and dolomite form cements in the interpillow interstices and coarse (<2 mm) veins within the glassy margins. Pale pink calcite veins with a powdery texture are also common in the pillow margins. Toward the bottom of Hole 1140A, fibrous aragonite fills rare subhorizontal veins in fine-grained basalt.

Rare, completely altered but not visibly oxidized patches within the fine- to medium-grained massive interiors of some flows are either elongate subvertical trails (~2 cm × 5–10 cm) or spheroidal (~5–10 cm). High vesicularity (~20%) suggests that these features are pools or rising fingers of late-stage magmatic segregations (see **"Physical Volcanology,"** p. 12). The dominance of altered mesostasis and the complete absence of either groundmass minerals or phenocrysts indicates that these patches were originally glassy. The glassy regions are completely altered to black clay, whereas the generally large vesicles (~5 mm) are filled with green clay and calcite (Fig. **F38**). Basalts hosting these segregations are commonly more altered in the surrounding ~10 cm. Cut surfaces become flaky or desiccated on drying, indicating abundant smectite (cf. Hole 1037A, Escanaba Trough Reference Hole; Fouquet, Zierenberg, Miller, et al., 1998).

Oxidation halos are less common in the more massive fine-grained interiors of the thicker lava units except where these rocks are intercalated with ~1-m-thick beds of dolomitized and oxidized chalk (e.g., Unit 4 and surrounding rocks; Sections 183-1140A-32R-3 through 32R-4). The dolomite within these sediments is coarsely crystalline, typically as colorless rhombs. It is secondary after primary sedimentary phases and replaces or partly fills foraminifers. Dolomite within the lavas is most common in the interstices between pillow lobes, and there is a clear association between the presence of dolomite in the lavas and the close proximity of intercalated sediments. Although elucidation of the mechanism of dolomite precipitation will require postcruise geochemical investigation, it is likely that the sediment horizons have acted as channels, enabling large volumes of seawater-derived fluids access to the basement. This resulted in the precipitation of abundant, euhedral, colorless dolomite crystals in the margins of the chalks and numerous sparry dolomite ± calcite veins on the pillow margins.

The alteration at Site 1140 strongly resembles that in young mid-ocean-ridge lavas from the uppermost ocean crust. In particular, it is very similar to that described from the ocean crust reference sections penetrated in DSDP–ODP Holes 504B and 896A, located in 5.9-m.y.-old

F32. Primitive mantle–normalized Zr/Ti vs. Zr and Zr vs. Nb diagrams, **p. 68.**

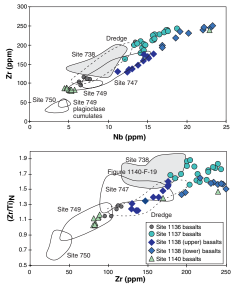

F33. Nb/Y vs. Zr/Y diagram, **p. 69.**

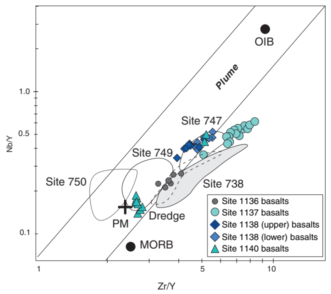

T8. Secondary minerals within basement units identified by XRD, **p. 111.**

F34. Alteration downhole in Hole 1140A vs. depth, **p. 70.**

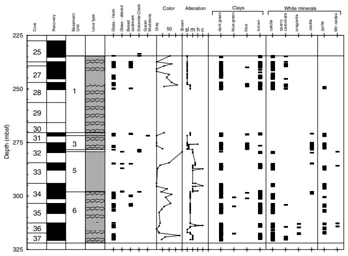

F35. Close-up photograph of Sample 183-1140A-28R-3 (Piece 2, 86–102 cm), **p. 71.**

crust in the eastern equatorial Pacific Ocean (Alt et al., 1986; Teagle et al., 1996). The secondary minerals and the intensity of alteration are indistinguishable from normal young ocean crust. Only abundant dolomite is rare in the alteration of the upper ocean crust (Alt and Teagle, 1999). However, the alteration of basalts erupted in a mid-ocean ridge setting may differ from that of basalts formed on the flanks of a seamount or other submarine volcanic edifice. If the Hole 1140A flows are compositionally similar to MORB, then Hole 1140A may provide an important section of intermediate age (10 to 110 Ma) for assessing the progressive alteration of the upper oceanic crust with time.

PALEOMAGNETISM

We measured the natural remanent magnetization (NRM) of most archive halves from Hole 1140A with the pass-through cryogenic magnetometer using measurement intervals of 5 and 2.5 cm for sediments and basement rocks, respectively. Subsequently, sediment and basement core sections were demagnetized with peak alternating fields (AF) of 20 and 50 mT, respectively. We did not analyze highly disturbed sections. Discrete sediment samples were stepwise AF demagnetized up to 30 mT. Six discrete basement samples were thermally demagnetized at temperatures of up to 620°C.

We obtained stable and reliable paleomagnetic directions from the sediments of Hole 1140A. Correlation of biostratigraphic data and polarity reversals suggests that the reversed and normal chrons are middle Miocene to early Oligocene or latest Eocene in age. We obtained reliable paleomagnetic directions from basement rocks and a magnetic reversal at the boundary between basement Units 1 and 2. We compared magnetic properties with lithologic and basement units.

Sediments

One archive section of most cores was stepwise demagnetized up to 30 mT. We took one or two discrete samples per section, and 11 samples were stepwise AF demagnetized up to 30 mT to confirm the reliability of whole-core measurements. We obtained reliable results from undisturbed cores and correlated normal and reversed segments with biostratigraphic zones (see **“Biostratigraphy,”** p. 5). The sediments of Hole 1140A generally have a stable magnetization, which was obtained after AF demagnetization at 10 mT. Most discrete samples have a high median destructive field (MDF), and the remanent direction is stable in demagnetization steps between 10 and 30 mT (Fig. **F39**). We, therefore, used the remanent magnetization, after AF demagnetization at 20 mT, to correlate the paleomagnetic record with geomagnetic chrons. Furthermore, we used the data selection criteria as discussed in **“Paleomagnetism,”** p. 27, in the “Explanatory Notes” chapter for magnetostratigraphic studies of Hole 1140A (Fig. **F40**). The selection criteria were that (1) the intensity of remanent magnetization after AF demagnetization at 20 mT was $>2 \times 10^{-4}$ A/m, (2) the inclination was >±30°, (3) at least two consecutive values (which corresponds to a 10-cm length of split core) had the same polarity, and (4) there was no significant core disturbance. Characteristic inclinations from discrete samples generally agree well with selected inclinations from whole-core measurements (Fig. **F40**).

F36. Close-up photograph of Sample 183-1140A-29R-1 (Piece 2, 85–103 cm), **p. 72.**

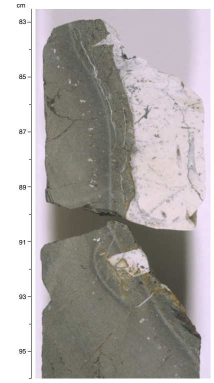

F37. Close-up photograph of Sample 183-1140A-34R-3 (Piece 1, 77–90 cm), **p. 73.**

F38. Close-up photograph of Sample 183-1140A-36R-1 (Piece 3, 112–124 cm), **p. 74.**

F39. AF demagnetization of a discrete sediment sample, **p. 75.**

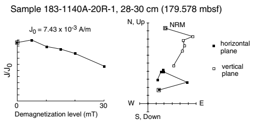

The correlation of biostratigraphic data and polarity reversals (Fig. **F40**) suggests that the reversed and normal chrons in Hole 1140A are middle Miocene to early Oligocene or latest Eocene in age (see **"Biostratigraphy,"** p. 5). We obtained a relatively continuous paleomagnetic record from high-recovery core in the lower part of Unit I (160–250 mbsf; see **"Lithostratigraphy,"** p. 3). The upper part of the unit provides only a limited paleomagnetic record as a result of low recovery and highly disturbed cores. However, we propose the following correlations with paleontological data from the core catcher of each core (see **"Biostratigraphy,"** p. 5). We suggest that the normal and reversed segments between 0 and 143 mbsf lie within middle and early Miocene chrons. The normal and reversed segments between 143 and 230 mbsf correspond to chrons of late Oligocene to early Oligocene age (nannofossil Zone *Ch. altus;* see **"Biostratigraphy,"** p. 5). The normal–reversed sequence at ~230 mbsf may correlate with Chrons C12n/r or C13n/r in the early Oligocene and late Eocene (Section 183-1140A-25R-CC; nannofossil Zones CP16a/b to CP15b; see **"Biostratigraphy,"** p. 5).

We observed high but scattered susceptibilities (whole-core multisensor track [MST] measurements; see **"Physical Properties,"** p. 24) and NRM intensities in the uppermost 10 mbsf (Subunit IA; diatom nannofossil ooze and silty diatom ooze; see **"Lithostratigraphy,"** p. 3) (Fig. **F40**). We observed lower susceptibilities and weaker NRM intensities in Subunit IB (nannofossil ooze and chalk) than in Subunit IA (Figs. **F40, F41**). In Subunit IB (227–245 mbsf), we observed higher magnetic susceptibilities in the lowest part.

Basement Rocks

We observed the magnetic properties of each basement unit (see **"Igneous Petrology and Geochemistry,"** p. 16, and **"Physical Volcanology,"** p. 12) and the variation of magnetic properties within each unit (Fig. **F42**). Three independent types of susceptibility measurements, MST, AMST, and discrete samples, generally show consistent results. We observed no significant differences in average susceptibility and NRM intensity within or between the lava flows (basement Units 1, 2, 3, 5, and 6; Figs. **F41, F42**). Average NRM intensities and range from 3.14 (Unit 1) to 8.91 (Unit 3) A/m. Average susceptibilities range from 0.747 $\times 10^{-3}$ (Unit 2) to 1.25 $\times 10^{-3}$ (Unit 5) SI units. Within the lava flows, we observed constant high susceptibility in three intervals (241–244 mbsf, Unit 1; 296–299 mbsf, Unit 5; and 315–317 mbsf, Unit 6). These intervals are also characterized by a large decrease of intensity after AF demagnetization (low MDF) (Fig. **F42**). Susceptibility was scattered in other parts of the flow units. Unit 4 (dolomite and dolomite-nannofossil-chalk; see **"Lithostratigraphy,"** p. 3) has low susceptibility values (see Figs. **F41, F42**).

We obtained reliable magnetic directions from whole-core measurements after AF demagnetization at 40 mT. We found negative inclinations, indicating a normal magnetic polarity, in basement Unit 1 and positive inclinations, indicating a reversed magnetic polarity, in basement Units 2, 3, 5, and 6. Unit 1 shows a reversed magnetic overprint; hence, it is probably not caused by the Holocene (Brunhes normal epoch) magnetic field. The reversed magnetic component may be secondary, acquired during alteration or drilling. Consistent with the magnetostratigraphy of the overlying sediments, this reversal is late Eocene in age. As a result of problems with the pass-through magnetometer, we have no remanent information for basement Unit 4. Be-

F40. Inclination, intensity, and susceptibility of sediments, **p. 76.**

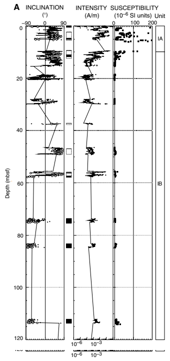

F41. Average intensity and susceptibility of all units, **p. 78.**

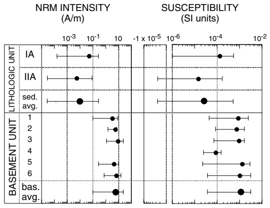

F42. Inclination, intensity, and susceptibility of basement rocks, **p. 79.**

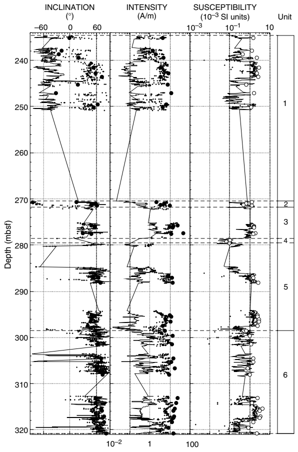

cause of the very strong remanent intensities of the igneous rocks within the same core section of Unit 4, the magnetometer was out of range.

Stepwise AF demagnetization up to 60 mT was applied to the archive-half of Section 183-1140A-37R-4 from Unit 6. We chose a rock (interval 183-1140A-37R-4 [Piece 1, 0–33 cm]) that is longer than the effective sensitivity of the pass-through magnetometer (~15 cm) and analyzed its behavior during demagnetization at 7.5 cm in the section (Fig. F43). The magnetization has a MDF of 20 mT and a two-component magnetization with a stable hard component, as shown by the straight lines in the orthogonal vector projection. Six discrete samples from basement Units 1, 3, 5, and 6 were stepwise thermally demagnetized up to 620°C. We measured the susceptibility of the samples after each heating step to detect changes in their magnetic minerals. We found two types of behavior during thermal demagnetization. Three samples (Samples 183-1140A-27R-2, 83–85 cm; 28R-3, 20–22 cm; and 36R-2, 128–130 cm) show a large decrease in intensity during the low-temperature demagnetization steps. The directions of the magnetization are strongly scattered, and we could not apply component analysis to determine characteristic inclinations (Fig. F44A). Susceptibility measurements show no changes in mineralogy with heating. Three other samples (Samples 183-1140A-32R-1, 94–96 cm; 34R-1, 139–141 cm; and 34R-5, 10–12 cm) display a two-component magnetization. The high-temperature phase is characterized by an unblocking temperature of ~560°C, and the low-temperature phase by an unblocking temperature of ~350°C (Fig. F44B). The high-temperature phase probably corresponds to titanium-poor titanomagnetite, and the low-temperature phase to (titano)maghemite. The magnetization is stable and we determined characteristic inclination values of 52°, 51°, and 63° (see Table T9).

F43. AF demagnetization of a basement archive half, p. 80.

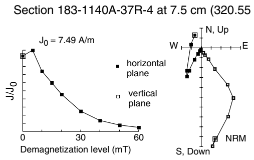

F44. Thermal demagnetization of discrete basement samples, p. 81.

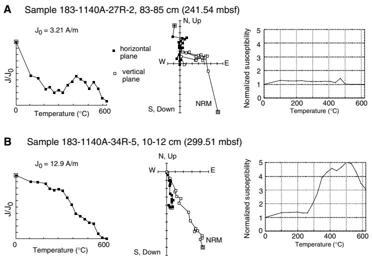

T9. Characteristic inclinations and NRM intensities of discrete basalt samples, p. 112.

PHYSICAL PROPERTIES

Introduction

Physical properties measurements of whole-core sections from Hole 1140A using the MST included magnetic susceptibility, gamma-ray attenuation porosity evaluator (GRAPE) bulk density, and natural gamma radiation (NGR) data. We determined compressional wave velocities (V_p) from the split cores in transverse x directions for soft sediments in liners and for hard-rock pieces without the liner. Measurements in the longitudinal (z) and transverse (x and y) directions on cut samples of consolidated sediment and hard rock allowed us to investigate velocity anisotropy. We estimated the magnitude of velocity anisotropy by dividing differences between the maximum and minimum velocities (among the three mutually perpendicular directions—x, y, and z) by the mean velocity of the sample. Index properties determinations included bulk density, water content, porosity, and grain density. We calculated index properties from wet and dry sample weights and dry volumes. We also determined thermal conductivity for sediment and basalt.

Index Properties

We determined index properties by using gravimetric methods on discrete samples (Table T10). The general trend exhibited by the index

T10. Index properties data, p. 113.

properties data at Site 1140 reflect downhole variations in lithology (Figs. **F45, F46**).

In Subunit IA (seafloor to 10 mbsf), bulk densities vary from 1.4 to 1.5 g/cm³, grain densities range between 2.2 and 2.4 g/cm³, and porosity changes from 66% to 69%. Sediments in this interval consist of middle Miocene diatom-bearing nannofossil ooze (see **"Lithostratigraphy,"** p. 3).

Between ~10 and ~75 mbsf in Subunit IB, bulk densities change little, averaging 1.5 g/cm³. Porosity remains constant at 65% (Fig. **F45C**). Grain densities, however, exhibit large scatter in this interval, with values between 2.3 and 2.6 g/cm³. The lithology in this interval changes from foraminifer-bearing nannofossil ooze at the top of the sequence to semilithified nannofossil chalk at the bottom (the beginning of the ooze-chalk transition zone). The large scatter may reflect the presence of diatoms, which are abundant to 47 mbsf and present until ~200 mbsf. The grain density of sediment consisting of 50% diatoms (opal A) and 50% calcite would be ~2.3 g/cm³.

From 84 to 182 mbsf, still within Subunit IB, bulk density increases slightly from 1.4 to 1.7 g/cm³. Down to ~160 mbsf, grain density is between 2.6 and 2.7 g/cm³, whereas from 160 to 182 mbsf the grain density varies from 2.6 to 2.9 g/cm³. The reason for this scatter is unclear. Porosity decreases from 76% to 62% (Fig. **F45C**). Sediments in this depth interval become progressively stiffer downhole and are mainly greenish nannofossil-bearing ooze and chalk.

Between 184 and 234 mbsf in Subunit IB, index properties change significantly. Bulk density gradually increases from 1.5 to 2.0 g/cm³, grain density gradually increases from 2.6 to 2.9 g/cm³, and porosity gradually decreases from 74% to 44% downhole through this interval. The sediments in this interval are mainly extensively burrowed nannofossil-bearing ooze and chalk. The increase in grain density downhole corresponds to dolomitization (see **"Lithostratigraphy,"** p. 3).

At the boundary between Unit II and basement (~235 mbsf), index properties change abruptly (Figs. **F45, F46**). In basement Unit 1, which consists of pillow and massive basalt (see **"Physical Volcanology,"** p. 12), bulk densities increase to ~2.8 g/cm³, grain densities increase to 2.9 g/cm³, and porosities sharply decreases to 6%.

From 278.9 to 279.5 mbsf, within basement Unit 4, a layer of rusty brown to rusty orange dolomite bed was recovered. The corresponding physical properties data clearly reflect this change in lithology. Bulk density sharply decreases to 2.1 g/cm³, grain density decreases to a mean of 2.8 g/cm³, and porosity increases to a mean of 41%. The difference in grain densities reflect the different degree of dolomitization and variable clay content. The dolomite pieces were fragile and tended to disaggregate when saturated in saltwater. This disaggregation may have been caused by swelling of clays. This swelling, followed by dehydration when dried in oven at 110°C, could also cause the lower bulk density and higher porosity observed in this interval.

In the lowermost part of the basement, Units 5 and 6 (287 to 321 mbsf), bulk densities vary from 2.5 to 3.0 g/cm³ with a mean of 2.9 g/cm³, grain density approaches a mean of 3.0 g/cm³, and porosity varies from 22% to 4% (Fig. **F46**). The lithologies in these units are pillow and massive basalts.

F45. Downhole index properties and V_p, **p. 82.**

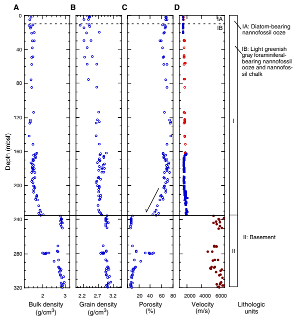

F46. Downhole index properties profiles for discrete samples from basement Units 2–19, **p. 83.**

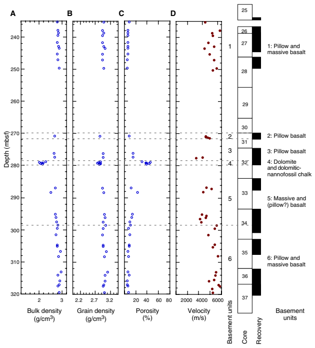

MST Measurements

GRAPE Density

Bulk density was measured by the GRAPE every 4 cm on whole sections of cores recovered from Hole 1140A. In sedimentary Subunits IA and IB (0 to 235 mbsf), the maximum values of GRAPE densities correspond well with wet bulk densities determined from discrete samples. GRAPE densities also show fluctuations that are similar to shallow resistivity values from the logging data (Fig. **F47**) (see **"Downhole Measurements,"** p. 29).

F47. Downhole profiles of MST measurements together with discrete measurements, **p. 84.**

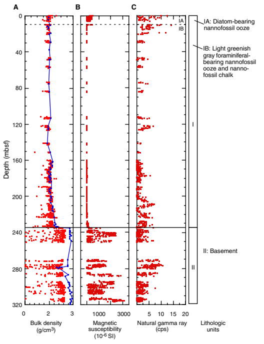

Below ~235 mbsf, bulk densities are much more scattered than in overlying sediments. As with other Leg 183 sites, the larger scatter in the GRAPE bulk density data for the deeper units results from empty space between pieces of core and the core's fractured nature, whereas the generally lower maximum GRAPE values are caused by the smaller diameters of the cores.

Natural Gamma Radiation

We measured NGR every 12 cm on unsplit sections of cores from Site 1140. Between seafloor and 10 mbsf, in Subunit IA, the NGR count fluctuates with a maximum peak near the boundary between Subunits IA and IB (~10 mbsf). Within Subunit IB, we observe two positive peaks of >7 counts per s (cps) at depth ranges centered around ~120 and ~215 mbsf (Fig. **F47**), probably reflecting an increase in clay content. These intervals correspond to the light green chalk (Core 183-1140A-14R) and the light brown nannofossil-bearing chalk (Core 183-1140A-24R), respectively. Gamma-ray values increase to a maximum of 10 cps in basement Units 2 and 3, and to 7 cps in basement Unit 4 (270.5 to 279.7 mbsf). This gamma-ray increase is associated with a decrease in magnetic susceptibility. The remaining basement units have values around 4 cps. The downhole natural gamma-ray profile (MST) exhibit fluctuations very similar to those of downhole spectral gamma-ray logging data (see **"Downhole Measurements,"** p. 29).

Magnetic Susceptibility

We determined magnetic susceptibility on all cores from Site 1140 (Fig. **F47B**). The results are discussed in **"Paleomagnetism,"** p. 22.

Compressional Wave Velocity

We determined compressional wave velocity from both split-core sections and discrete samples (Figs. **F45D, F46D**). Velocity anisotropy in both sedimentary and basaltic units is negligible, typically <4%. The compressional wave velocity data for Subunit IA and the upper sequence of Subunit IB (0–182 mbsf), which consist of diatom-bearing nannofossil ooze and foraminifer-bearing nannofossil ooze and chalk, show very little scatter, with a mean value of ~1633 m/s (Table **T11;** Fig. **F45D**). The compressional wave velocities in the lower part of Unit IB increase gradually with depth, from 1578 to 2018 m/s. These changes correspond to a decrease in porosity from 74% to 44%.

T11. V_p discrete measurements, **p. 115.**

At the boundary between Unit I and basement (~235 mbsf), the compressional wave velocity increases sharply. Velocity in basement Unit 1 varies from 5484 to 6859 m/s. The recovered cores (Cores 183-1140A-

26R through 28R) in this unit are pillow and massive basalts. Velocities between ~6000 and 7000 m/s seem high and may be a consequence of the calibration method (see **"Velocity Determinations,"** p. 36, in the "Explanatory Notes" chapter). Velocities in the bottom of basement Units 5 and 6 typically range from 5099 to 6055 m/s, with few values above 6500 m/s. Velocity, bulk density, and porosity correlate well in Core 183-1140A-34R. Velocity trends correlate with the downhole trends of the sonic log, but discrete velocity values are higher in the basement units.

Thermal Conductivity

Thermal conductivity values for sediments from Subunits IA and IB are commonly between 0.7 and 1.1 W/(m·K), with a mean value of 0.9 W/(m·K), and show little scatter (Fig. F48; Table T12). The mean value is similar to values in sedimentary units at other Leg 183 sites. For the basement units, thermal conductivity values vary quite widely, from a low value of 1.1 W/(m·K) to a high value of 2.4 W/(m·K) in the depth interval from ~235 to 321 mbsf, with a mean value of 1.69 W/(m·K). The highest values were in Sections 183-1140A-27R-2 (~243 mbsf) and 183-1140A-34R-4 (~300 mbsf), which are pillow and massive basalts in basement Units 1 and 6, respectively.

F48. Downhole index properties and V_p, **p. 85.**

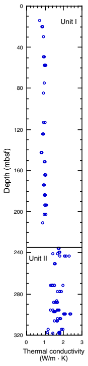

T12. Thermal conductivity values, **p. 117.**

Concluding Discussion

Physical properties at Site 1140 vary downhole and correlate with changes in lithology. Index properties data in sedimentary Subunits IA and the upper part of Subunit IB (0–182 mbsf) show insignificant changes, and compressional wave velocity is fairly uniform. Between 184 and 234 mbsf, within Unit IB, physical properties change noticeably because of lithification. Bulk and grain densities as well as compressional wave velocities gradually increase with depth, with a corresponding decrease in porosity.

All index properties abruptly change at the boundary between basement and overlying sedimentary units. Massive pillow basalts in basement Units 1, 5, and 6 have higher density, velocity, and magnetic susceptibility values than those of pillow basalts in basement Units 2 and 3. Basement Units 2 and 3 have the overall highest natural gamma-ray values.

ORGANIC AND INORGANIC CHEMISTRY

We measured concentrations of carbonate in sediments from Hole 1140A on ~1 sample per core (Table T13). In addition, we analyzed 14 of the sediment samples for organic carbon, total nitrogen, sulfur, and hydrogen. The results of the analyses are discussed in **"Lithostratigraphy,"** p. 3.

For basalts that were analyzed by XRF, we measured total carbon, total nitrogen, sulfur, and hydrogen using the NCS analyzer (Table T14).

T13. Carbon, nitrogen, sulfur, and hydrogen analyses of sediments, **p. 118.**

T14. Carbon, nitrogen, sulfur, and hydrogen analyses of basalts, **p. 119.**

SEISMIC STRATIGRAPHY

Data

We used densities and compressional wave velocity from index properties data and downhole logs (Fig. **F49**) to synthesize seismograms at Site 1140. A detailed comparison of velocities from samples and logs is given in the **"Downhole Measurements,"** p. 54, in the "Site 1137" chapter. Based on coherence analysis of velocity data from Site 1137 (Fig. **F90,** p. 161, in the "Site 1137" chapter), we filtered the sample velocities and densities from Site 1140 using a 5-m-long filter. The data were resampled simultaneously every 2 m, and data gaps >5 m were linearly interpolated. We used a robust mode filter (i.e., a maximum likelihood probability estimator) that calculated the mode within the given data window, as described in **"Seismic Stratigraphy,"** p. 47, in the "Explanatory Notes" chapter.

F49. Comparison of densities determined from core samples and GRAPE, and V_p from downhole logs and core samples, **p. 86.**

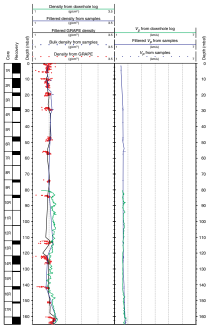

Velocities from downhole logs and discrete samples agree well above 235 mbsf (Fig. **F49**). In the basement section, below 235 mbsf, discrete samples yield higher velocities than log values. The majority of the low-velocity sediments intercalated with pillow basalts, as documented in the FMS images (see **"Downhole Measurements,"** p. 29), were not recovered, resulting in the observed bias in the discrete sample velocities. Within basement, low recovery hampers the spatial resolution of sample density data. High-frequency variations in density and velocity data within basement are fairly coherent and likely represent real downhole variations of physical properties, rather than noise.

The deployment of the WST at this site offered an opportunity to test the integrity of velocities from the downhole log and samples by comparing relationships between depth and two-way traveltime (TWT) derived from the latter two data sets and TWT derived from WST one-way traveltime (Fig. **F50A;** Table **T15**). The comparison illustrates that TWT from sonic velocities and the WST agree well. Above basement (~235 mbsf) TWT derived from sample velocities agree with the other two data sets as well. Within the basement, use of discrete sample velocities results in underestimating TWT because the discrete samples are biased toward higher values (Fig. **F50B**).

F50. Comparison of depth vs. TWT relationships for Sites 1140 and 1139, **p. 88.**

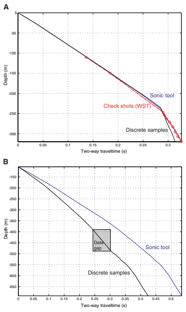

The depth-TWT relationship for Site 1139 juxtaposes TWT derived from the sonic velocity log and from discrete samples (Fig. **F50**). The two functions differ by >100 ms near the bottom of the hole. Comparison of data from Sites 1139 and 1140 emphasizes that (1) TWT based on high-quality sonic logs are accurate, (2) TWT based on velocities from discrete samples are fairly reliable if core recovery is consistently high, and (3) only the WST can resolve differences between transit times from logs and samples.

Synthetic Seismograms

We used velocity and density data from physical properties measurements (0–85 and below 312 mbsf) and from downhole logs (85–312 mbsf) to synthesize seismograms for linking cores and logs with MCS reflection data. We constructed a composite TWT-depth array using TWT from the sonic log above 109 mbsf and WST data below this depth, which corresponds to the shallowest deployment depth of the WST.

We resampled the TWT array linearly using a sampling interval of 0.1 ms, resulting in oversampling to avoid aliasing. We then resampled ve-

T15. Shotpoints and the measured one-way traveltimes of the checkshot survey, **p. 120.**

locities and densities using the resampled TWT array, obtained impedance from the product of velocity and density, and computed reflection coefficients from impedance contrasts (Fig. **F51**). We constructed synthetic seismograms with and without multiples and transmission losses (see **"Seismic Stratigraphy,"** p. 47, in the "Explanatory Notes" chapter). However, at this site we used a Ricker wavelet with a peak frequency of 30 Hz to synthesize seismograms, as the use of higher frequencies results in peaks that are not observed in the MCS data. Comparison of the two synthetic seismograms (Fig. **F51F**) shows that the phase of large-amplitude peaks is nearly identical. However, transmission losses reduce amplitudes in the basement section (Fig. **F51F**, red trace). The sedimentary section does not include any high-amplitude reflections caused by a lack of substantial impedance contrasts (Fig. **F51C**).

F51. Composite of core recovery, lithostratigraphy, and age data, **p. 89.**

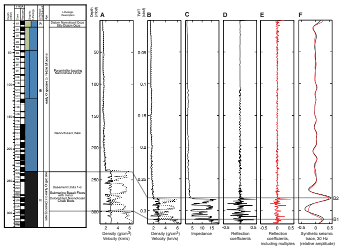

Seismic Stratigraphy

The synthetic seismogram, including transmission losses, matches the MCS data extremely well (Fig. **F52**). Igneous basement is represented by reflection B2, which corresponds to pillow basalts underlying dolomite (see Fig. **F15**). Reflection B1 represents the transition from the massive sheet flow of basement Unit 5 to pillow basalts of basement Unit 6 (Fig. **F15**).

F52. Seismic reflection data and a synthetic seismic trace, **p. 91.**

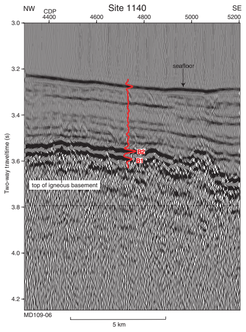

DOWNHOLE MEASUREMENTS

Logging Operations

Three different logging runs were successful at Site 1140 (Table **T16**) (see **"Operations,"** p. 2). The first run included the triple combo, consisting of the DITE, the APS, the HLDS, as well as the HNGS and the LDEO-TAP tools. We completed two passes in the basement section; the main log was recorded from 321.2 to 0 mbsf, and a repeat section from 321.2 to 225 mbsf. The tools encountered no ledges or bridges. We attempted to log the seafloor depth, but as at Site 1137, calcareous ooze and seawater showed no contrast in natural gamma radiation. The driller's pipe depth was 2486 meters below rig floor (mbrf), and the logging data recorded the pipe at 2488 mbrf. Instead of shifting the logging data to the driller's seafloor at 2406 mbrf, we shifted the data with respect to the pipe and assumed that the depth of the seafloor was at 2408 mbrf.

T16. Summary of logging operations, **p. 121.**

For the second run, we deployed the FMS, the LSS, and the NGT tool combination and completed two passes in the basement and one pass in the sedimentary section. Although the tools did not contact the borehole wall through most of the sedimentary section (diameter = >15 in), we continued logging to obtain velocity data.

The third run employed the WST. We used a 300-in^3 air gun, which produced good signals into basement. The source offset was 49.0 m. In basement, we chose eight locations clamping the tools every ~10 m. In the sediments, the WST would only clamp at two depths because the hole was too large and/or the tool did not stay in position.

Log Quality

Data from the first two logging runs (Fig. **F53**) are of good quality. The calipers of the HLDS and the FMS show that the hole was enlarged, >15 in (38 cm) above 227 mbsf, whereas in basement the hole was in excellent condition. Small breakouts in a few discrete intervals correspond to sedimentary interbeds. Unfortunately, all data from the HNGS are not useful. The tool's spectrum was shifted for some reason and gave erroneous counts that cannot be corrected. However, the natural gamma-ray data from the second run are of high quality. Ship heave generally needs to be taken into account because it might have caused shifts between different logging runs.

Discrete core measurements and logged density, compressional wave, and natural gamma-ray data (Fig. **F54**) agree well both in sediments and basement. In the sediments of lithologic Unit I, all curves show the same trends with no offset or depth mismatch. In igneous basement, recovery was poor and cores should be shifted for a better fit (e.g., low core densities at 278.7–279.2 mbsf [Section 183-1140A-32R-3] were measured in Unit 4 [see **"Physical Properties,"** p. 24], which is a sedimentary interlayer [see **"Lithostratigraphy,"** p. 3] corresponding to a depth of ~283 mbsf in the logging data). The NGR of the rocks detected by both downhole measurements and the core measurements correlates well in the sedimentary section. In the basement section, the minimum and maximum values correspond generally, but because of the low core recovery, the core data are slightly shifted. The velocity data were corrected for cycle skipping. They agree well with velocities determined from core samples (Fig. **F54**) (see **"Seismic Stratigraphy,"** p. 28).

The check-shot survey with the WST yielded excellent data for time-depth conversion (Table **T15**). For further information, see **"Seismic Stratigraphy,"** p. 28.

To orient structural measurements of Site 1140 cores (see **"Alteration and Weathering,"** p. 19) and to determine true thicknesses of lithologic units, we need oriented downhole images. The FMS images show sediment interbeds, fractures, vesicles, and structural features of the pillow lavas. The FMS data are of low quality in the sedimentary section because the FMS pads did not contact the wall of the enlarged borehole. This was as expected based on the caliper data from the first run.

Results

The sediment/igneous basement boundary at 235.8 mbsf is marked by a significant increase in density, resistivity, velocity, and a decrease in porosity (Fig. **F55**). Logging data help delineate the five lava units and the sedimentary interbeds in basement. The basalts generally have densities of 2.8–3.0 g/cm^3, resistivities of 20–200 Ωm, porosities of <20%, and compressional wave velocities of 5–6 km/s. In the sediments, densities are <2.0 g/cm^3, resistivities range from 0.5 to 2 Ωm, porosities from 60%–80%, and compressional wave velocities are <4 km/s (Fig. **F56A, F56B**). Sediments interbedded with lava flows show intermediate physical properties, probably because of greater consolidation compared with sediment overlying basement. Different lithologies identified in the logging data correlate with units identified in the recovered rocks (Table **T17**).

The top of the igneous basement consists of both pillows and massive basalts producing distinguishable FMS images. The pillow contacts with wider (>40 cm) voids show clearly in density, resistivity, and po-

F53. Logging data, **p. 92.**

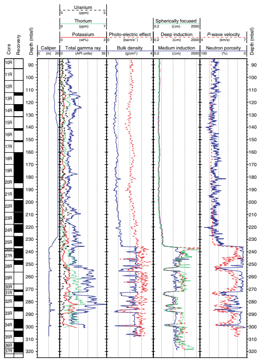

F54. Comparison of densities determined from downhole logs, **p. 93.**

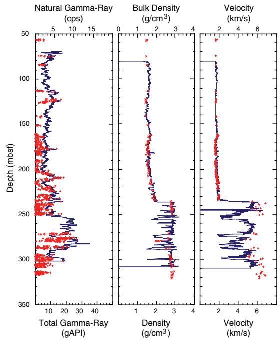

F55. Composite of wireline logs compared to the core-derived lithostratigraphy, **p. 94.**

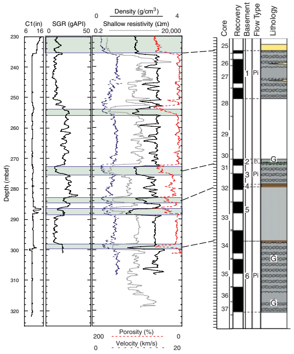

F56. Crossplots of density vs. porosity and shallow resistivity vs. V_p, **p. 95.**

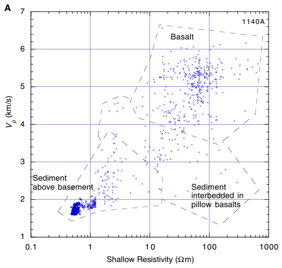

rosity logs. The thicknesses and relative positions of the pillowed and massive lavas correlate with the rocks recovered from basement Unit 1 in Cores 183-1140A-25R to 28R. At the bottom of basement Unit 1, in the portion not recovered in cores, a 2.4-m-thick zone with both pillows and pods of sediments appears in the FMS data. This might indicate that basement Unit 1 flowed over the underlying sediments and partially sank into them. The lack of thick sediment fill between the pillows above this points argues against sediments infilling after the pillows were emplaced. The sediments from 253.4 to 255.5 mbsf appear homogeneous in the FMS data; we assume that they separate basement Units 1 and 2 (Fig. **F55**).

Only 1.27 m of pillow basalts was recovered from basement Unit 2, but the downhole measurements show that this unit is 10.9 m thick and includes a 1.3-m-thick massive lava (Fig **F55**). Basement Unit 2 lavas are the most phenocryst rich at Site 1140, but this did not produce any significant change in the physical properties of the lava. However, natural gamma-ray intensity is elevated compared to basement Unit 1 (Fig. **F55**), which is related to the primary composition of the lava (see **"Igneous Petrology and Geochemistry,"** p. 16). The FMS images of basement Unit 2 show the pillowed character of the lava flows (Fig. **F57**).

The top of basement Unit 3 consists of a small piece of greenish sediment in the recovered core (see **"Lithostratigraphy,"** p. 3). In the logging data, this sedimentary layer is 2.4 m thick (Fig **F55**). The FMS image appears speckled; this could be caused by mottles, burrows, coarse sediment grains, or concretions (Fig. **F58**). The sediments are also characterized by low total gamma-ray signature (SGR) values (~12 gAPI), increased porosity and low density, resistivity, and velocity values, comparable to the ranges in the calcareous sediments above basement (Fig **F55**). This minimizes the possibility that the sediment is dominantly hyaloclastite. Furthermore, caliper measurements indicate that the hole was in good condition in this interval, suggesting very competent sediment.

The lava in basement Unit 3 consists solely of pillows, and, therefore, its physical properties vary widely. The marginally lower resistivity and density might be related to the slightly higher vesicularity of this unit (see **"Physical Volcanology,"** p. 12). The elevated total gamma-ray readings are caused by increased potassium and thorium values (Fig. **F53**), which are related to the primary composition of the lavas (see **"Igneous Petrology and Geochemistry,"** p. 16).

Below basement Unit 3, a thin package of lava is sandwiched between two sediment layers (Fig. **F59**). The upper sediment layer probably corresponds to basement Unit 4, which consists of dolomite and dolomitic nannofossil chalk (see **"Lithostratigraphy,"** p. 3). In the FMS data, we see no pillow structures within the sandwiched lava. This lava might have been recovered as the altered (orange) uppermost lava in basement Unit 5 (Section 183-1140A-33R-1) (see **"Alteration and Weathering,"** p. 19) (Fig. **F10;** Table **T17**). Caliper measurements show an enlarged hole in the lower sediment layer (Fig. **F59**), which suggests that it is soft, thus explaining why it was not recovered.

Beneath the sediment layers, basement Unit 5 is massive lava with relatively homogeneous physical properties. This correlates with the thick, massive lowermost lobe recovered in core (see **"Physical Volcanology,"** p. 12). Near the base of basement Unit 5, planar fractures are well imaged by the FMS (Fig. **F60**). These fractures all dip in a direction of ~240°. We interpret vertical features to be pipe vesicles or fingers of

T17. Depths of basement unit boundaries from FMS data, **p. 122.**

F57. FMS image displaying typical pillow lava structures in basement Unit 2, **p. 97.**

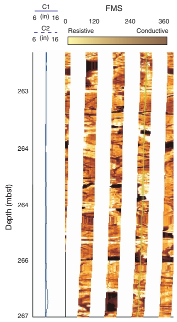

F58. FMS image displaying basement Units 2 and 3, **p. 98.**

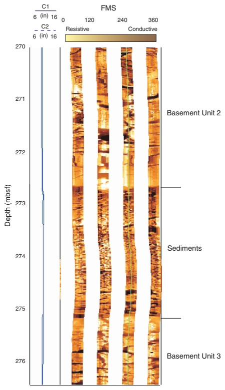

F59. FMS image displaying two sedimentary layers with a intervening lava flow, **p. 99.**

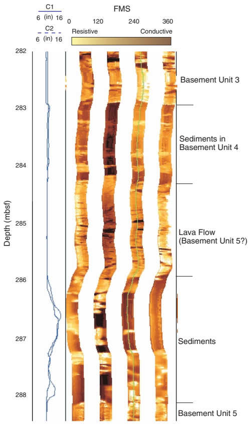

late-stage segregations seen in Section 183-1140A-34R-3 (see **"Alteration and Weathering,"** p. 19, and **"Physical Volcanology,"** p. 12).

The logging data show that the small piece of orange dolomite between basement Units 5 and 6 is from a ~1-m-thick sediment layer (Fig. **F60**). Although the FMS data essentially cover the entire drilled interval of basement Unit 6, not all instruments were able to reach the bottom of the hole. We acquired no data from the natural gamma-ray tool within basement Unit 6. The FMS images show that basement Unit 6 is a mix of pillowed and massive basalt. The 3-m-thick massive portion of basement Unit 6 is also seen in the recovered core.

Comparing the different lava units, we find that gamma-ray values are lowest in the basalts of basement Units 1 and 5. This is related to primary geochemical differences. This observation is consistent with XRF analyses, in which the highest potassium values were detected in basement Units 2 and 3 (see **"Igneous Petrology and Geochemistry,"** p. 16). In general recovery of massive lava was somewhat better than that of pillows (45%–100% vs. 12%–79%).

F60. FMS image displaying the transition from basement Units 5–6, **p. 100.**

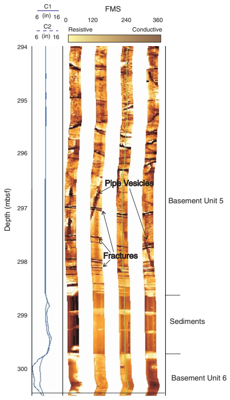

REFERENCES

Alibert, C., 1991. Mineralogy and geochemistry of a basalt from Site 738: implications for the tectonic history of the southernmost part of the Kerguelen Plateau. *In* Barron, J., Larsen, B., et al., *Proc. ODP, Sci. Results,* 119: College Station, TX (Ocean Drilling Program), 293–298.

Alt, J.C., Honnorez, J., Laverne, C., and Emmermann, R., 1986. Hydrothermal alteration of a 1 km section through the upper oceanic crust, Deep Sea Drilling Project Hole 504B: mineralogy, chemistry, and evolution of seawater-basalt interactions. *J. Geophys. Res.,* 91:10309–10335.

Alt, J.C., and Teagle, D.A.H., 1999. The uptake of carbon during alteration of ocean crust. *Geochim. Cosmochim. Acta,* 63:1527–1535.

Berggren, W.A., 1992. Neogene planktonic foraminifer magnetobiostratigraphy of the southern Kerguelen Plateau (Sites 747, 748, and 751). *In* Wise, S.W., Jr., Schlich, R., et al., *Proc. ODP, Sci. Results,* 120 (Pt. 2): College Station, TX (Ocean Drilling Program), 631–647.

Berggren, W.A., Kent, D.V., Swisher, C.C., III, and Aubry, M.-P., 1995. A revised Cenozoic geochronology and chronostratigraphy. *In* Berggren, W.A., Kent, D.V., Aubry, M.-P., and Hardenbol, J. (Eds.), *Geochronology, Time Scales and Global Stratigraphic Correlation.* Spec. Publ.—Soc. Econ. Paleontol. Mineral. (Soc. Sediment. Geol.), 54:129–212.

Coccioni, R., Monaco, P., Monechi, S., Nocchi, M., and Parisi, G., 1988. Biostratigraphy of the Eocene-Oligocene boundary at Massignano (Ancona, Italy). *In* Premoli Silva, I., Coccioni, R., and Montanari, A. (Eds.), *The Eocene-Oligocene Boundary in the Marche-Umbria Basin (Italy).* Int. Subcomm. Paleogr. Strat., Eocene/Oligocene Meeting, Spec. Publ., II, 1:59–80.

Davies, H.L., Sun, S.-S., Frey, F.A., Gautier, I., McCulloch, M.T., Price, R.C., Bassias, Y., Klootwijk, C.T., and Leclaire, L., 1989. Basalt basement from the Kerguelen Plateau and the trail of the DUPAL plume. *Contrib. Mineral. Petrol.,* 103:457–469.

Fisher, R.L., 1997. Bathymetry of the Southern Indian Ocean. *General Bathymetric Chart of the Oceans.* GEBCO, Sheet 97.1.

Fisk, M.R., Giovannoni, S.J., and Thorseth, I.H., 1998. Alteration of oceanic volcanic glass: textural evidence of microbial activity. *Science,* 281:978–980.

Fitton, J.G., Saunders, A.D., Larsen, L.M., Hardarson, B.S., and Norry, M.J., 1998. Volcanic rocks from the southeast Greenland Margin at 63°N: composition, petrogenesis, and mantle sources. *In* Saunders, A.D., Larsen, H.C., and Wise, S.W., Jr. (Eds.), *Proc. ODP, Sci. Results,* 152: College Station, TX (Ocean Drilling Program), 331–350.

Fitton, J.G., Saunders, A.D. Norry, M.J., Hardarson, B.S., and Taylor, R., 1997. Thermal and chemical structure of the Iceland plume. *Earth Planet. Sci. Lett.,* 153:97–208.

Fouquet, Y., Zierenberg, R.A., Miller, D.J., et al., 1998. *Proc. ODP, Init. Repts.,* 169: College Station, TX (Ocean Drilling Program).

Giret, A., and Beaux, J.-F., 1984. The plutonic massif of Val Gabbro (Kerguelen Islands), a tholeiitic complex related to the activity of the East-Indian paleo-ridge. *C. R. Acad. Sci. Ser. 2,* 299:965–970.

Giret, A., and Lameyre, J., 1983. A study of Kerguelen plutonism: petrology, geochronology and geological implications. *In* Oliver, R.L., James, P.R., and Jago, J.B. (Eds.), *Antarctic Earth Science:* Cambridge (Cambridge Univ. Press), 646–651.

Gregg, T.K.P., and Fink, J.H., 1995. Quantification of submarine lava-flow morphology through analog experiments. *Geology,* 23:73–76.

Le Bas, M.J., Le Maitre, R.W., Streckeisen, A., and Zanettin, B., 1986. A chemical classification of volcanic rocks based on the total alkali-silica diagram. *J. Petrol.,* 27:745–750.

Macdonald, G.A., and Katsura, T., 1964. Chemical composition of Hawaiian lavas. *J. Petrol.,* 5:82–133.

Mahoney, J.J., Jones, W.B., Frey, F.A., Salters, V.J.M., Pyle, D.G., and Davies, H.L., 1995. Geochemical characteristics of lavas from Broken Ridge, the Naturaliste Plateau and southernmost Kerguelen Plateau: Cretaceous plateau volcanism in the Southeast Indian Ocean. *Chem. Geol.,* 120:315–345.

Mehl, K.W., Bitschene, P. R., Schminke, H.-U., and Hertogen, J., 1991. Composition, alteration, and origin of the basement lavas and volcaniclastic rocks at Site 738, southern Kerguelen Plateau. *In* Barron, J., Larsen, B., et al., *Proc. ODP, Sci. Results,* 119: College Station, TX (Ocean Drilling Program), 299–322.

Nicolaysen, K., Frey, F.A., Hodges, K.V., Weis, D., and Giret, A., in press. ^{40}Ar/^{39}Ar geochronology of flood basalts from the Kerguelen Archipelago, southern Indian Ocean: implication for Cenozoic eruption rates of the Kerguelen plume. *Earth Planet. Sci. Lett.*

Nicolaysen, K., Frey, F.A., Hodges, K., Weis, D., Giret, A., and Leyrit, H., 1996. ^{40}Ar/^{39}Ar geochronology of flood basalts forming the Kerguelen Archipelago. *Eos,* 77:824.

Royer, J.-Y., and Coffin, M.F., 1992. Jurassic to Eocene plate tectonic reconstructions in the Kerguelen Plateau region. *In* Wise, S.W., Jr., Schlich, R., et al., *Proc. ODP, Sci. Results,* 120: College Station, TX (Ocean Drilling Program), 917–928.

Royer, J.-Y., and Sandwell, D.T., 1989. Evolution of the eastern Indian Ocean since the Late Cretaceous: constraints from GEOSAT altimetry. *J. Geophys. Res.,* 94:13755–13782.

Salters, V.J.M., Storey, M., Sevigny, J.H., and Whitechurch, H., 1992. Trace element and isotopic characteristics of Kerguelen-Heard Plateau basalts. *In* Wise, S.W., Jr., Schlich, R., et al., *Proc. ODP, Sci. Results,* 120: College Station, TX (Ocean Drilling Program), 55–62.

Sandwell, D.T., and Smith, W.H.F., 1997. Marine gravity anomaly from Geosat and ERS-1 satellite altimetry. *J. Geophys. Res.,* 102:10039–10054.

Shipboard Scientific Party, 1989. Site 737. *In* Barron, J., Larsen, B., et al., *Proc. ODP, Init. Repts.,* 119: College Station, TX (Ocean Drilling Program), 159–227.

Storey, M., Kent, R.W., Saunders, A.D., Salters, V.J., Hergt, J., Whitechurch, H., Sevigny, J.H., Thirlwall, M.F., Leat, P., Ghose, N.C., and Gifford, M., 1992. Lower Cretaceous volcanic rocks on continental margins and their relationship to the Kerguelen Plateau. *In* Wise, S.W., Jr., Schlich, R., et al., *Proc. ODP, Sci. Results,* 120: College Station, TX (Ocean Drilling Program), 33–53.

Sun, S.-S., and McDonough, W.F., 1989. Chemical and isotopic systematics of oceanic basalts: implications for mantle composition and processes. *In* Saunders, A.D., and Norry, M.J. (Eds.), *Magmatism in the Ocean Basins.* Geol. Soc. Spec. Publ. London, 42:313–345.

Teagle, D.A.H., Alt, J.C., Bach, W., Halliday, A.N., and Erzinger, J., 1996. Alteration of upper ocean crust in a ridge-flank hydrothermal upflow zone: mineral, chemical, and isotopic constraints from Hole 896A. *In* Alt, J.C., Kinoshita, H., Stokking, L.B., and Michael, P.J. (Eds.), *Proc. ODP, Sci. Results,* 148: College Station, TX (Ocean Drilling Program), 119–150.

Wei, W., 1992. Paleogene chronology of Southern Ocean drill holes: an update. *In* Kennett, J.P., and Warnke, D.A. (Eds.), *The Antarctic Paleoenvironment: a Perspective on Global Change.* Antarct. Res. Ser., 56:75–96.

Wei, W., and Thierstein, H.R., 1991. Upper Cretaceous and Cenozoic calcareous nannofossils of the Kerguelen Plateau (southern Indian Ocean) and Prydz Bay (East Antarctica). *In* Barron, J., Larsen, B., et al., *Proc. ODP, Sci. Results,* 119: College Station, TX (Ocean Drilling Program), 467–494.

Wei, W., and Wise, S.W., Jr., 1992. Selected Neogene calcareous nannofossil index taxa of the Southern Ocean: biochronology, biometrics, and paleoceanography. *In* Wise, S.W., Jr., Schlich, R., et al., *Proc. ODP, Sci. Results,* 120: College Station, TX (Ocean Drilling Program), 523–537.

Weis, D., Bassias, Y., Gautier, I., and Mennessier, J.-P., 1989. DUPAL anomaly in existence 115 Ma ago: evidence from isotopic study of the Kerguelen Plateau (South Indian Ocean). *Geochim. Cosmochim. Acta,* 53:2125–2131.

Weis, D., Frey, F.A., Giret, A., and Cantagrel, J.M., 1998. Geochemical characteristics of the youngest volcano (Mount Ross) in the Kerguelen Archipelago: inferences for magma flux and composition of the Kerguelen plume. *J. Petrol.,* 39:973–994.

Weis, D., Frey, F.A., Leyrit, H., and Gautier, I., 1993. Kerguelen Archipelago revisited: geochemical and isotopic study of the Southeast Province lavas. *Earth Planet. Sci. Lett.,* 118:101–119.

Wise, S.W., Jr., 1983. Mesozoic and Cenozoic calcareous nannofossils recovered by Deep Sea Drilling Project Leg 71 in the Falkland Plateau region, Southwest Atlantic Ocean. *In* Ludwig, W.J., Krasheninnikov, V.A., et al., *Init. Repts. DSDP,* 71 (Pt. 2): Washington (U.S. Govt. Printing Office), 481–550.

Yang, H.-J., Frey, F.A., Weis, D., Giret, A., Pyle, D., and Michon, G., 1998. Petrogenesis of the flood basalts forming the northern Kerguelen Archipelago: implications for the Kerguelen plume. *J. Petrol.,* 39:711–748.

Figure F1. Satellite-derived free-air gravity map of the Kerguelen Plateau (after Sandwell and Smith, 1997). The five plateau province sectors are northern, central, southern, Elan Bank, and Labuan Basin (outlined in white). Leg 183 and previous (Legs 119 and 120) ODP sites are indicated by stars and circles, respectively (black = basement sites; white = sediment sites). Squares indicate dredge and piston core sites where igneous rock (black) and sediment (white) were recovered. (**Figure shown on next page.**)

Figure F1. (Caption shown on previous page.)

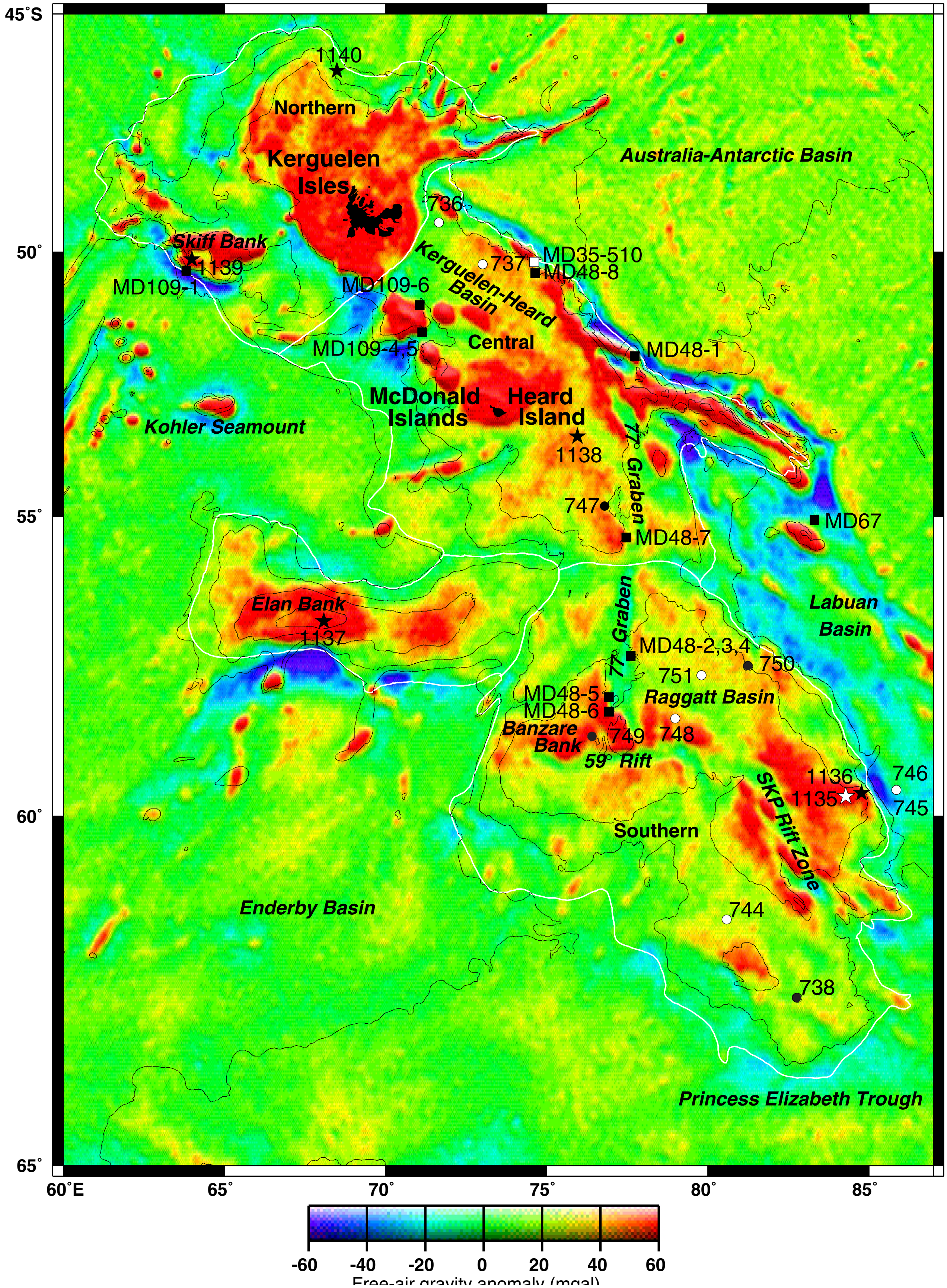

Figure F2. Location of Site 1140 and site-survey data. Navigation for *Marion Dufresne* survey 109, line 05 and line 06 (MD109-05, -06) data is shown in shotpoints. Bathymetric contour interval = 500 m (Fisher, 1997).

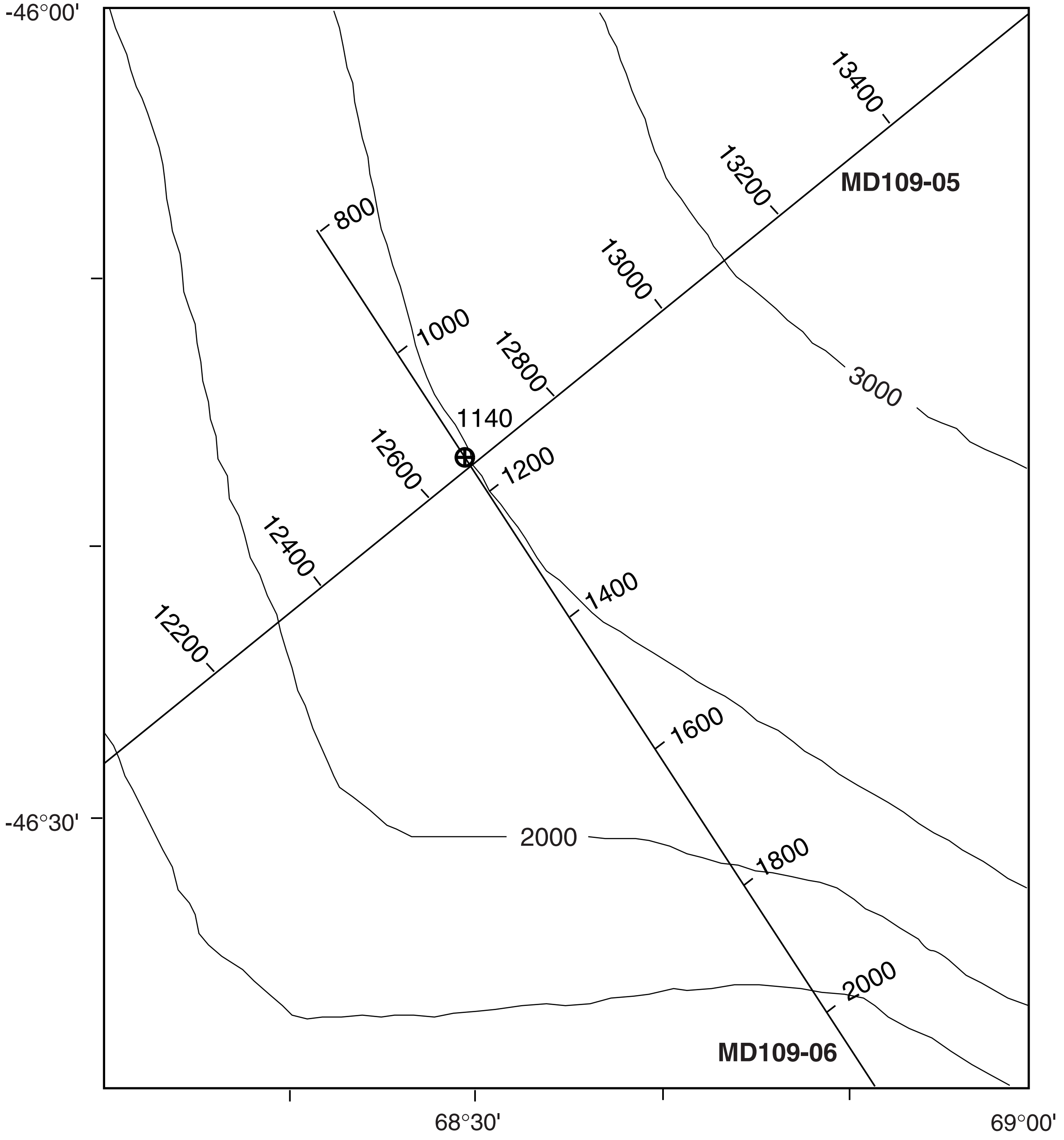

Figure F3. *Marion Dufresne* MD109-06 multichannel seismic profile across Site 1140. Vertical exaggeration = ~16 at the seafloor.

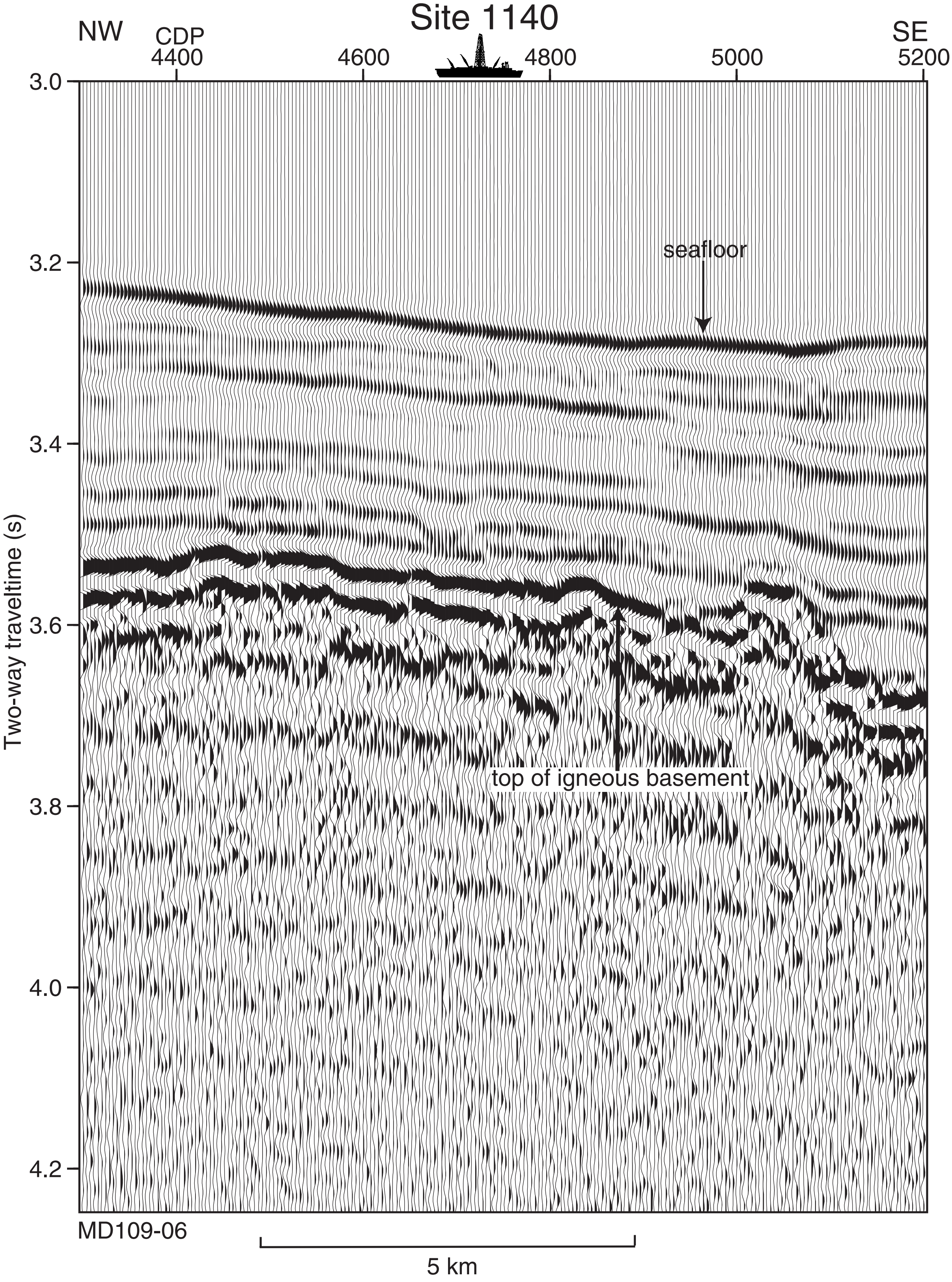

Figure F4. Composite stratigraphic section for Site 1140 showing core recovery, a simplified summary of lithology, lithologic unit boundaries, ages of units, and names of lithologies. The lithologic symbols are explained in Figure F3, p. 57, in the "Explanatory Notes" chapter.

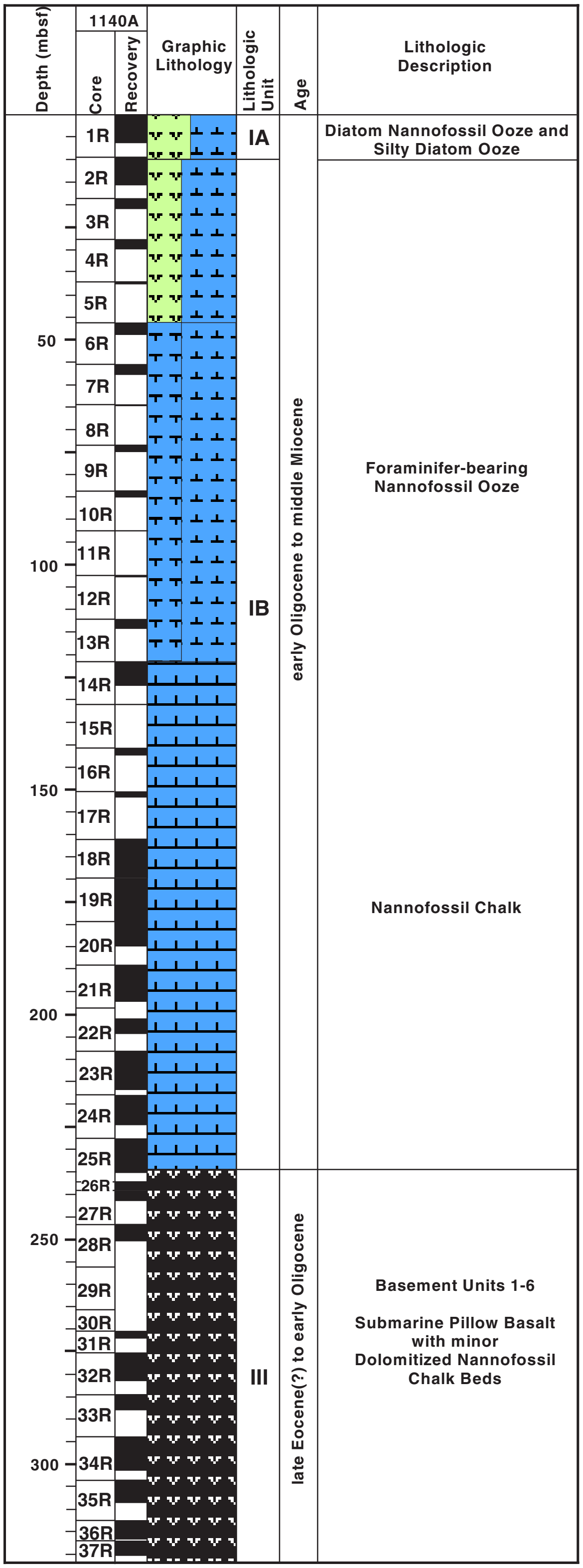

Figure F5. Site 1140 age-depth plot.

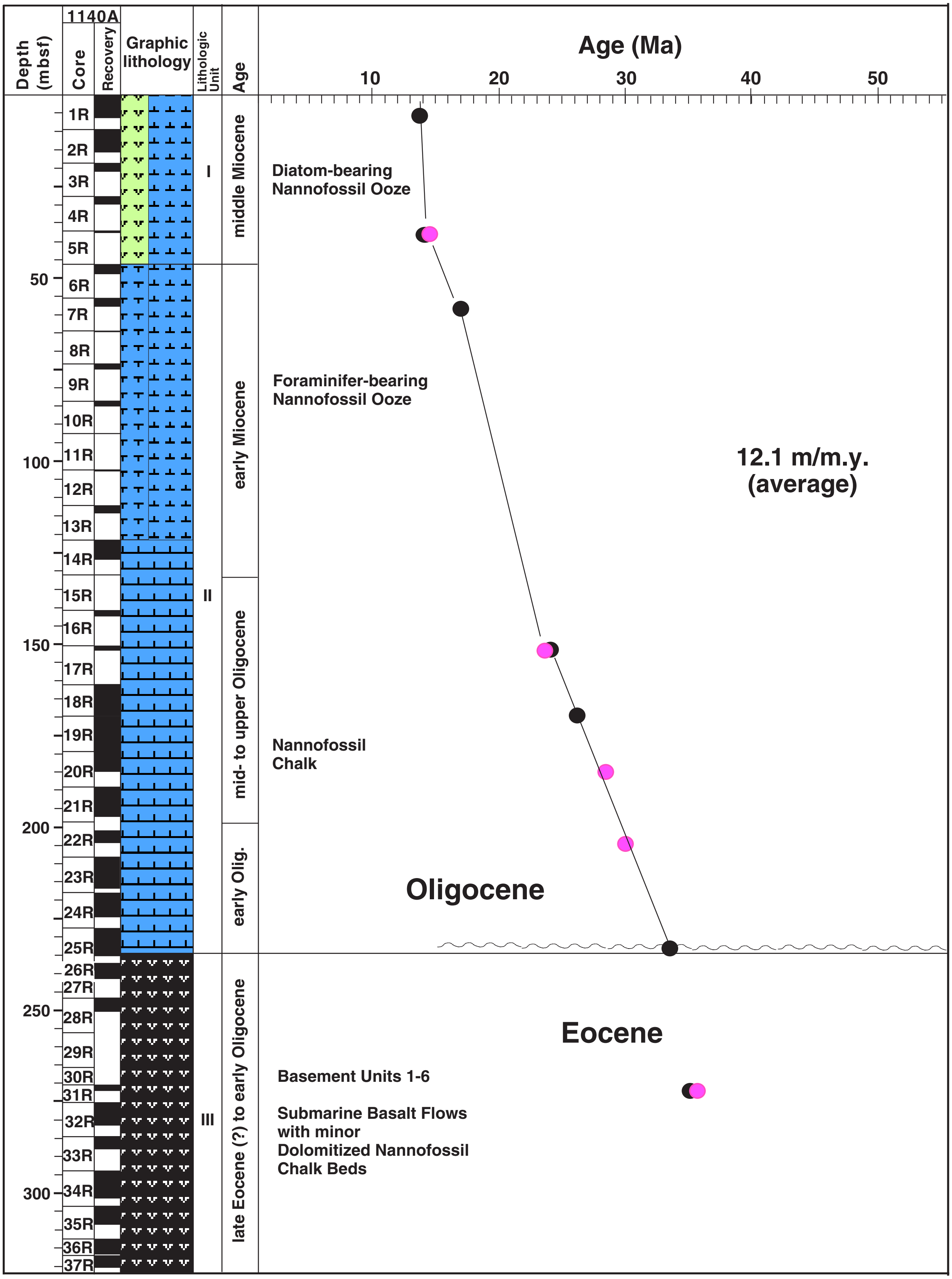

Figure F6. Close-up photograph of interval 183-1140A-26R-1, 0–10 cm. Note the calcite band that separates the identical thicknesses of the two chilled margins from two different pillows of basement Unit 1.

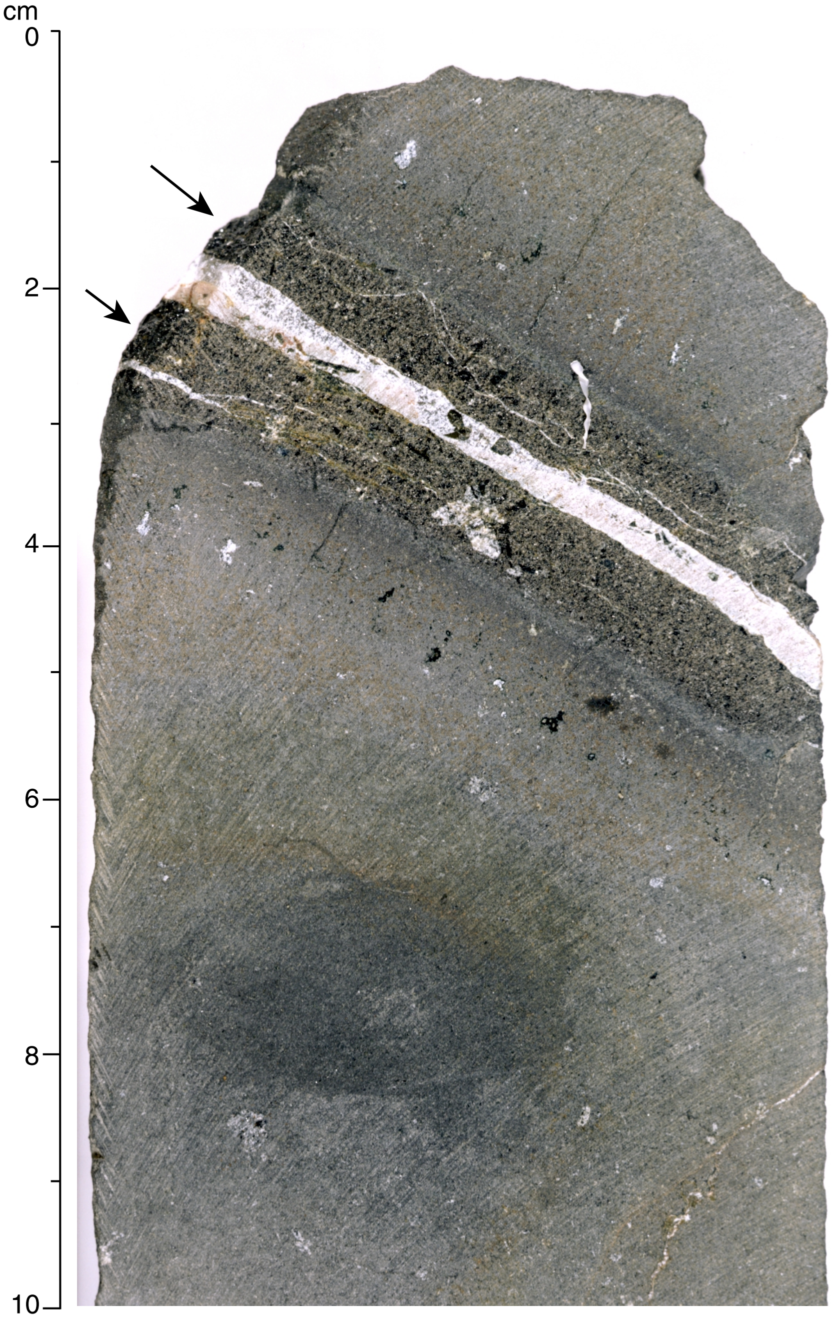

Figure F7. Vesicle distribution in the thickest lobe of basement Unit 1.

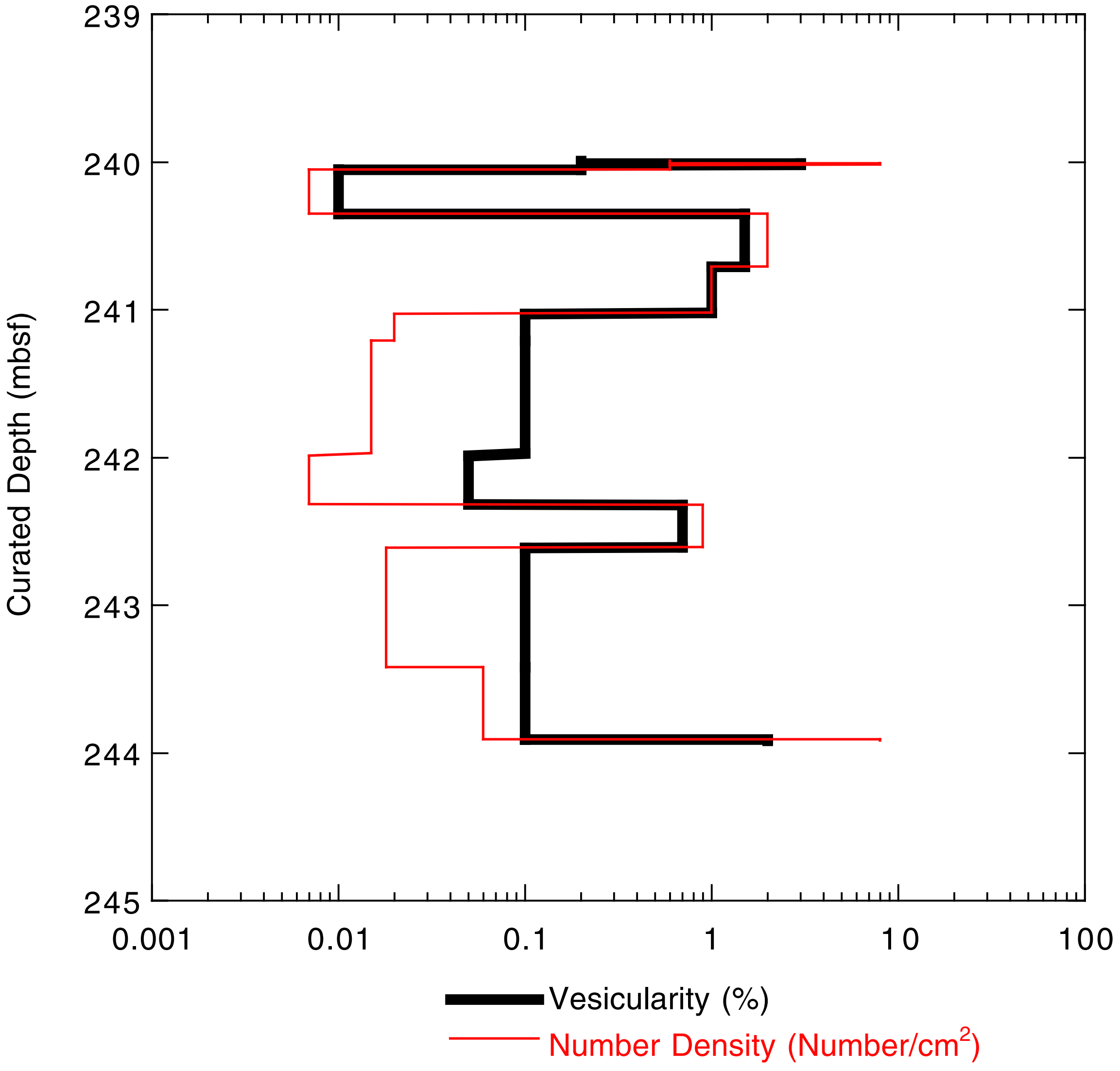

Figure F8. Close-up photograph of Sample 183-1140A-32R-2 (Pieces 18 and 19, 126–137 cm) (working half) showing irregular pipe vesicles in basement Unit 3. Side view (lower piece) and top view (upper piece) show a cylindrical cross section of the pipe vesicle and the pyrite filling.

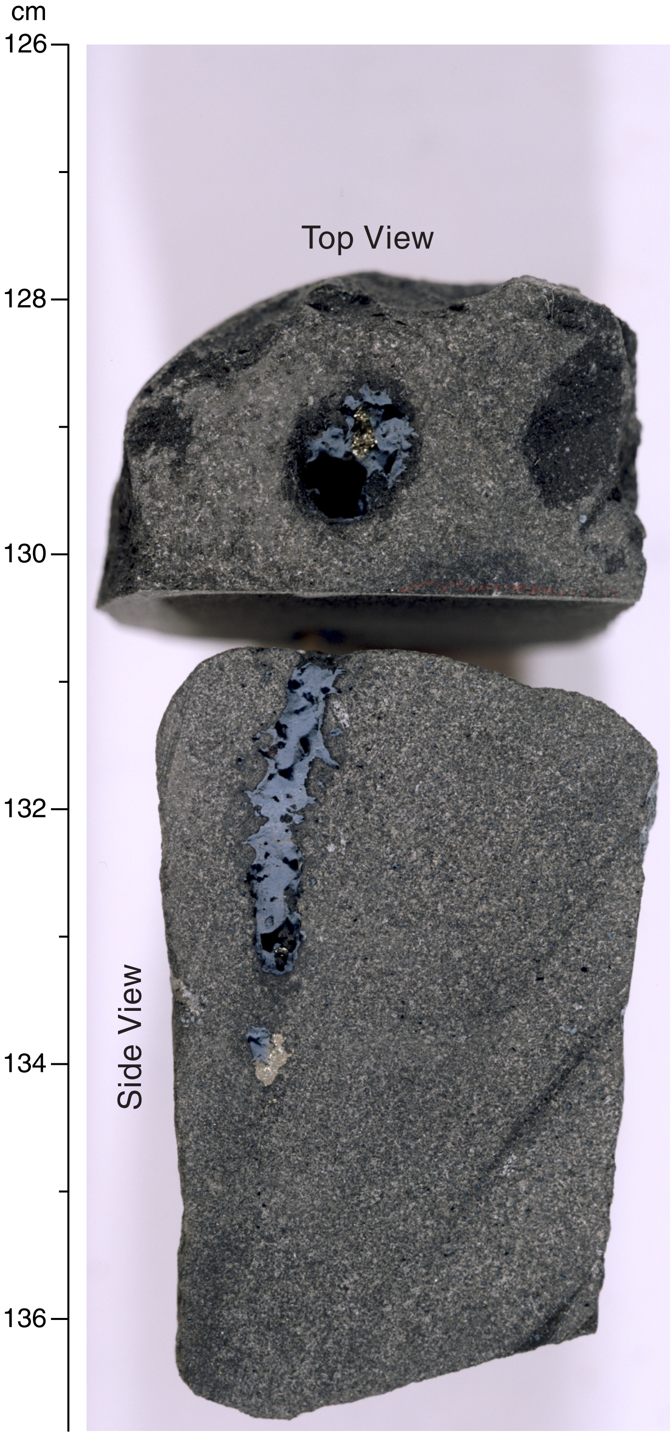

Figure F9. Vesicle distribution through a segment of basement Unit 3.

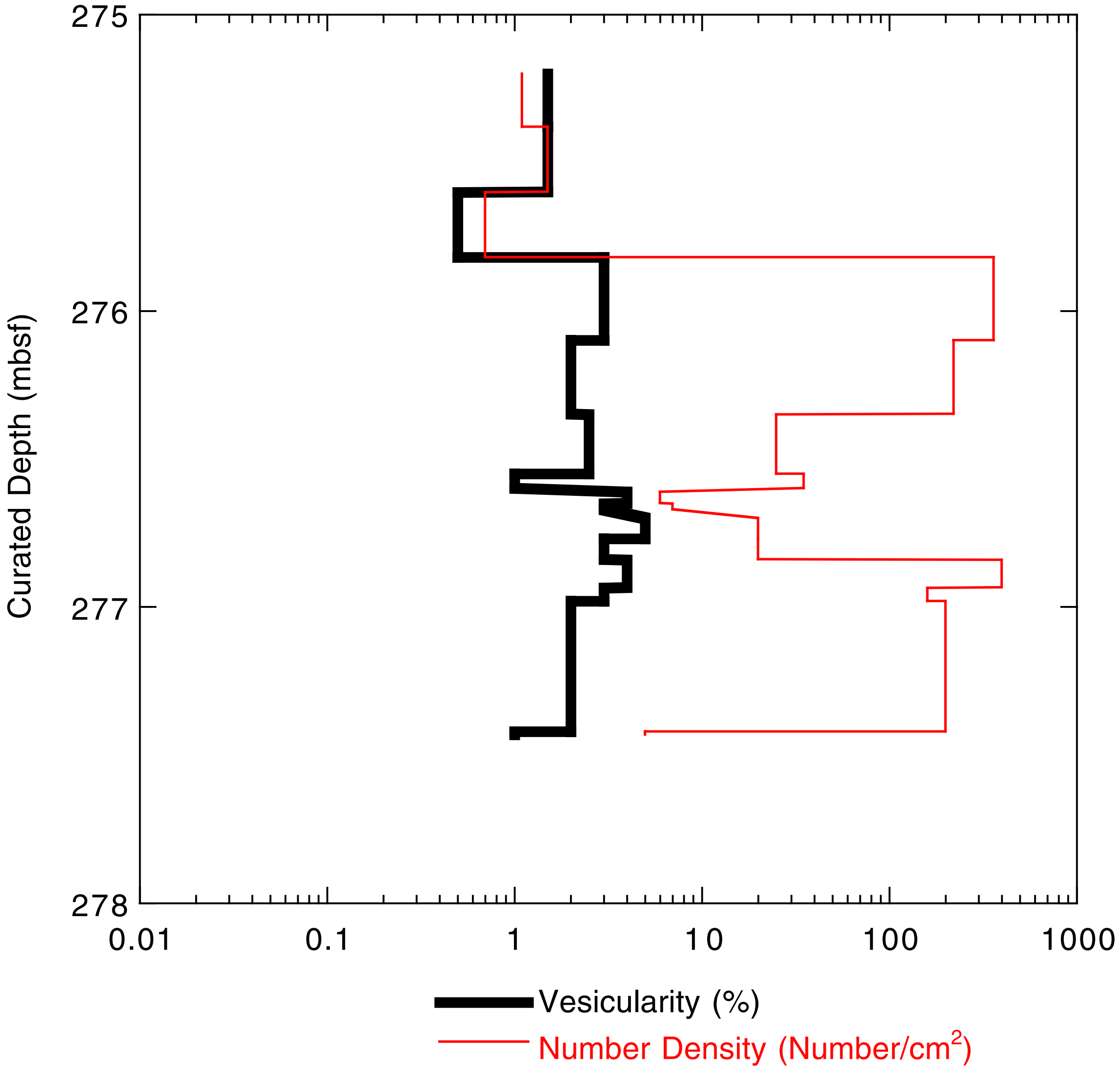

Figure F10. Digital close-up photograph of interval 183-1140A-33R-1, 31–45 cm. Note the chilled margin in the upper part of basement Unit 5 with glass altered to an orange color. This altered margin is likely to have underlain the unrecovered sedimentary interbed seen in the downhole measurements.

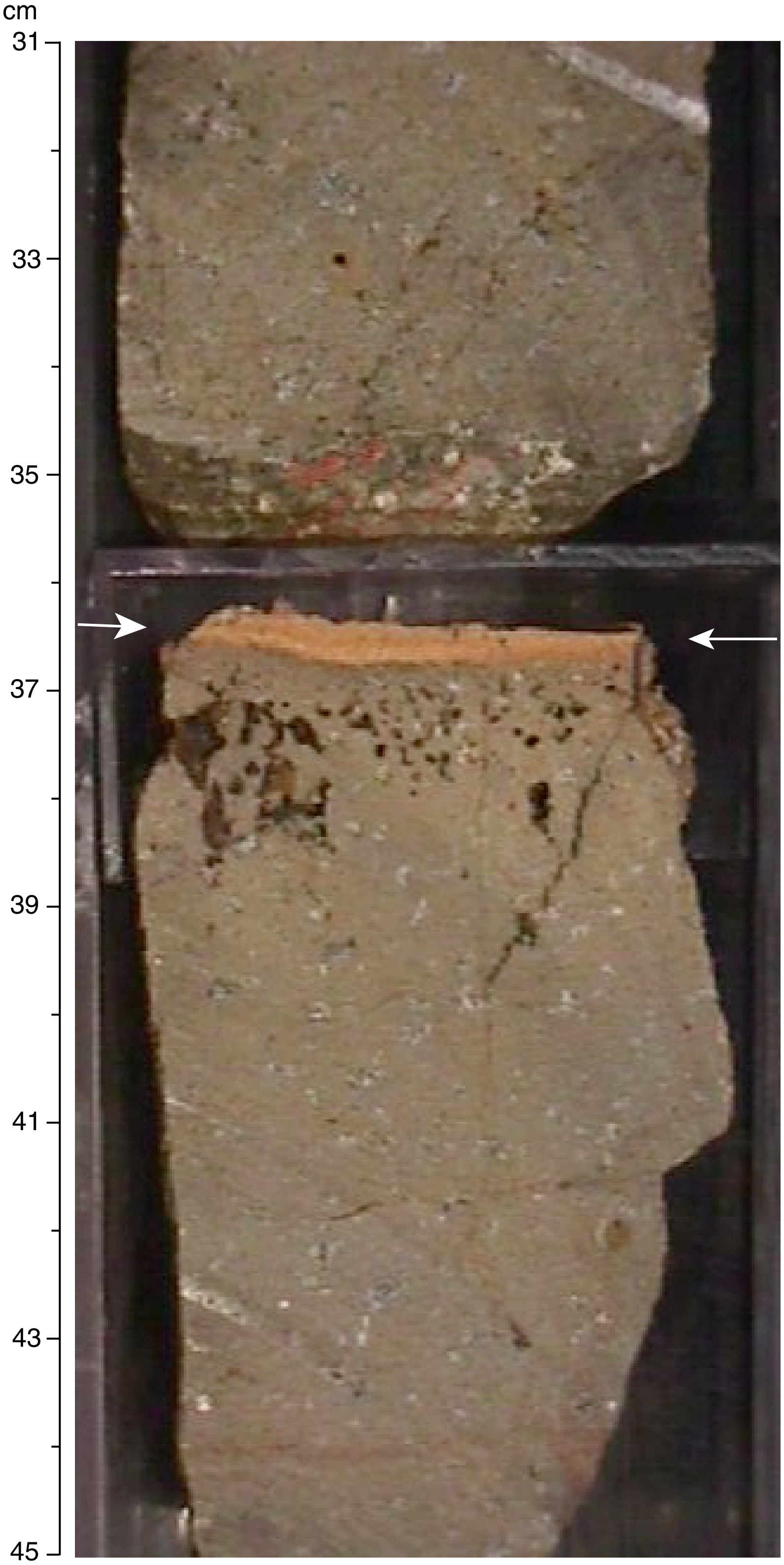

Figure F11. Vesicle distribution through a segment of basement Unit 5.

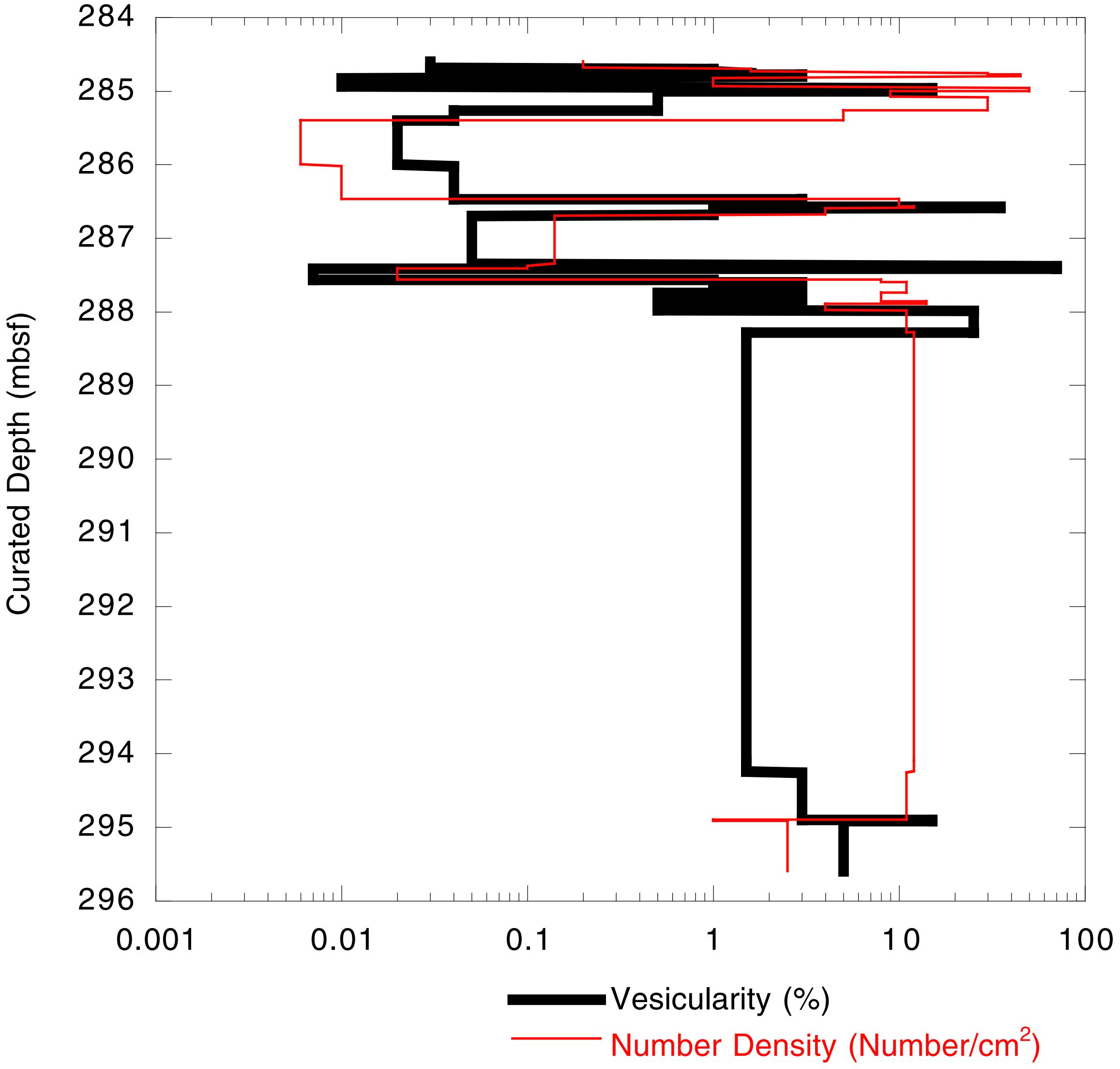

Figure F12. Vesicle distribution through a segment of basement Unit 6.

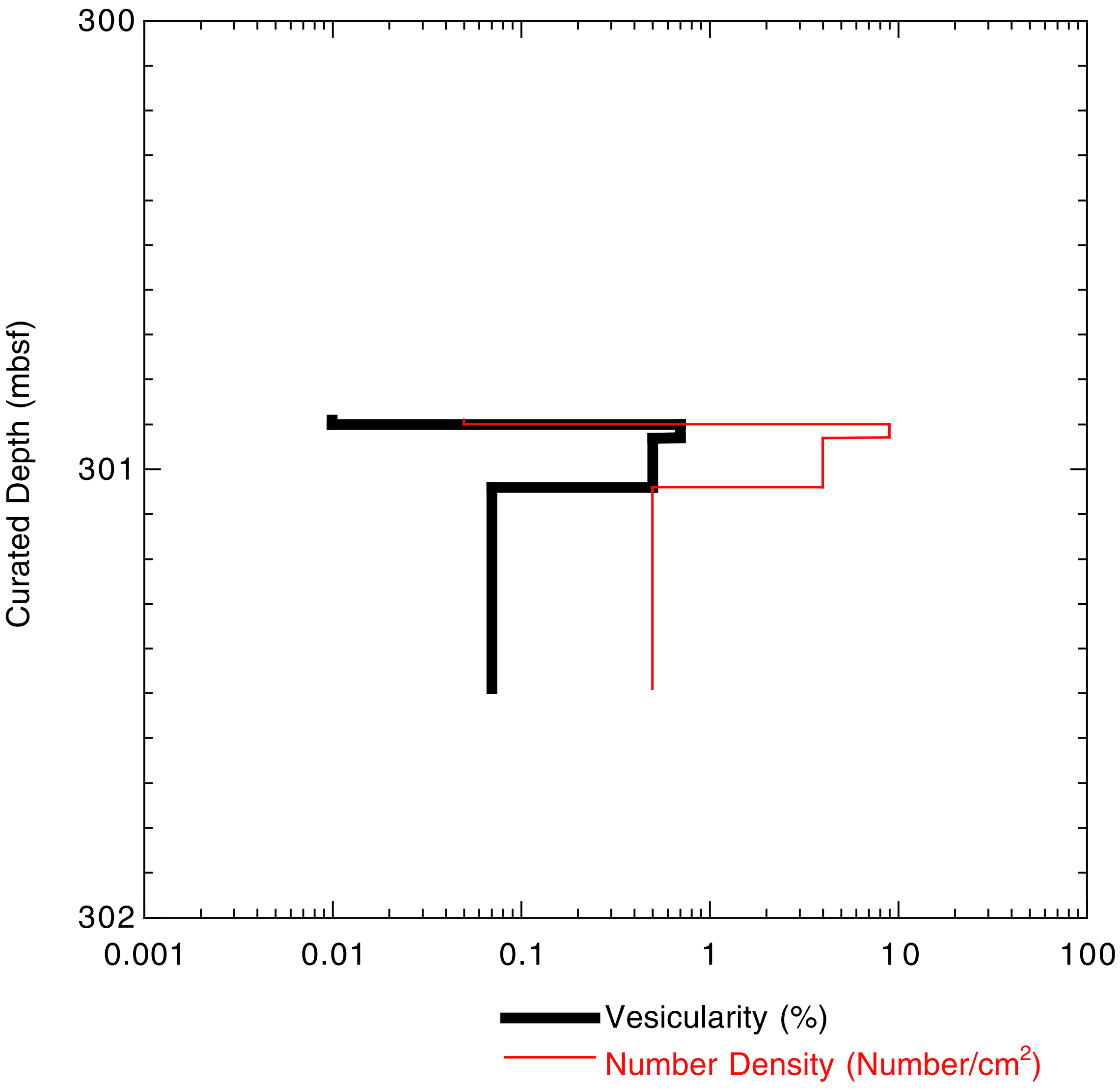

Figure F13. Close-up photograph of interval 183-1140A-35R-2, 37–47 cm, showing a fractured chilled margin in basement Unit 6 with pieces of the chilled margin that have been pushed 2–3 cm back into the pillow lobe with metamorphosed sediments filling the resulting space.

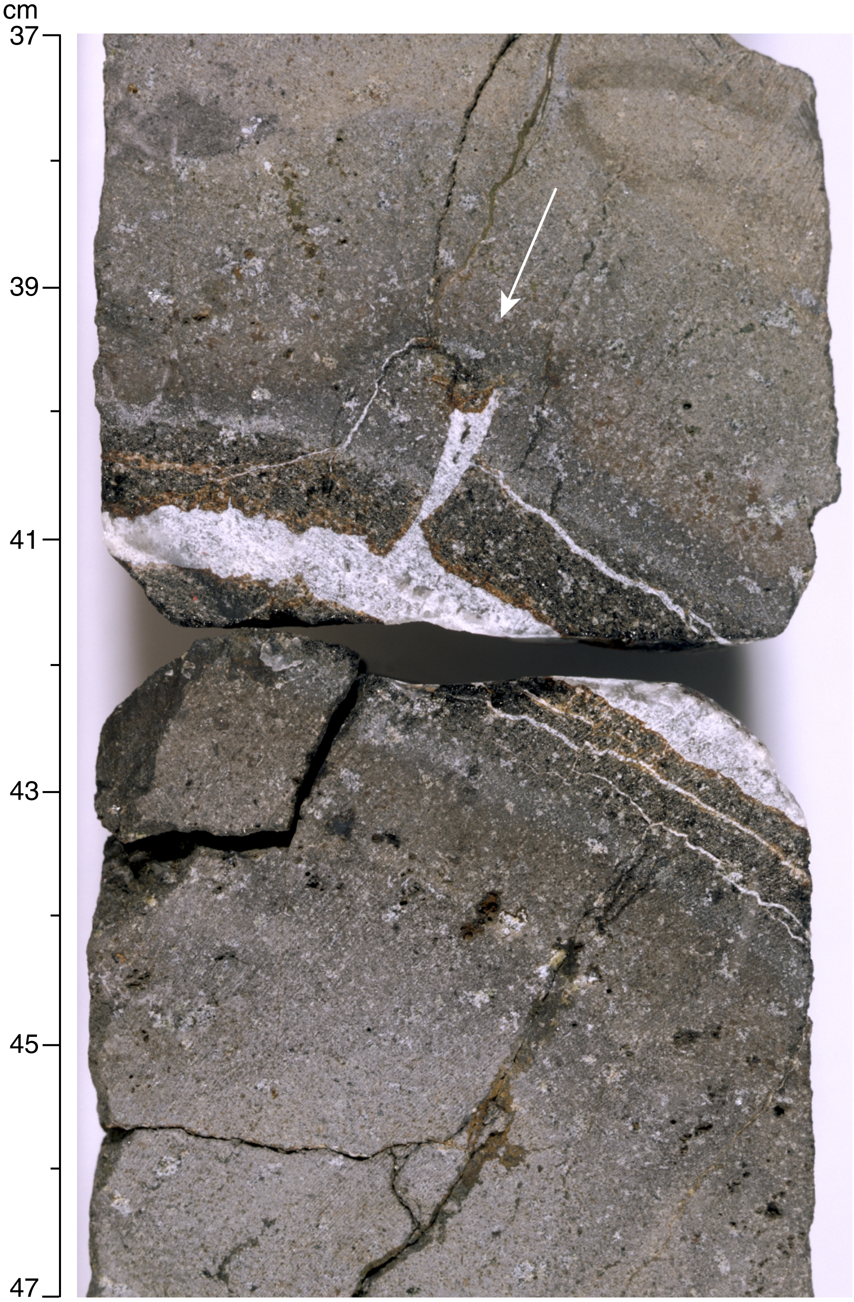

Figure F14. Graph of average lobe size in recovered rocks from Hole 1140A.

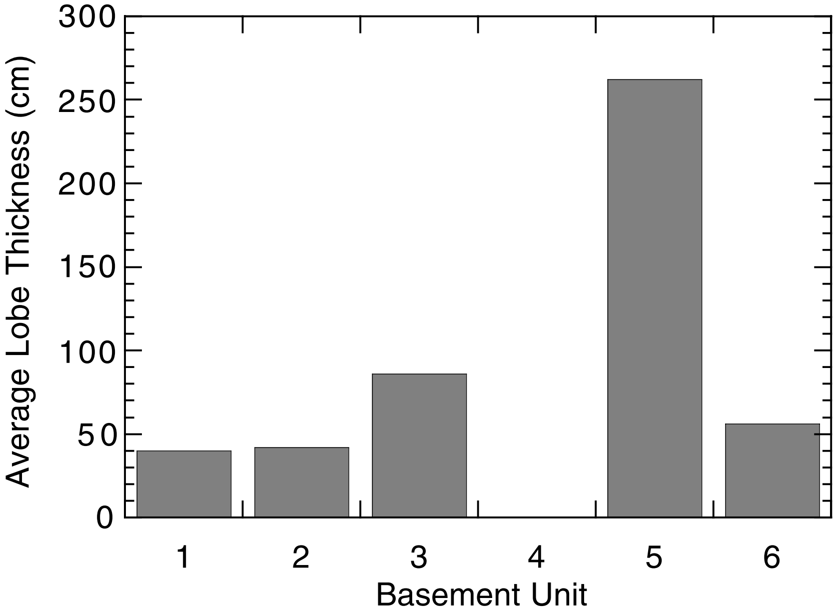

Figure F15. Interpretative summary of the lithology, morphology, and mineralogy of basement units sampled in the basement units at Site 1140. Boundaries for igneous Units 1–6 are indicated. Note that the contact between Units 1 and 2 was not recovered and has been located using downhole logging data (see "Physical Volcanology," p. 12, and "Downhole Measurements," p. 29). The occurrence of plagioclase, olivine, and clinopyroxene phenocrysts is indicated as well as the presence of glassy margins. A reversal of the magnetic field occurred between the time of eruption of Units 1 and 2 (see "Paleomagnetism," p. 22). The density log (see "Downhole Measurements," p. 29) and its interpretation are shown schematically to provide information about the lithology of unrecovered Cores 183-1140A-29R and 30R.

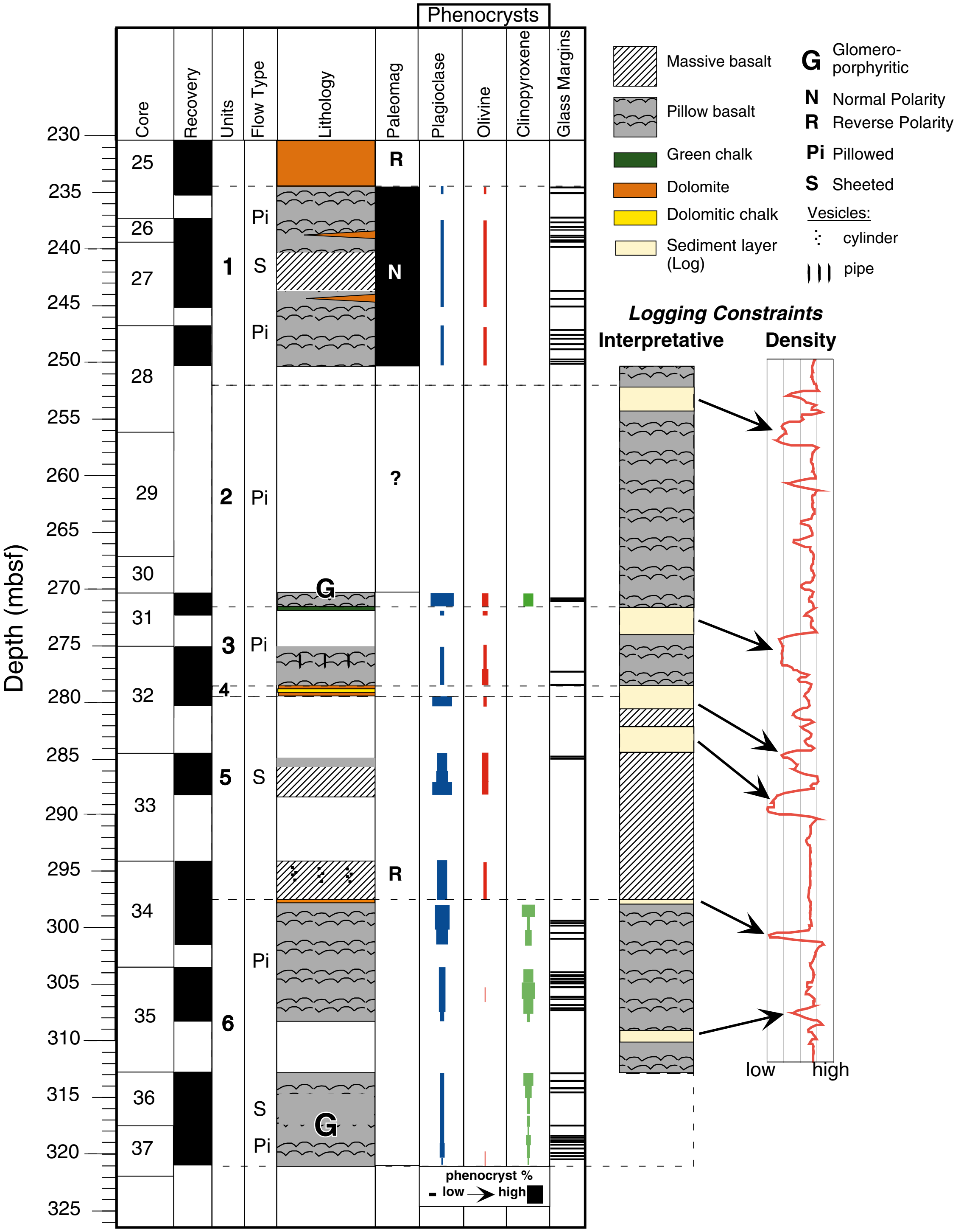

Figure F16. Photomicrograph (in plane-polarized light) of glass containing fresh, euhedral olivine phenocrysts (characteristic six-sided shape; center) from a chilled pillow margin (Unit 1). The largest olivine contains inclusions of two small chromite crystals and glass (left of the crystal) in Sample 183-1140-26R-1 (Piece 1A, 5–8 cm). The chromite inclusions in the olivine indicate early oxide precipitation.

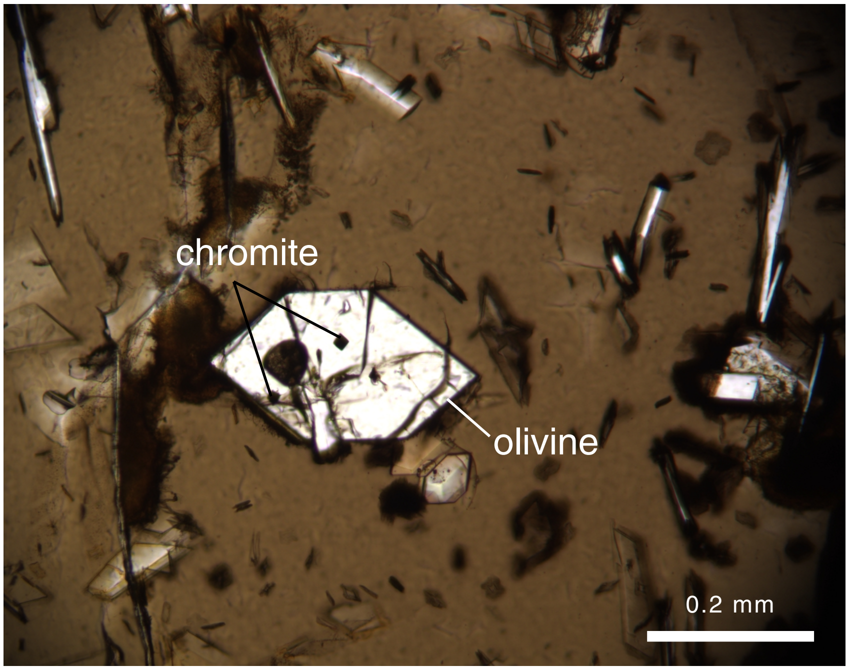

Figure F17. Photomicrographs (in cross-polarized light) of plagioclase phenocrysts from a plagioclase-clinopyroxene-olivine-phyric pillow basalt (Unit 2) in Samples 183-1140-31R-1 (Piece 3B, 53–57 cm) and 183-1140-31R-2 (Piece 4, 16–20 cm). The plagioclase phenocrysts in (**A**) and (**B**) show a marked compositional zoning pattern from core to rim. The plagioclase core in (A) contains several melt inclusions.

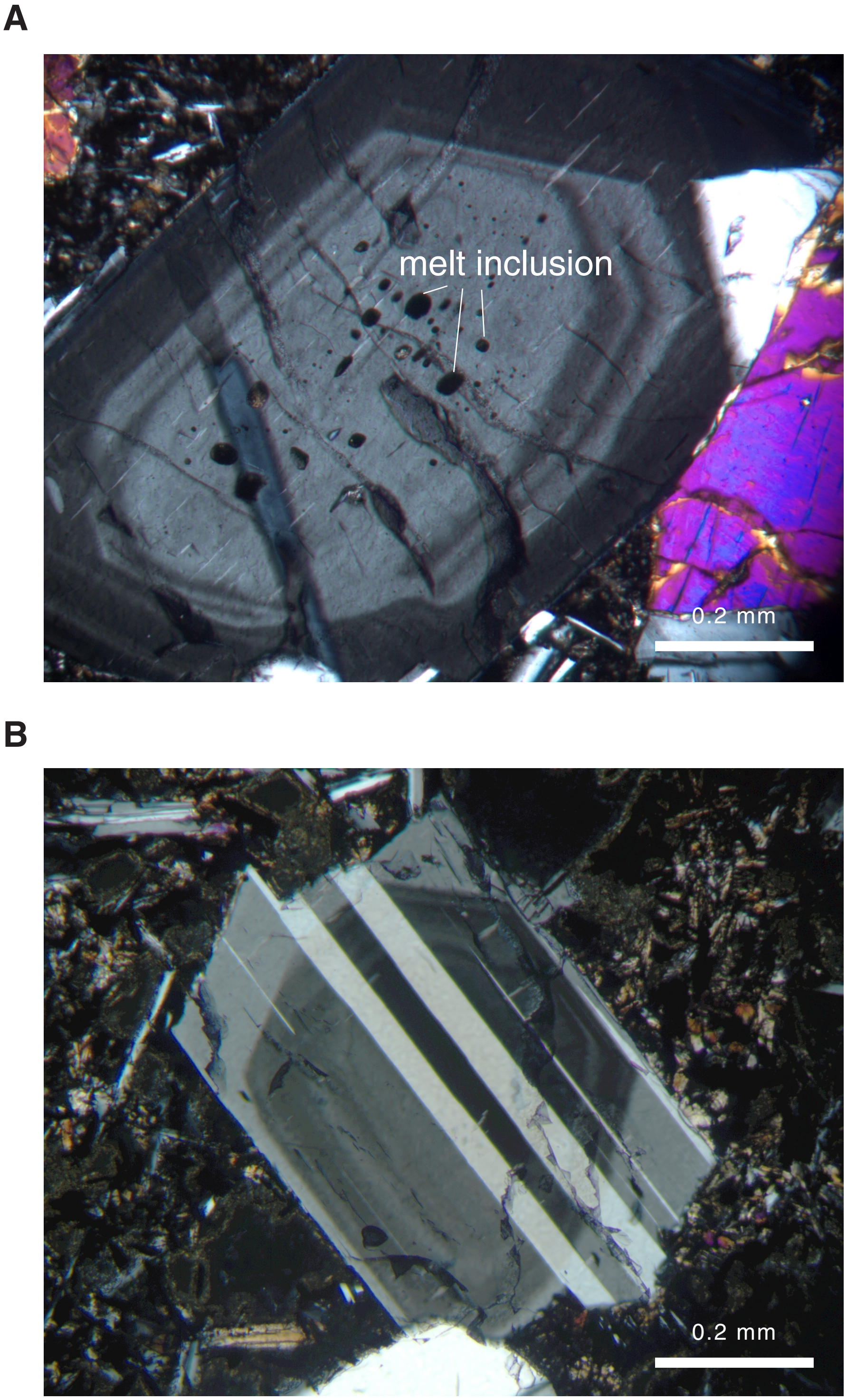

Figure F18. A. Photomicrograph (in cross-polarized light) of two large clinopyroxene phenocrysts from a plagioclase-clinopyroxene-olivine-phyric pillow basalt (Unit 2) in Sample 183-1140-27R-2 (Piece 1A, 0–5 cm). These phenocrysts show a compositional zonation defining core and mantle areas. **B.** Photomicrograph (in cross-polarized light) of a glomerocryst of clinopyroxene from a plagioclase-clinopyroxene-olivine-phyric pillow basalt in Unit 2, in Sample 183-1140-27R-2 (Piece 1A, 0–5 cm). Zoning is a relatively common feature of augites and particularly of Ti-rich varieties (sector zoning or hourglass). The lack of any pleochroism in this clinopyroxene indicates that although titanium levels are high enough (see Table T7, p. 110) to promote sector zonation, they are not as high as in alkali basalts where titaniferous augites are usually pleochroic.

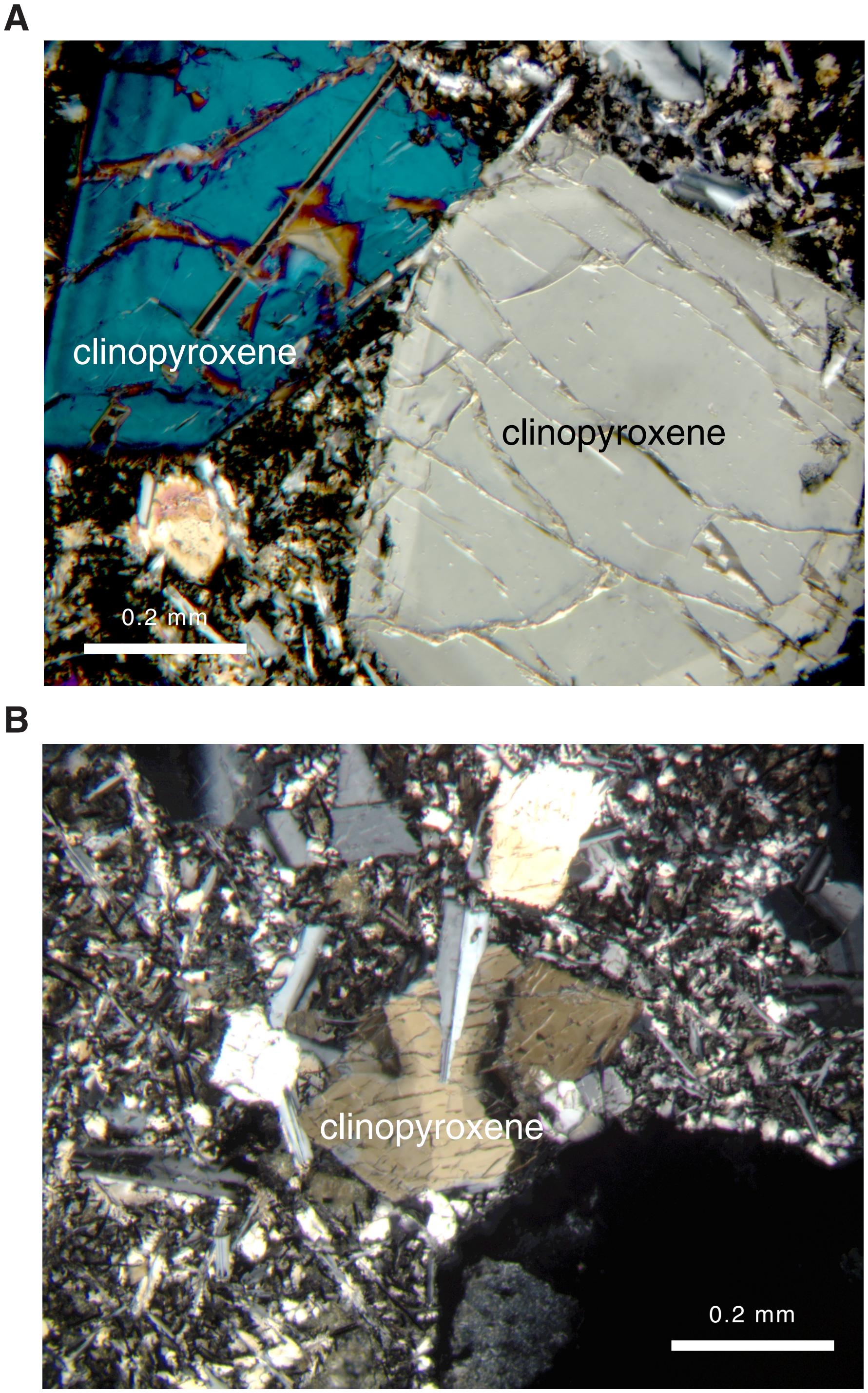

Figure F19. Photomicrograph (in cross-polarized light) of a partially altered olivine phenocryst (Unit 1) in Sample 183-1140-27R-2 (Piece 1A, 0–5 cm). The core remains fresh and is surrounded by brown clay.

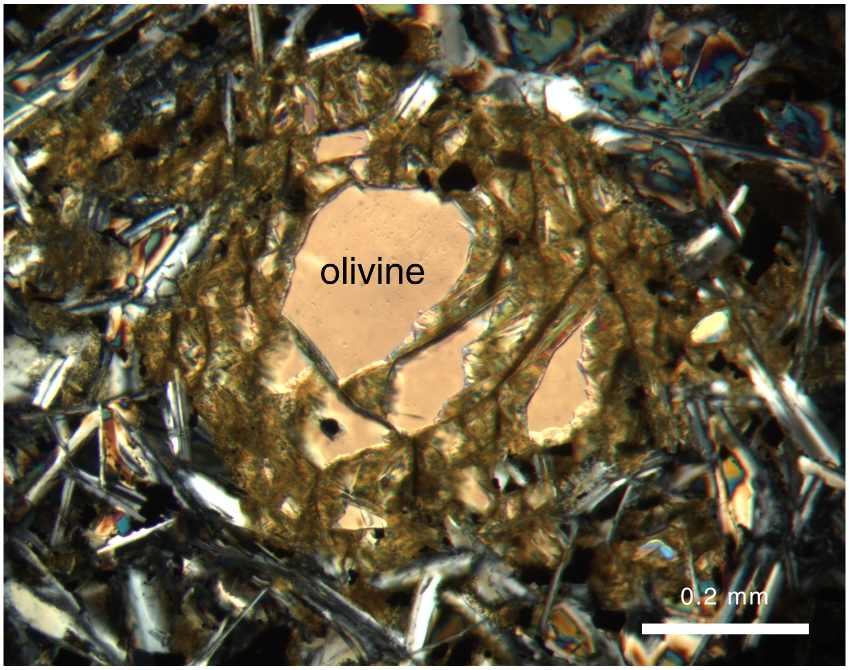

Figure F20. A. Photomicrograph (in plane-polarized light) of the boundary between a glassy pillow margin (center right) and dolomitic sediment (extreme lower right) (Unit 1) in Sample 183-1140-26R-1 (Piece 2A, 84–86 cm). The inner part of the pillow's glassy margin (upper left) is fresh and contains olivine phenocrysts and plagioclase microlites, whereas the outermost glassy margin (center right) is aphyric and locally altered to brown clay. A set of carbonate veins (white) crosscuts or fills in open spaces in the pillow margin. **B.** Photomicrograph (in plane-polarized light) of the boundary between foraminifer-bearing dolomite (central area) and the glassy margin of a basaltic pillow lava (upper left) (Unit 1) in Sample 183-1140-26R-1 (Piece 2A, 84–86 cm). The outermost glassy margin is locally altered to brown clay; carbonate veins (white) run parallel to the boundary in this area.

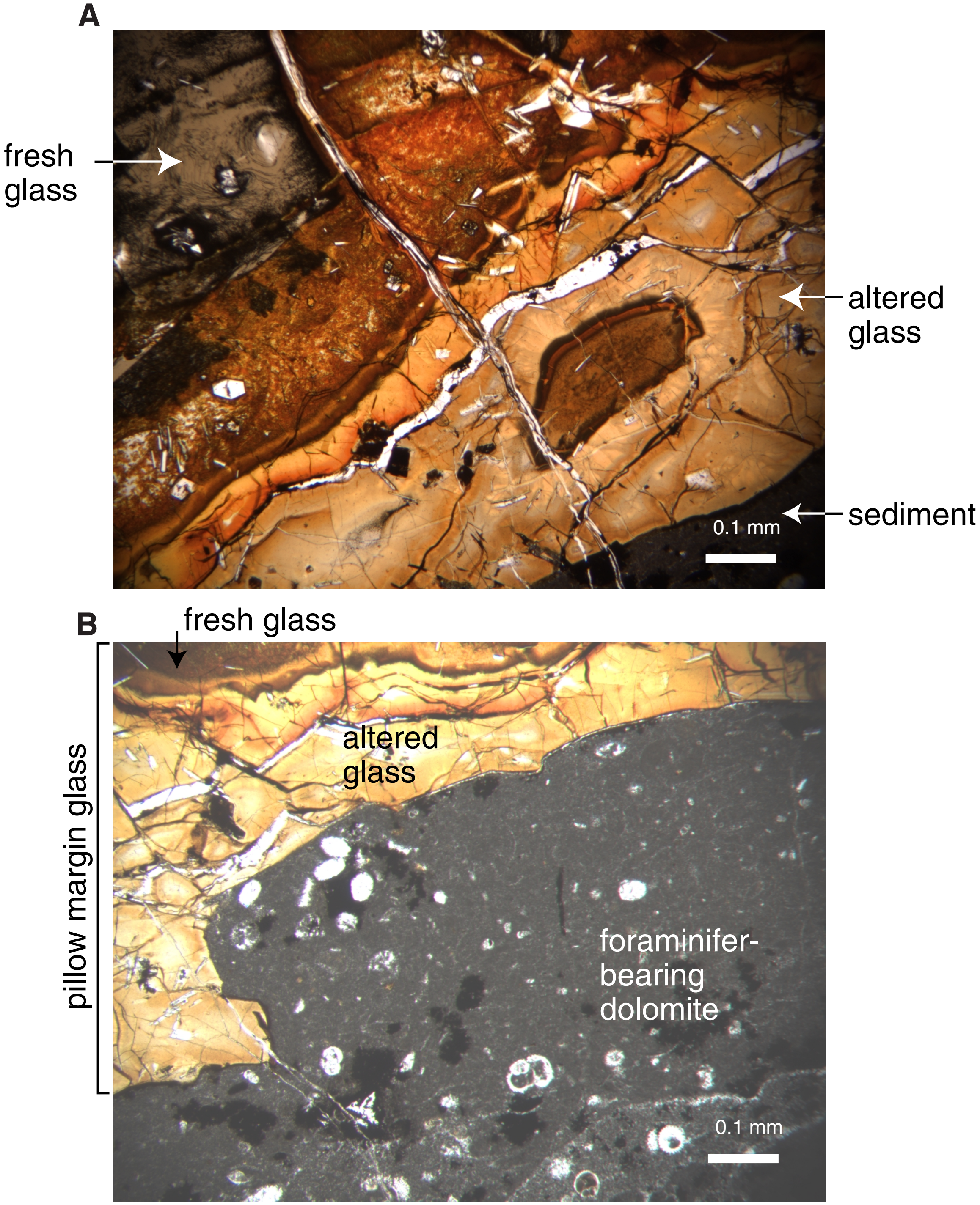

Figure F21. Photomicrograph (in plane-polarized light) of a glassy margin of a pillow lava from Unit 1, with radiating clusters of plagioclase microlites in Sample 183-1140-26R-1 (Piece 1A, 5–8 cm). These microlites display swallow-tailed terminations attesting to rapid cooling.

Figure F22. Photomicrograph (in plane-polarized light) of glass from a chilled pillow margin (Unit 1) in Sample 183-1140-26R-1 (Piece 1A, 5–8 cm). The glass contains fresh euhedral olivine phenocrysts (upper center), some of which contain spherical melt inclusions. The hair-like texture shown on the right consists of narrow channels that are the result of microbial degradation of the glass (Fisk et al., 1998).

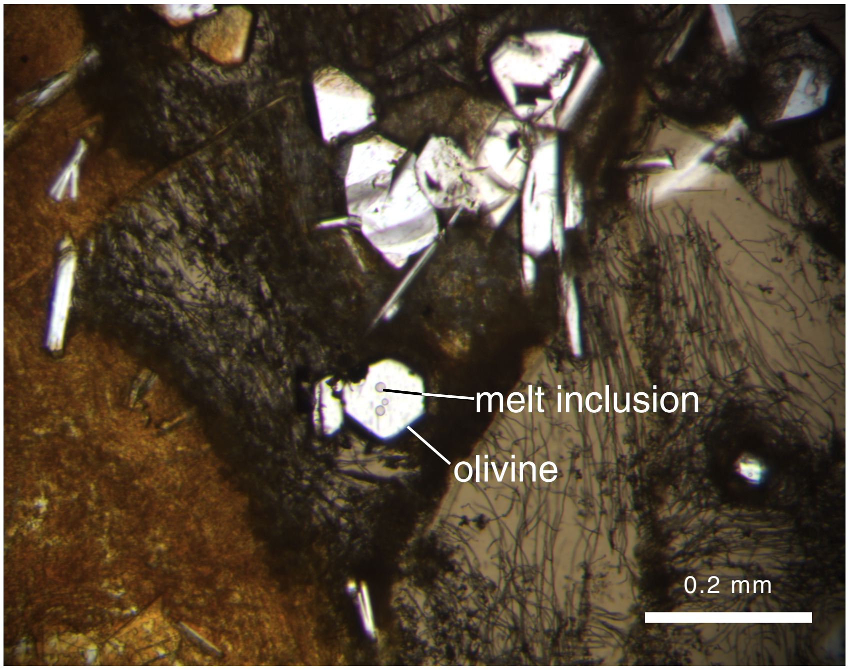

Figure F23. Close-up photograph of brecciated glass at a pillow margin in Unit 1, with clasts suspended in a calcite cement. **A.** Interval 183-1140A-27R-5, 53–66 cm. **B.** Interval 183-1140A-27R-5, 54–80 cm (full core).

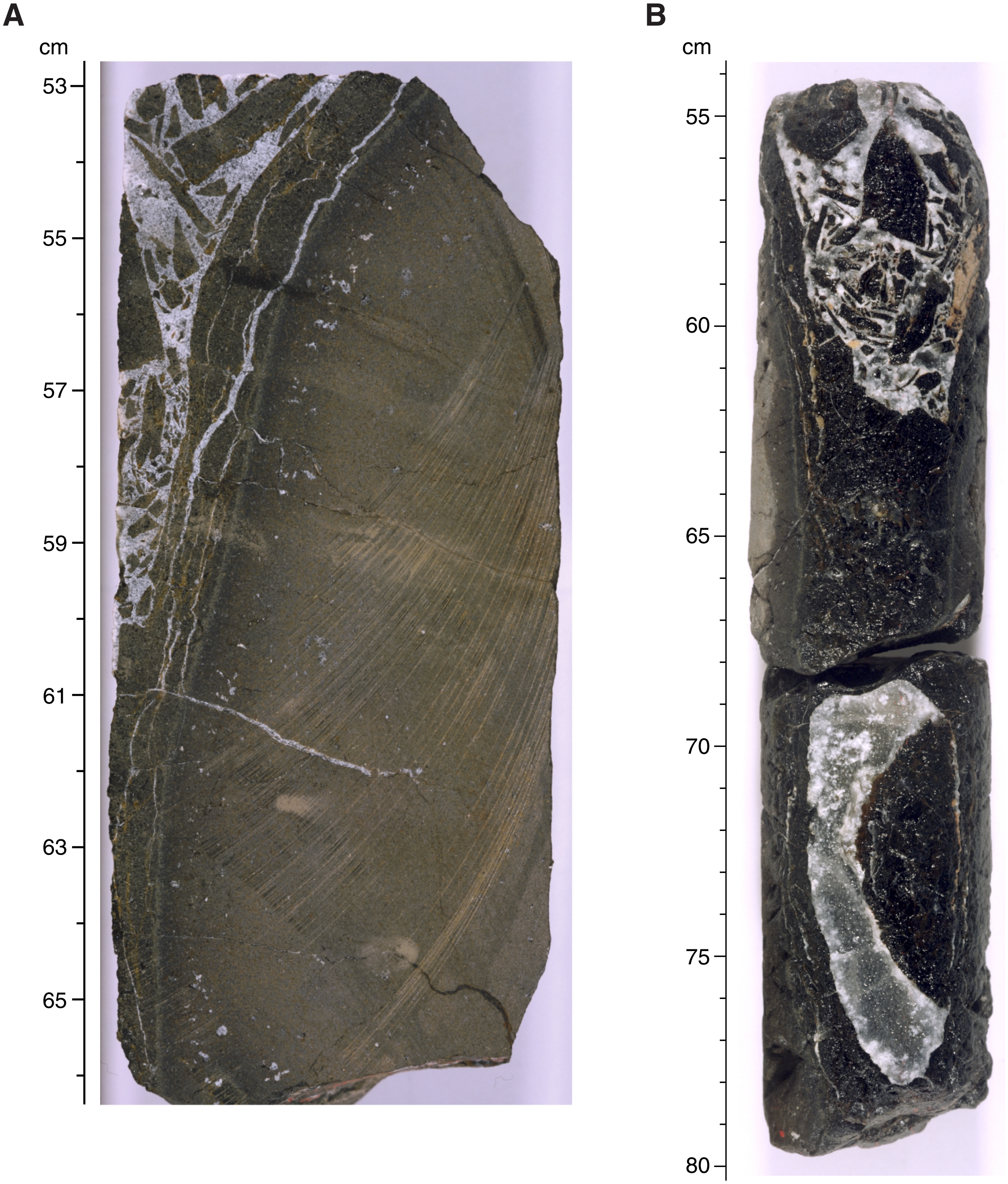

Figure F24. Photomicrographs of two examples of subophitic texture in the interiors of the larger and more slowly cooled pillow basalts (Unit 1) in Sample 183-1140-27R-2 (Piece 1A, 0–5 cm) in (**A**) plane-polarized light and (**B**) in cross-polarized light.

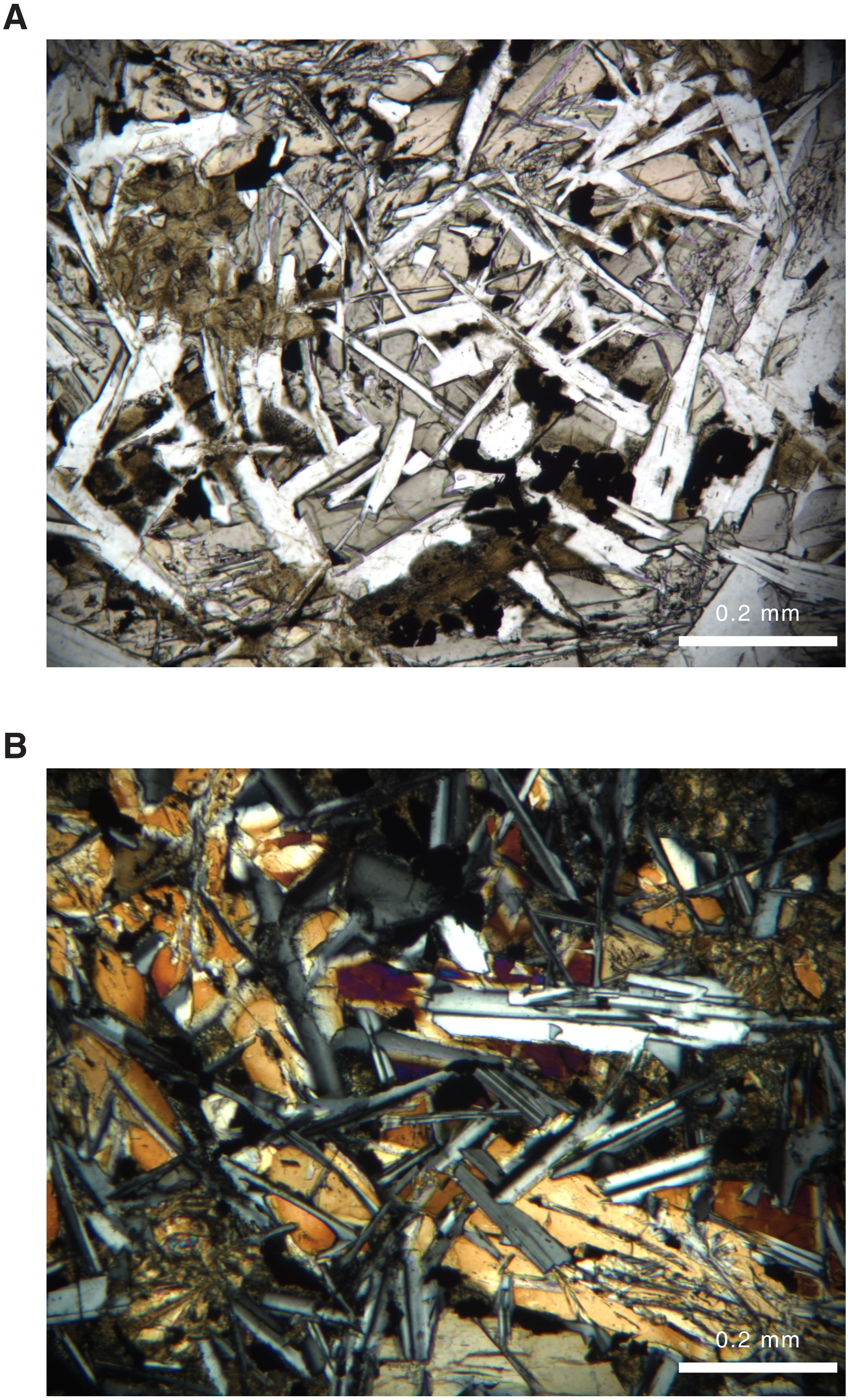

Figure F25. Photomicrograph (in cross-polarized light) of a partially altered groundmass olivine from the interior of a pillow basalt (Unit 1) in Sample 183-1140-27R-2 (Piece 1A, 0–5 cm).

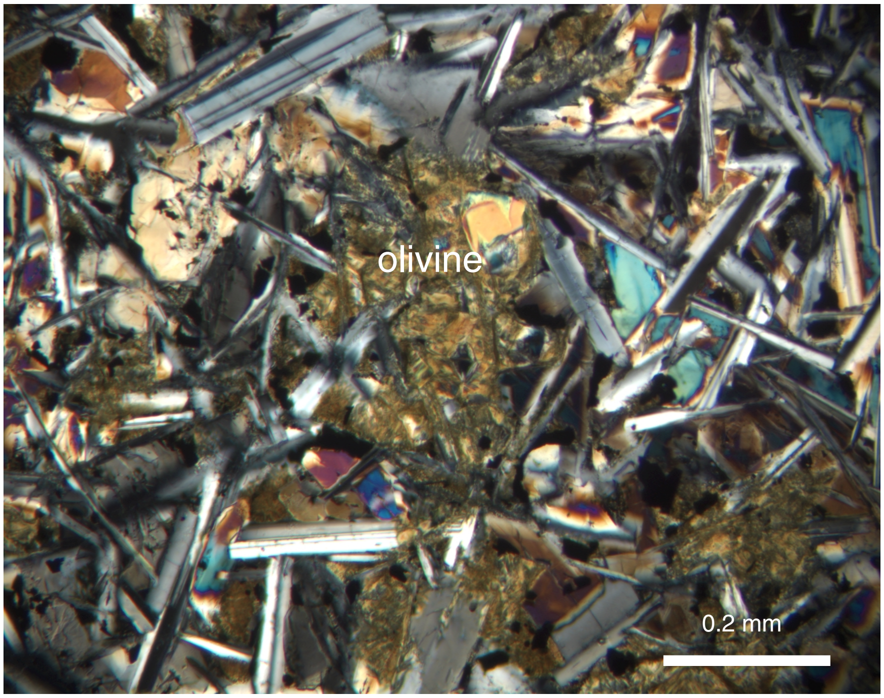

Figure F26. **A.** Photomicrograph (in reflected light) of a skeletal titanomagnetite from the inner part of a pillow lava (Unit 6) in Sample 183-1140-37R-1 (Piece 1C, 46–49 cm). This texture reflects a rapid crystallization of the lava (see Fig. F19, p. 55). Sulfide (pyrite or pentlandite) is present around and as minute inclusions (small bright grains) in the titanomagnetite grain. **B.** Photomicrograph (in reflected light) of secondary pyrite between plagioclase laths (Unit 2) in Sample 183-1140-31R-1 (Piece 3B, 53–57 cm).

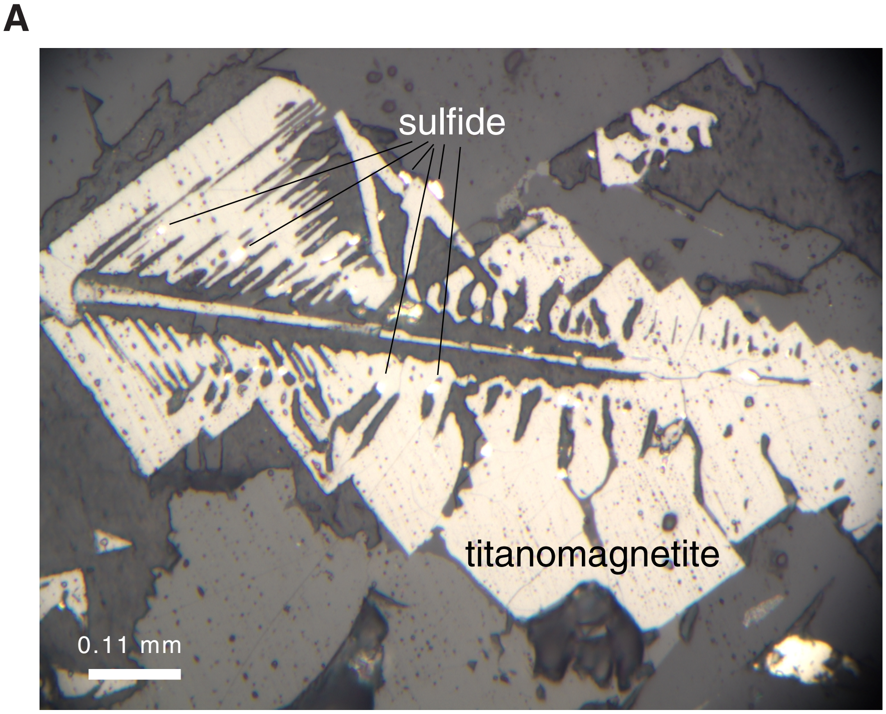

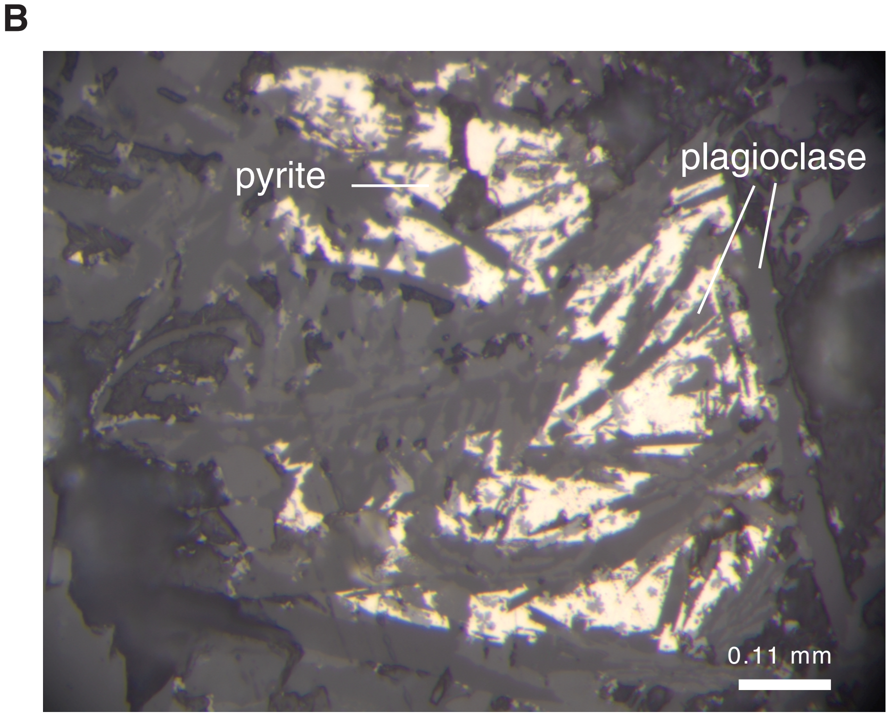

Figure F27. A. Site 1140 igneous rock compositions represented by total alkalis ($Na_2O + K_2O$) vs. SiO_2 (fields from Le Bas et al., 1986). All sampled lavas from Site 1140 are tholeiitic basalts. **B.** Alkalic and tholeiitic basalt fields are distinguished by the Macdonald-Katsura (1964) dashed line. Site 1140 basalts are poorer in alkalis than lavas from all other locations on the Kerguelen Plateau, except Site 750. The two samples that have slightly higher alkali contents correspond to lavas from Units 2 and 3. Compositions of basalts from southern and central Kerguelen Plateau locations are shown as fields for Sites 738, 747, 749, and 750 (Alibert, 1991; Mehl et al., 1991; Salters et al., 1992; Storey et al., 1992) and dredge samples (Davies et al., 1989; Weis et al., 1989). Open circles and diamond indicate highly altered samples from Sites 1137 and 1138, respectively.

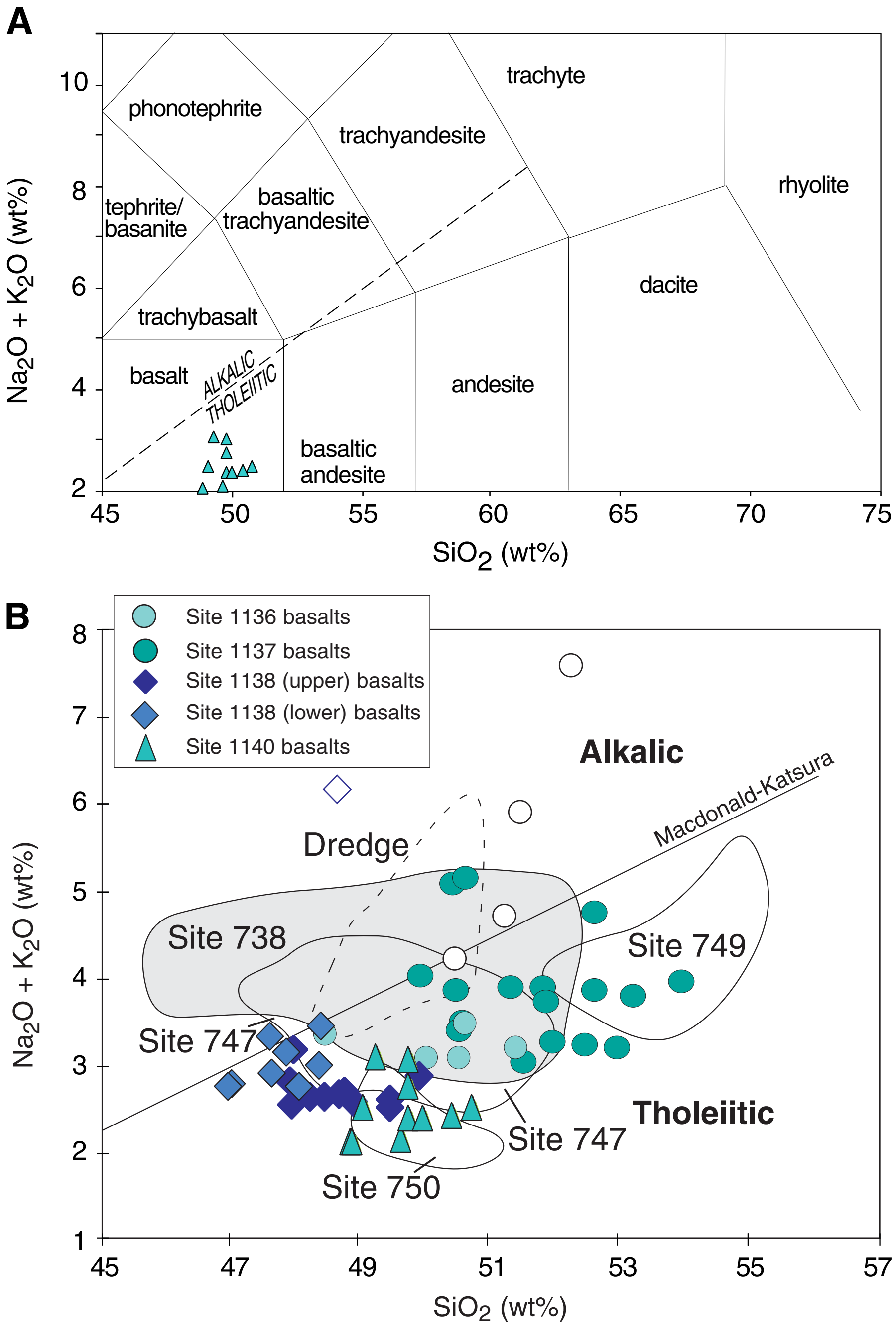

Figure F28. Major element abundances plotted vs. Mg# (Mg# is Mg/[Mg + Fe^{2+}], with Fe^{2+} = 0.8 Fe total) for Site 1140 basalts. Units 2 and 3 lavas are characterized by lower Mg#.

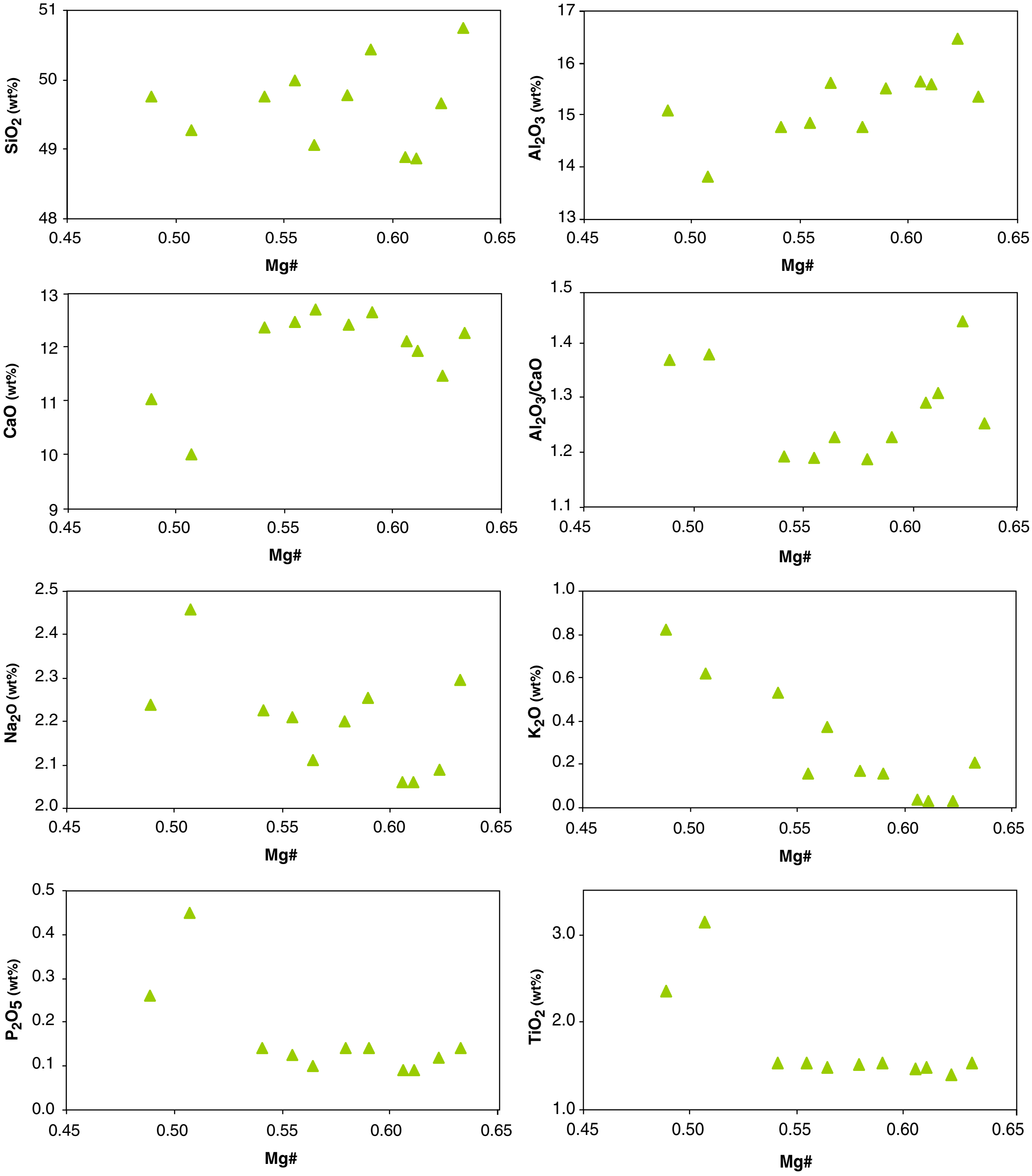

Figure F29. Downcore variations in major element composition for Site 1140 basalts. Lavas from Units 2 and 3 stand out because of lower Mg# and CaO but higher TiO_2, P_2O_5, and K_2O, and contents.

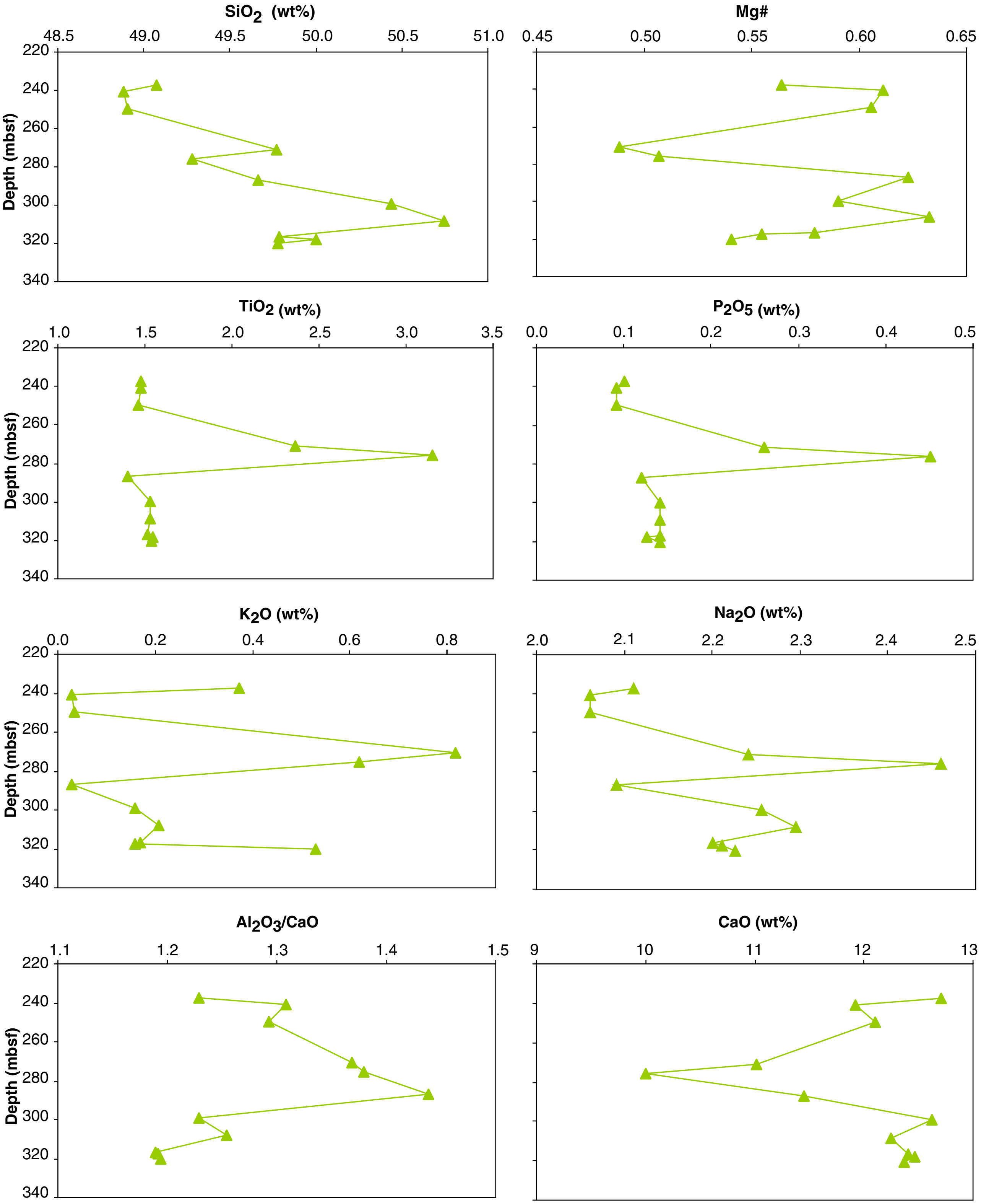

Figure F30. Downcore variations in trace element abundances and primitive mantle–normalized ratios (indicated by a subscript N) for Site 1140 basalts. Lavas from Units 2 and 3 are distinctly more enriched in Zr and Nb, have lower Cr concentrations, and have higher $(Zr/Ti)_N$, $(Nb/Zr)_N$, and $(Zr/Y)_N$ ratios.

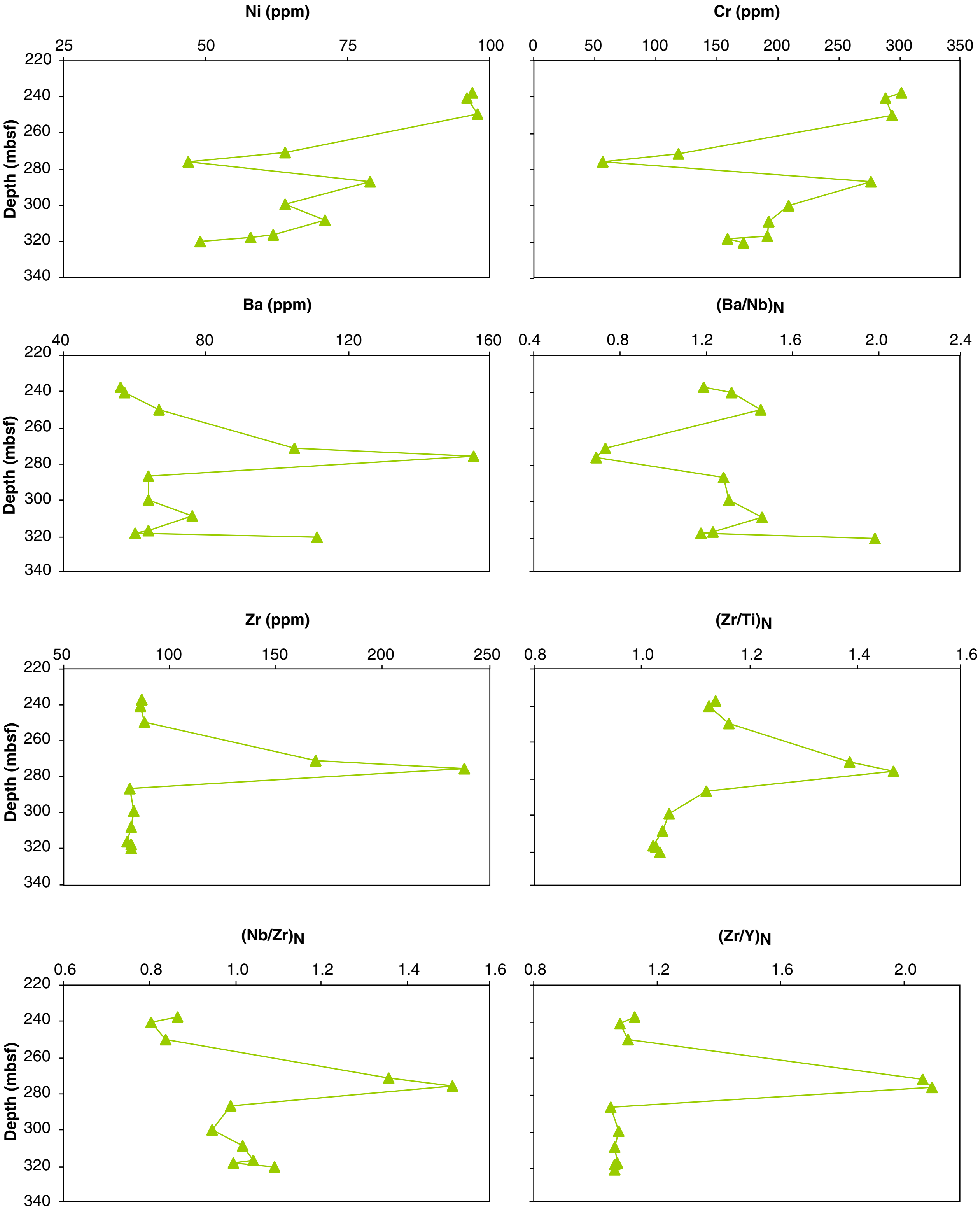

Figure F31. **A.** Primitive mantle–normalized (Sun and McDonough, 1989), incompatible trace element diagrams for Site 1140 basalts. **B.** Range for basalt compositions from Kerguelen Plateau Sites 749 and 750. Units 1, 5, and 6 from Site 1140 have concentrations intermediate between those for Sites 749 and 750 for the right part of the diagram (Nb-Y), but they are distinguished by low Rb and K. Except for Rb and K, lavas from Units 2 and 3 have much higher abundances of trace elements, by a factor of 5, than other Site 1140 basalts. Data sources are the same as in Figure F27, p. 63.

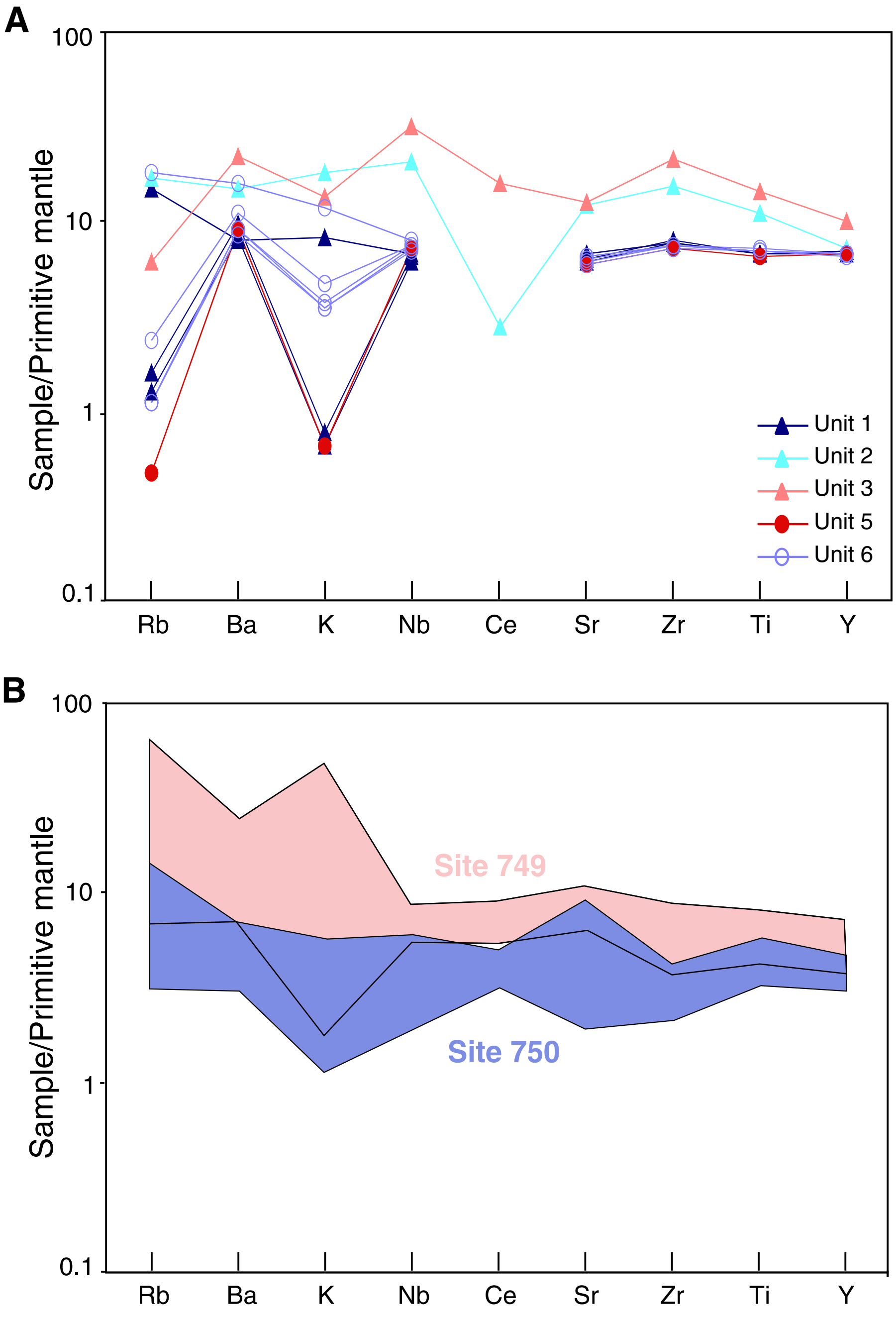

Figure F32. Primitive mantle–normalized Zr/Ti vs. Zr and Zr vs. Nb diagrams for Site 1140 basalts compared with data for central and southern Kerguelen Plateau basalts. Data sources are the same as in Figure F27, p. 63.

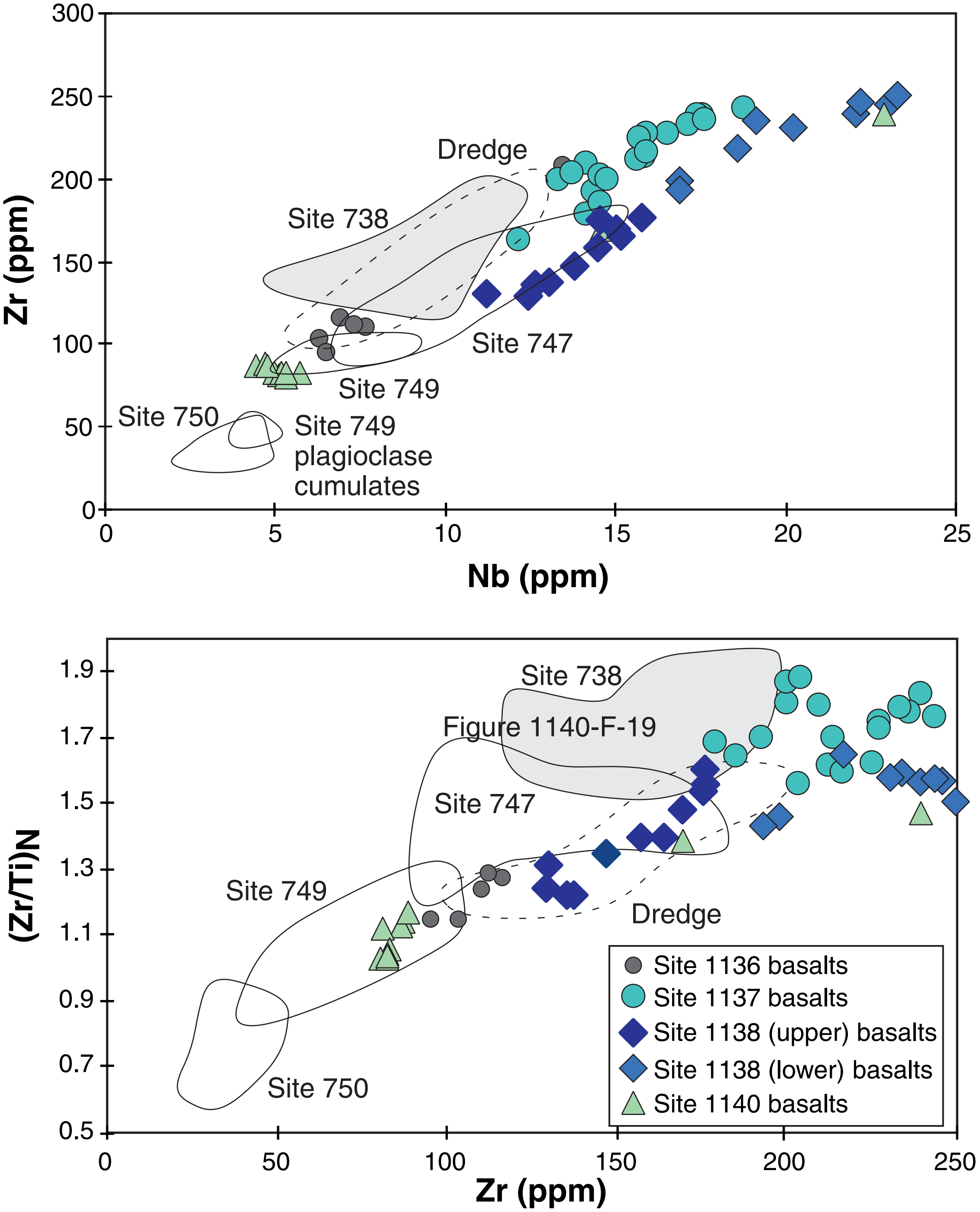

Figure F33. Nb/Y vs. Zr/Y diagram. This plot has been used to distinguish lavas derived from the Icelandic mantle plume from North Atlantic mid-ocean-ridge basalt (MORB) (Fitton et al., 1998). Shown for comparison are data for other Leg 183 sites and fields for basalts from Sites 738, 747, 749 and 750. Primitive mantle (PM) composition is located by the cross, and average oceanic island basalt (OIB) and MORB compositions are indicated by a black dot (data from Sun and McDonough, 1989). Site 1140 basalts plot within the plume-derived field. Units 1, 5, and 6 define a field that overlaps with Site 749 basalts, whereas Units 2 and 3 have higher ratios, comparable to those of Sites 1138 and 747 basalts. Data sources are the same as in Figure F27, p. 63.

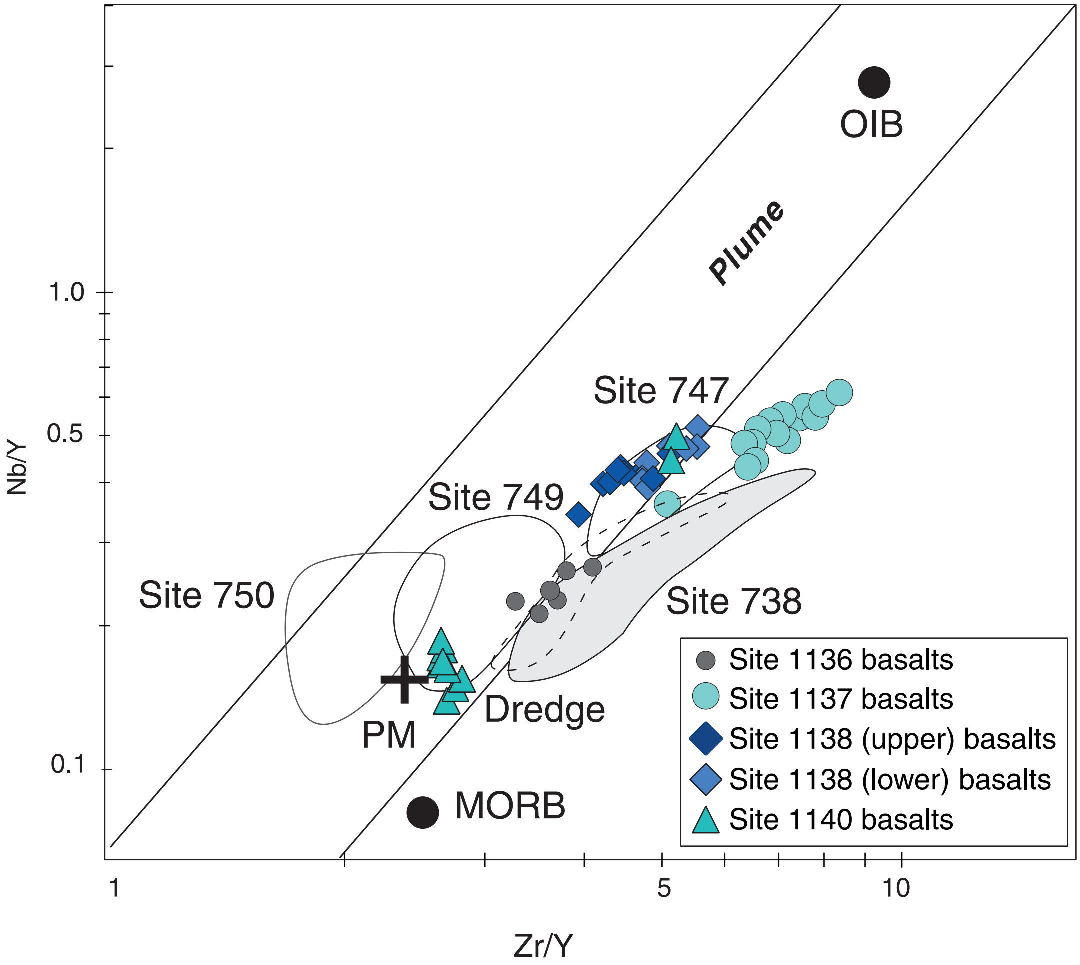

Figure F34. Alteration downhole in Hole 1140A vs. depth. Scalloped graphic in lava type column = pillow lavas; gray regions without this symbol = more massive lobes. Color shows the proportion of background gray basalts to brown oxidation halos. Black bars = the presence of glass, sediments, and secondary minerals. Sparry carbonate shows the location of intergrown open-space filled dolomite and calcite. Alteration: sl = slight, m = moderate, h = high, c = complete.

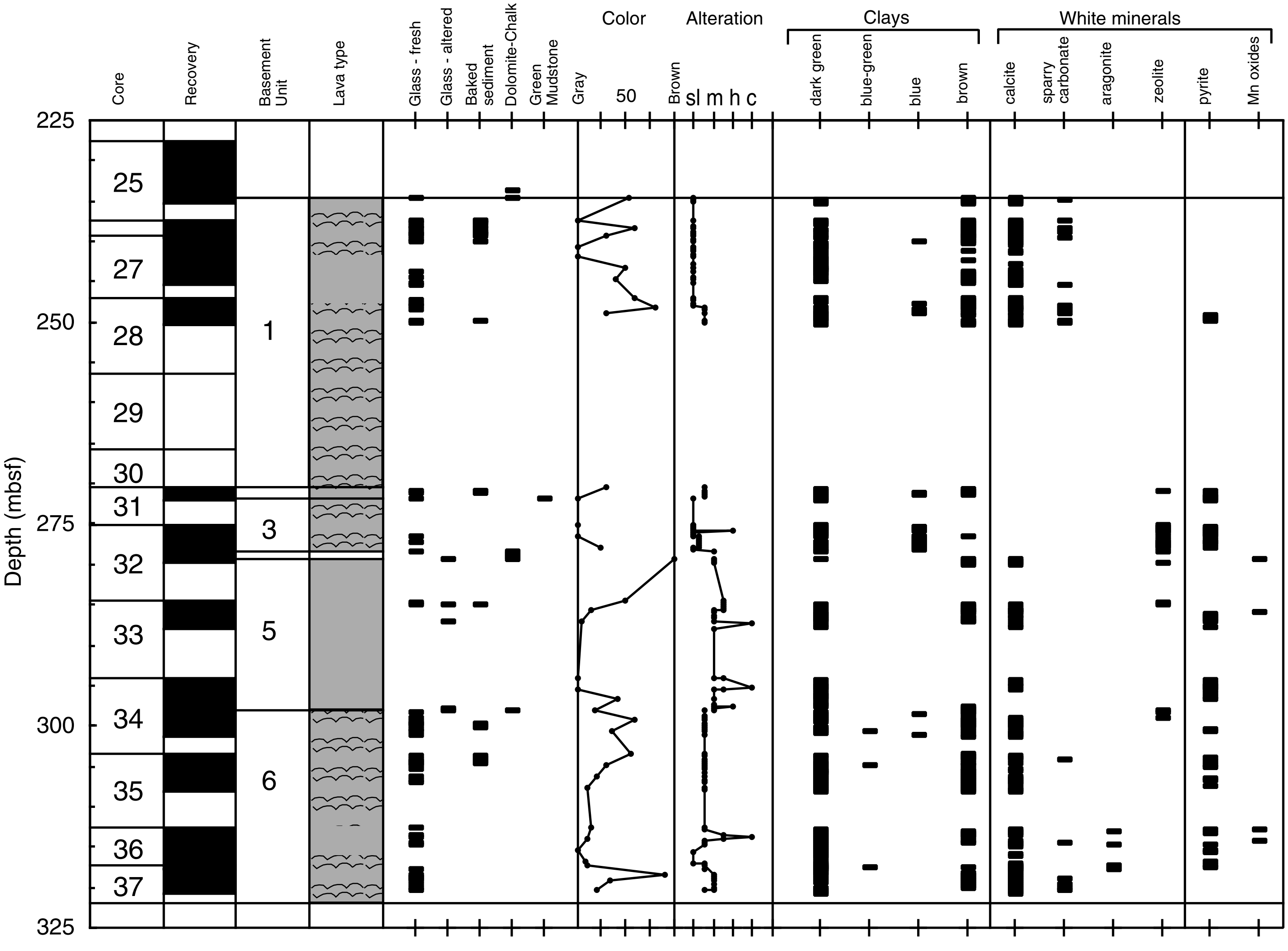

Figure F35. Close-up photograph of Sample 183-1140A-28R-3 (Piece 2, 86–102 cm). Glassy pillow rind with calcite-filling vesicles and veins. The rind cuts the core from ~98 cm on the left to 90 cm on the right. Open-space filled dolomite and baked white sediment is located along the margin with the glass.

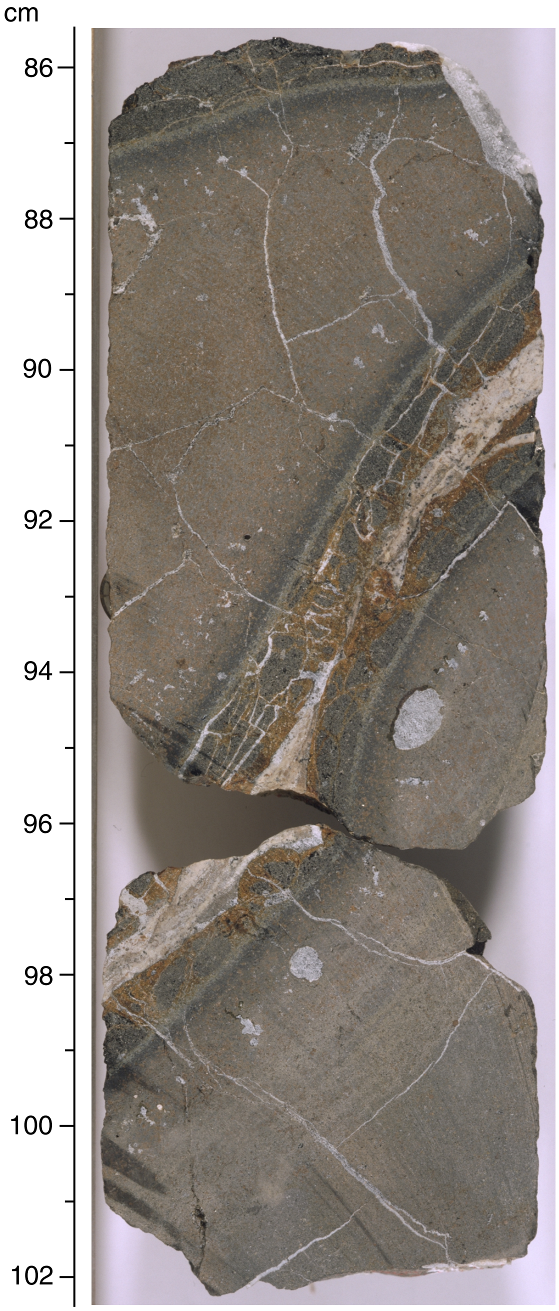

Figure F36. Close-up photograph of Sample 183-1140A-29R-1 (Piece 2, 83–96 cm). Baked foraminifer-bearing carbonate sediment on a 1-cm glassy margin in contact with sparry open-spaced filled dolomite. Brittle deformation of the glassy margin by the baked sediment has resulted in the injection of the sediment into the pillow interior while the basalt was still molten (at 92 cm). A mushroom-shaped cap of quenched vitreous glass is formed around the tip of the sediment indenter. A small vesicle trail runs parallel to the glassy margin near the contact between the variole-rich zone and the basalt.

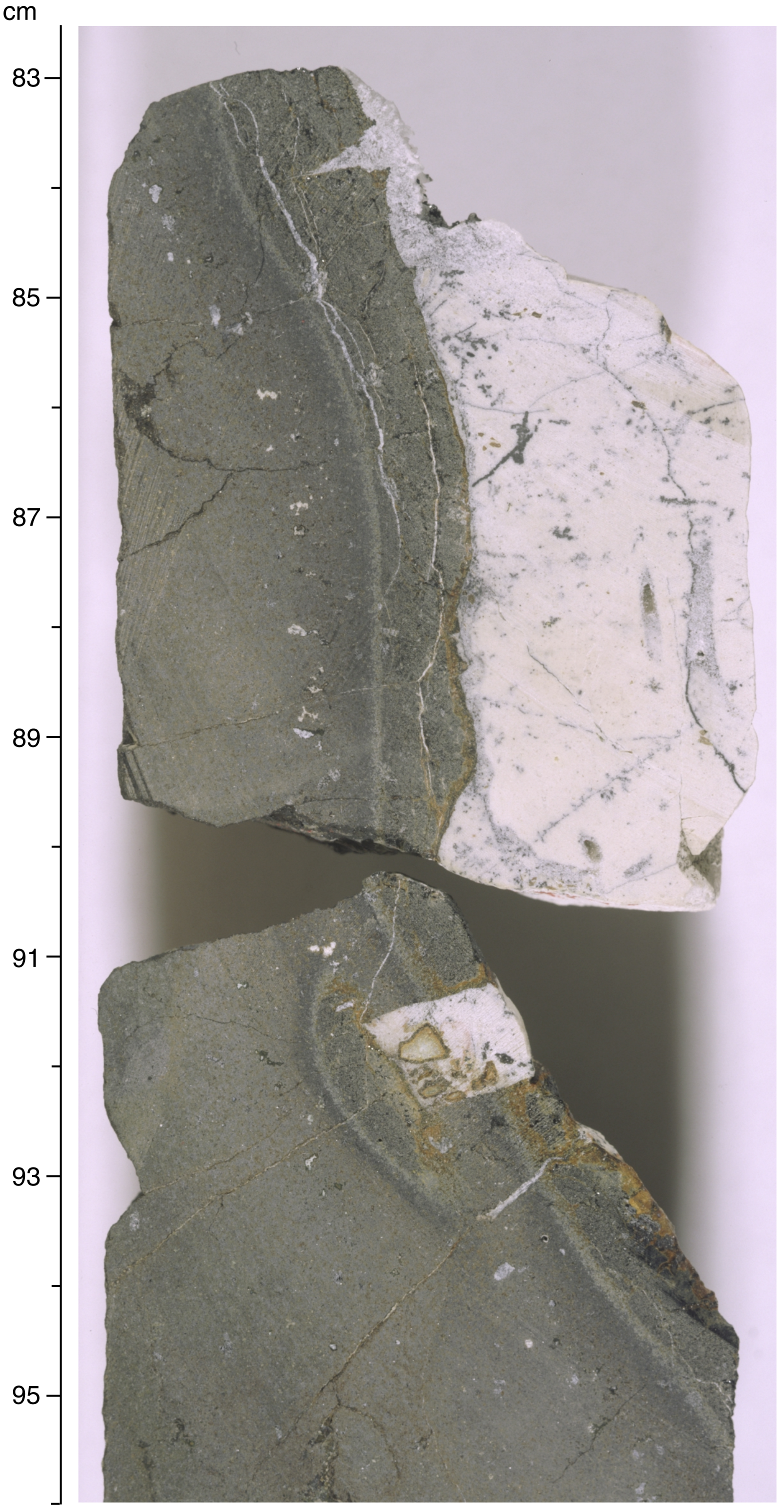

Figure F37. Close-up photograph of Sample 183-1140A-34R-3 (Piece 1, 77–90 cm). Sharp boundary between gray basalt and an oxidized orange-brown alteration halo related to the underlying contact with dolomitized chalk. The most intense coloration in this halo is at the boundary. The ~1-mm vein that cuts this boundary changes from light green clay to brown clay (± iron oxyhydroxides).

Figure F38. Close-up photograph of Sample 183-1140A-36R-1 (Piece 3, 112–124 cm). Highly altered, highly vesicular late-stage magmatic segregation in fine-grained basalt. The glass-rich mesostasis is completely altered to black clays, and the vesicles are filled with green clay and calcite.

Figure F39. Example of progressive AF demagnetization of a discrete sediment sample. The intensity decay curve is plotted on the left and the directional change is plotted on an orthogonal vector projection on the right. Magnetic directions that tend toward the origin with high median destructive fields are considered reliable. J_0 is the magnetization intensity before AF treatment.

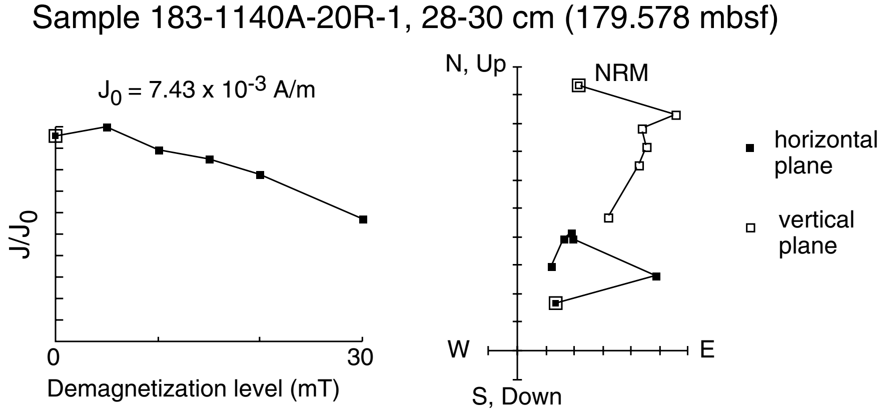

Figure F40. Hole 1140A inclination, intensity of remanent magnetization, and MST susceptibility of sediments from (**A**) 0–120 mbsf and (**B**) 120–240 mbsf. Crosses and lines represent remanent magnetization before and after AF demagnetization at 20 mT, respectively. Inclination data used for polarity interpretations are shown by open circles. Interpreted normal and reversed geomagnetic chrons are shown by black and white rectangles, respectively. Inclinations from discrete samples are shown by solid circles. Lithologic units are shown on the right. (Continued on next page.)

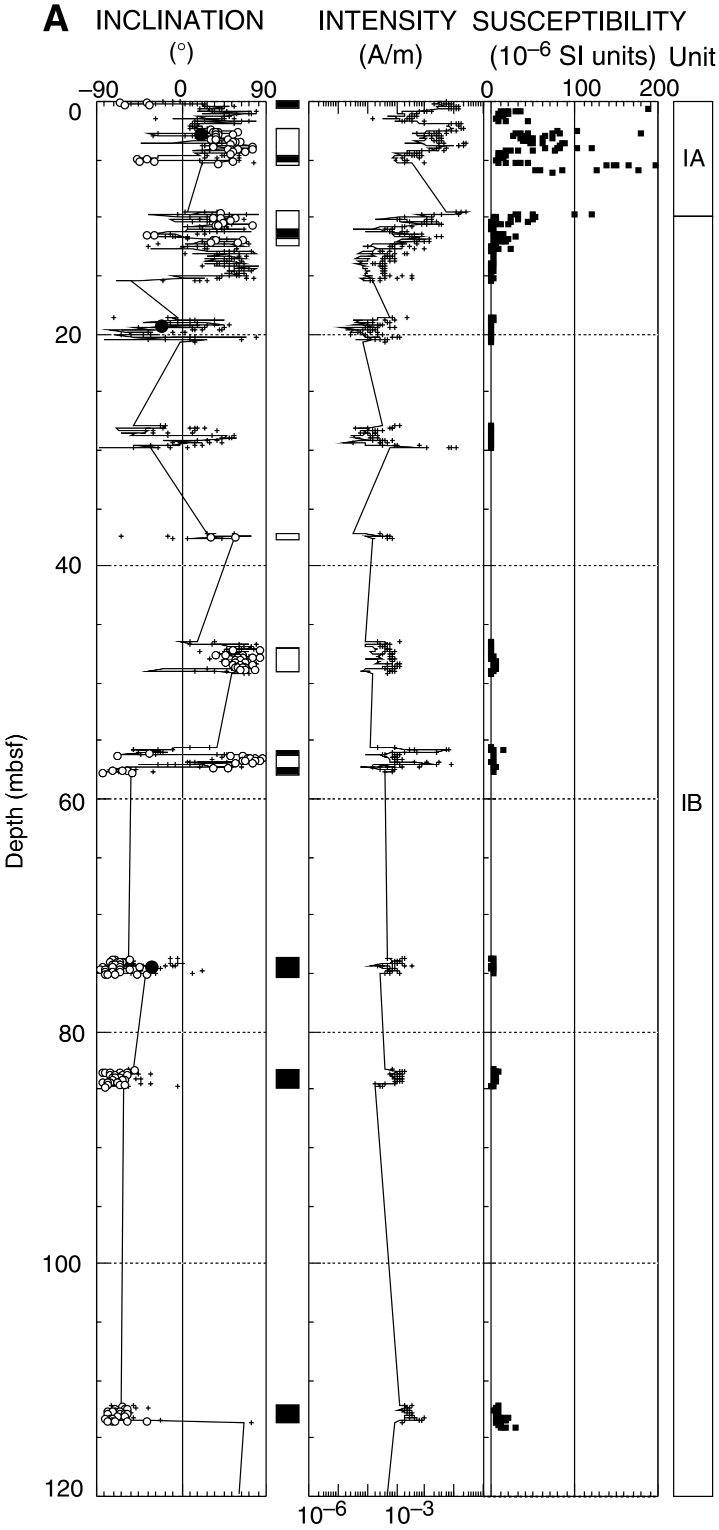

Figure F40 (continued).

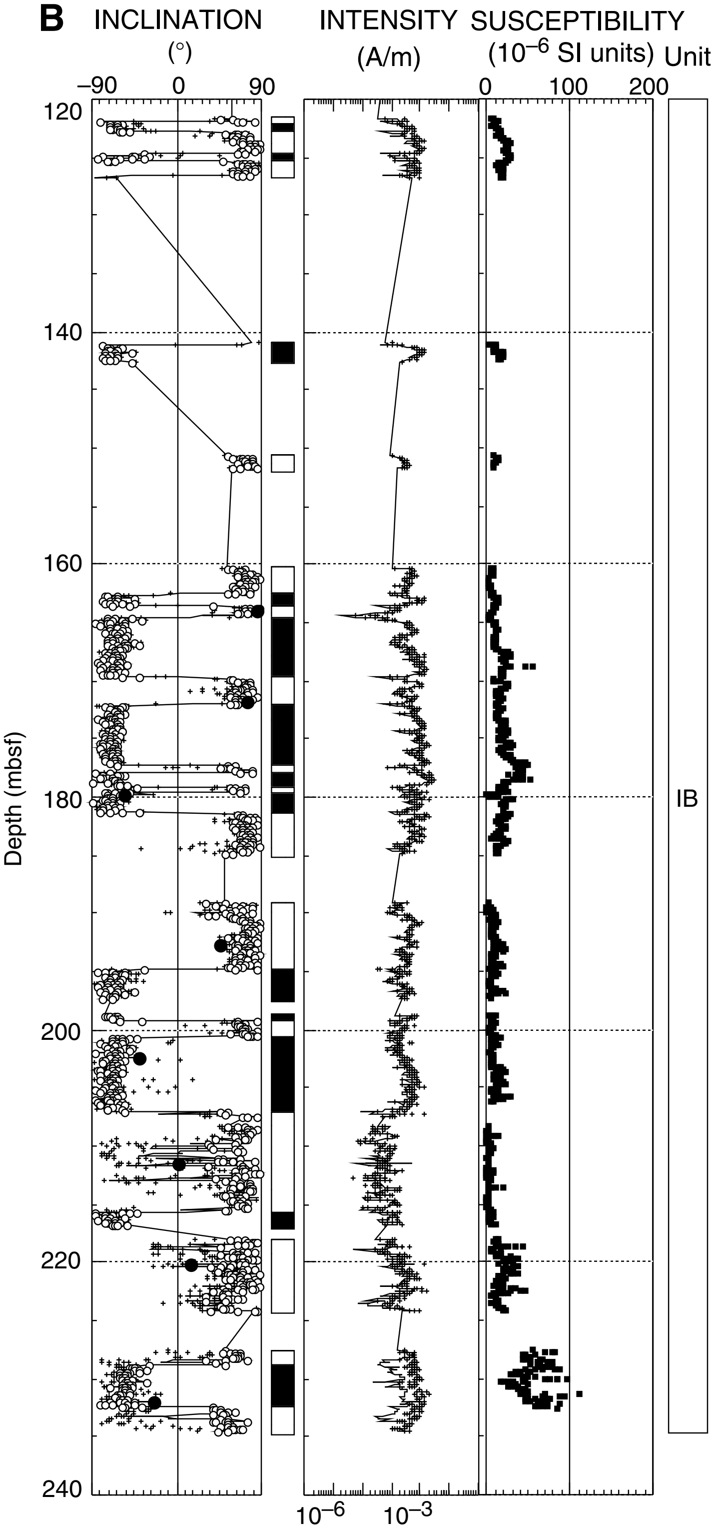

Figure F41. Average NRM intensity and MST susceptibility of each lithologic and basement unit. Large solid circles give the average values for all sediments and basement rocks. The horizontal bars show the range between maximum and minimum values in the respective units.

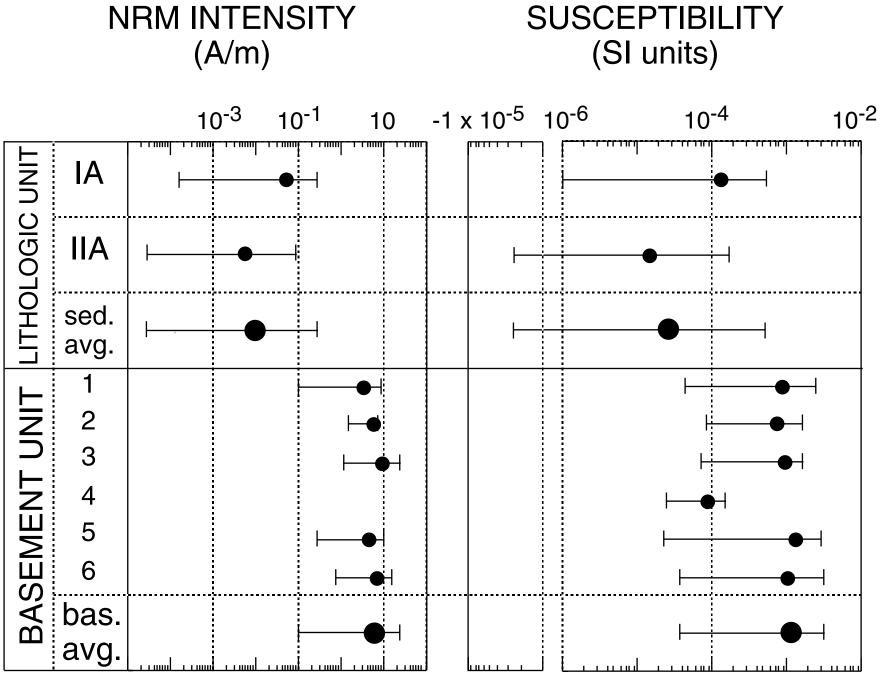

Figure F42. Hole 1140A inclination, intensity of remanent magnetization, and susceptibility of basement rocks vs. depth. Crosses and lines represent remanent magnetization before and after AF demagnetization at 40 mT, respectively. Inclinations of NRM and characteristic inclinations of discrete samples are represented by solid and open circles, respectively. MST, AMST, and discrete-sample susceptibilities are represented by lines, crosses and open circles, respectively. Basement units are shown on the right.

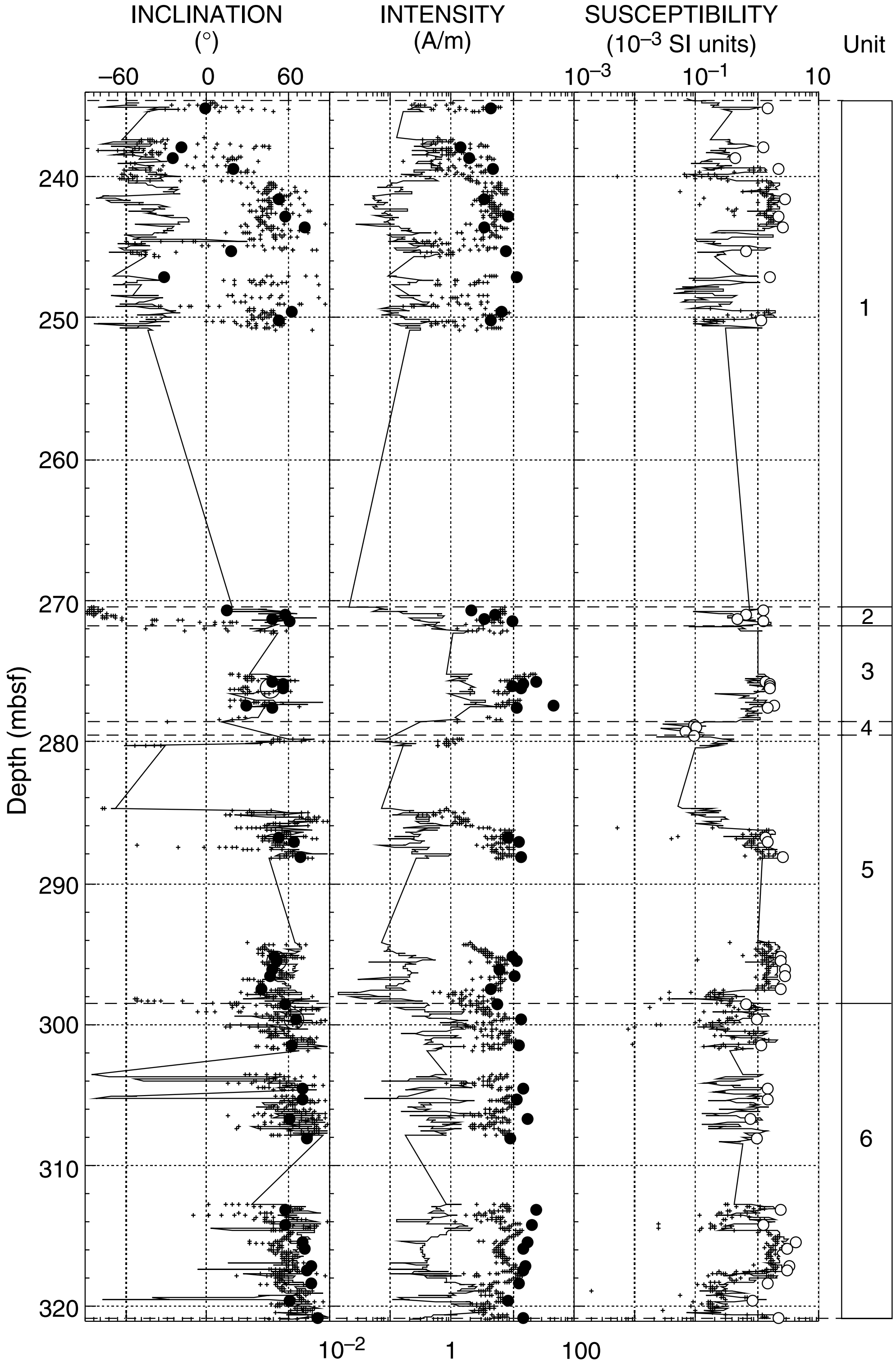

Figure F43. Stepwise AF demagnetization up to 60 mT at 7.5 cm of the archive half of Section 183-1140A-37R-4 from basement Unit 6. The magnetization has a MDF of 20 mT and a two-component magnetization. J_0 is the magnetization intensity before AF treatment.

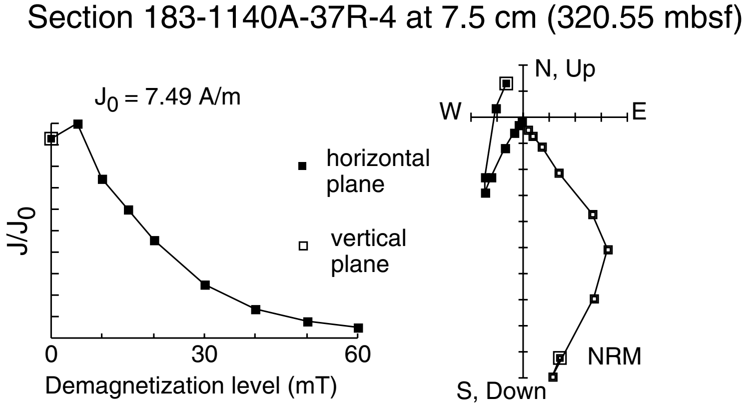

Figure F44. **A.** Thermal demagnetization of Sample 183-1140A-27R-2, 83–85 cm, from basement Unit 1. The intensity decreases mostly at low temperatures up to 200°C. Directions are scattered, and no characteristic inclination could be determined. **B.** Thermal demagnetization of Sample 183-1140A-34R-5, 10–12 cm, from basement Unit 6. Unblocking temperatures are ~560° and ~350°C and indicate that both titanomagnetite and titanomaghemite are the magnetic minerals. The NRM is a stable single component. J_0 is the magnetization intensity before thermal treatment.

A Sample 183-1140A-27R-2, 83-85 cm (241.54 mbsf)

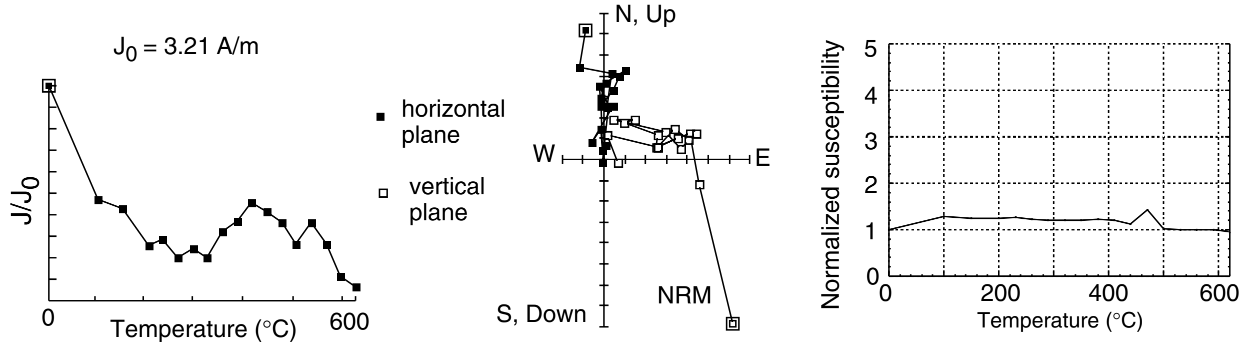

B Sample 183-1140A-34R-5, 10-12 cm (299.51 mbsf)

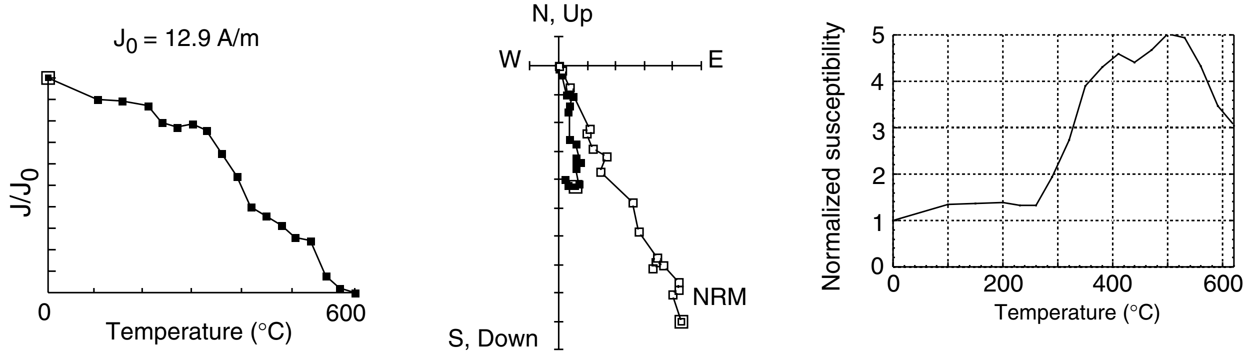

Figure F45. Downhole index properties and compressional wave velocities at Site 1140. The horizontal solid line separates the two lithologic units, and the dashed line shows the boundary between Subunits IA and IB. Lithologic units are shown on the right. Discrete measurements are of (**A**) bulk density, (**B**) grain density, (**C**) porosity, and (**D**) compressional wave velocities.

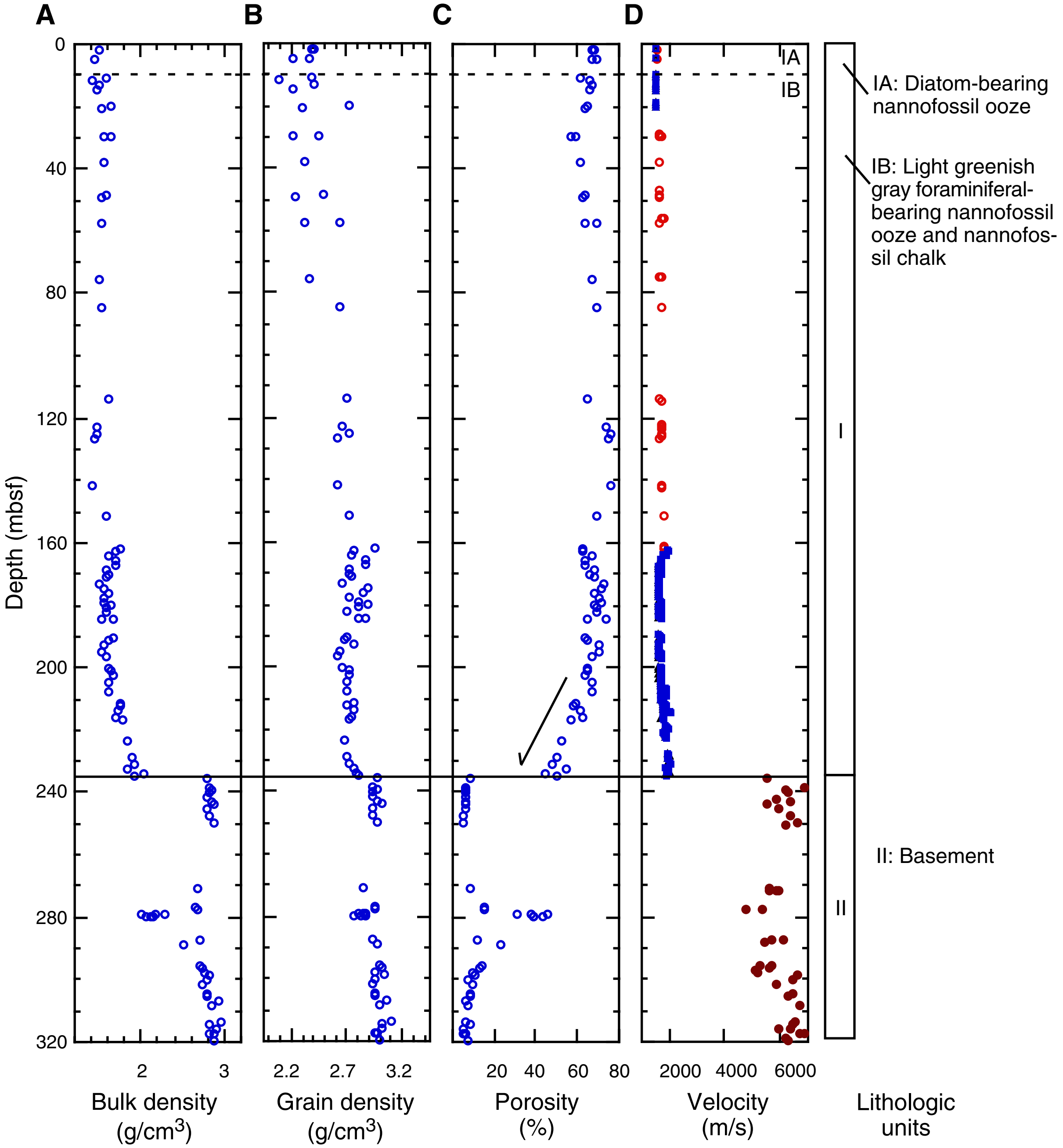

Figure F46. Downhole index properties profiles for discrete samples from basement Units 2–19 in Hole 1140A. Discrete measurements are of (**A**) bulk density, (**B**) grain density, (**C**) porosity, (**D**) discrete sample velocities. Black boxes at right denote recovery. Dashed gray lines indicate boundary of the basement units. This figure is a subset of results shown in Figure F45, p. 82.

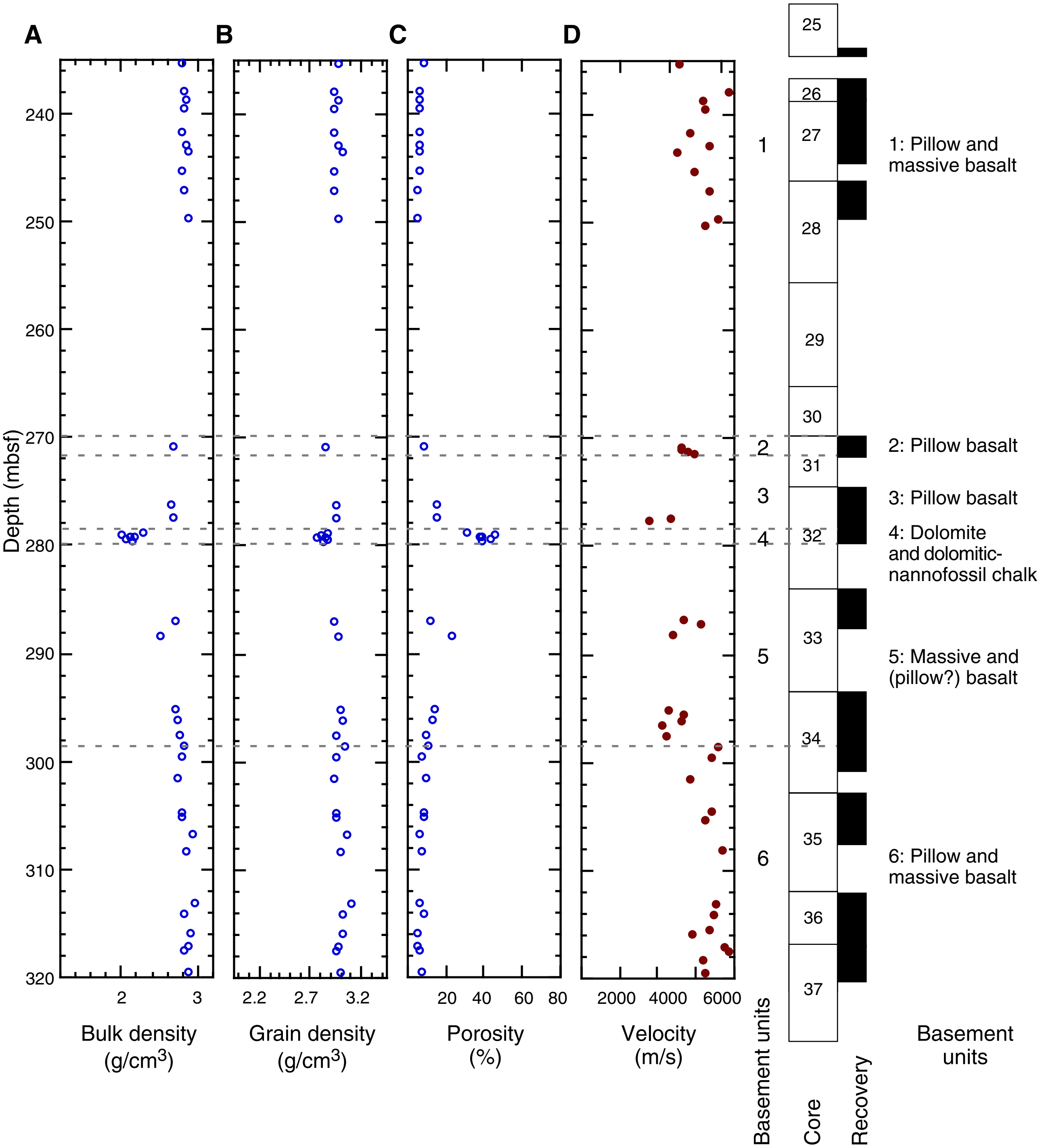

Figure F47. Downhole profiles of MST measurements together with discrete measurements. **A.** GRAPE bulk density (red squares) and bulk density derived from discrete samples (blue connected by solid line). **B.** Whole-core measurements of magnetic susceptibility. **C.** Natural gamma ray. Horizontal solid line separates the lithologic units, and the dashed line shows the boundary between Subunits IA and IB. Lithologic units are shown to the right.

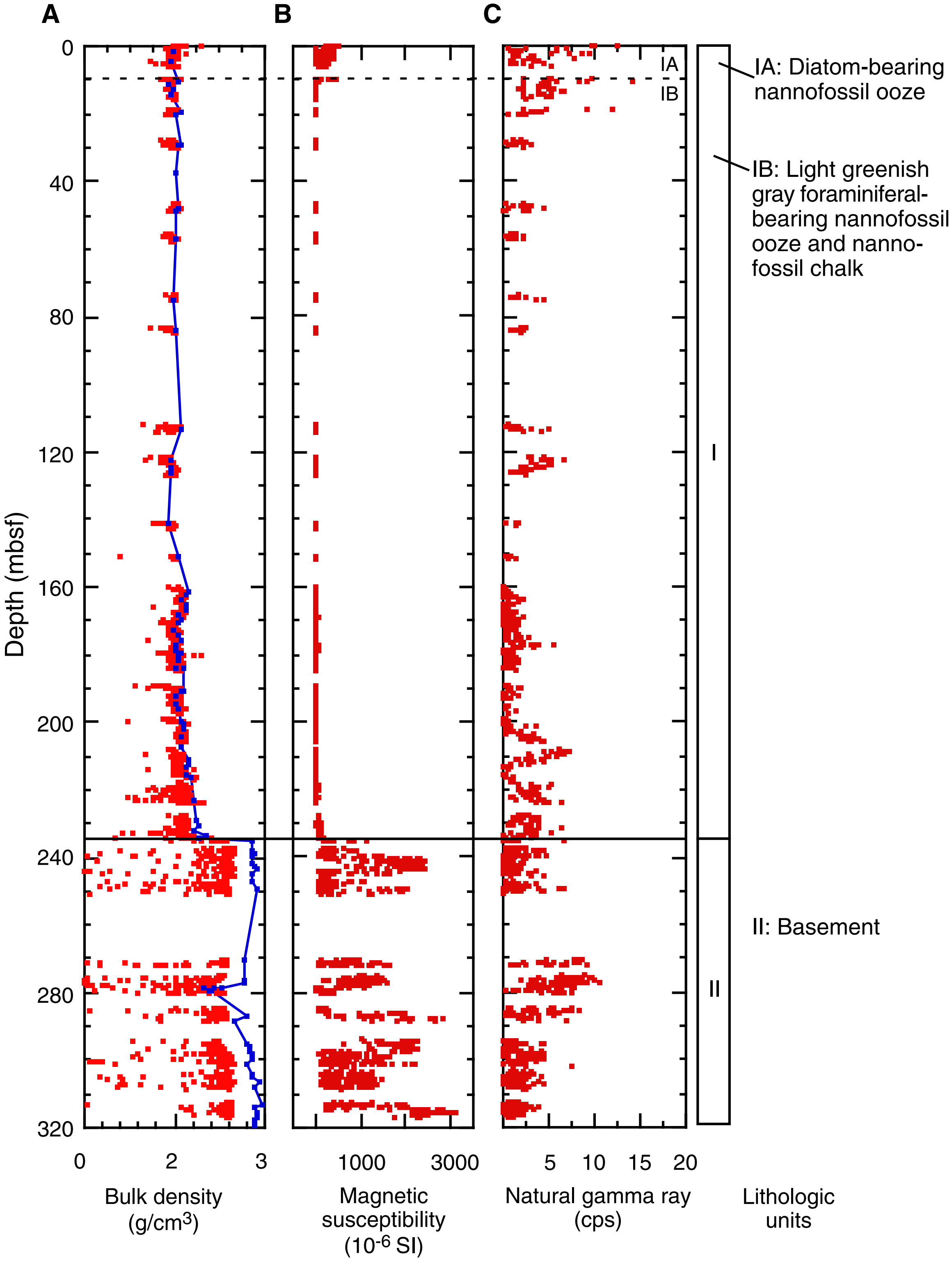

Figure F48. Downhole profile of thermal conductivity on soft sediments (whole-core measurement) and of hard rocks (measured on split-core pieces). Horizontal solid line separates the lithologic units.

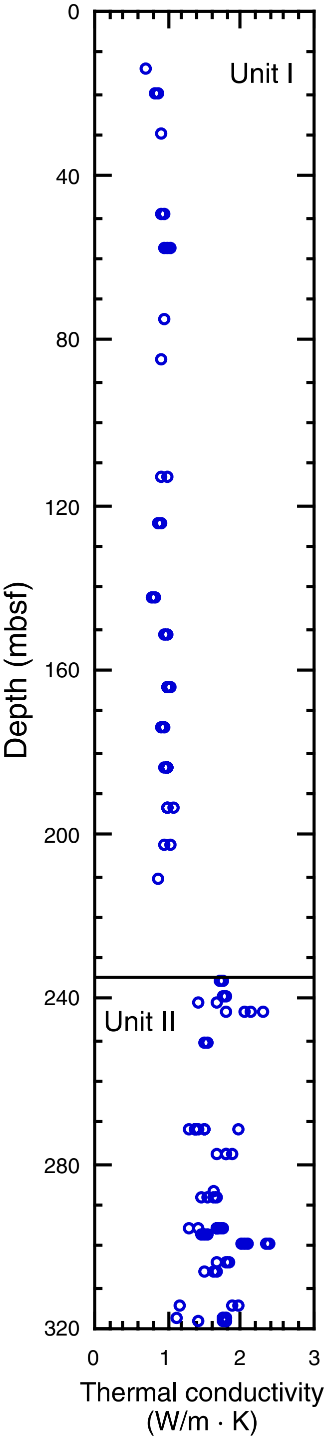

Figure F49. Comparison of densities determined from core samples and GRAPE measurement, and compressional wave velocities from downhole logs and core samples. Raw and robust mode filtered data are shown. (Continued on next page.)

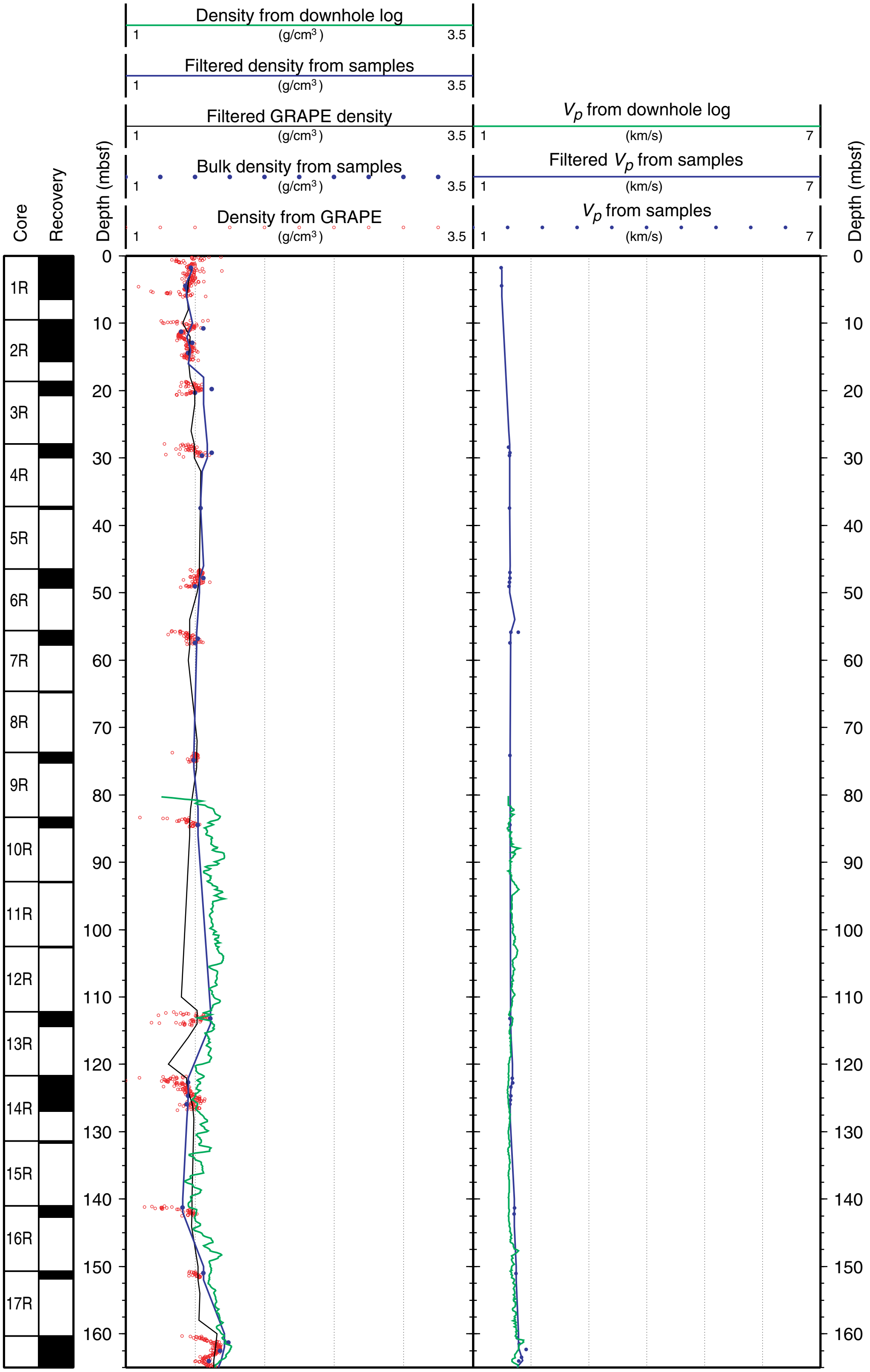

Figure F49 (continued).

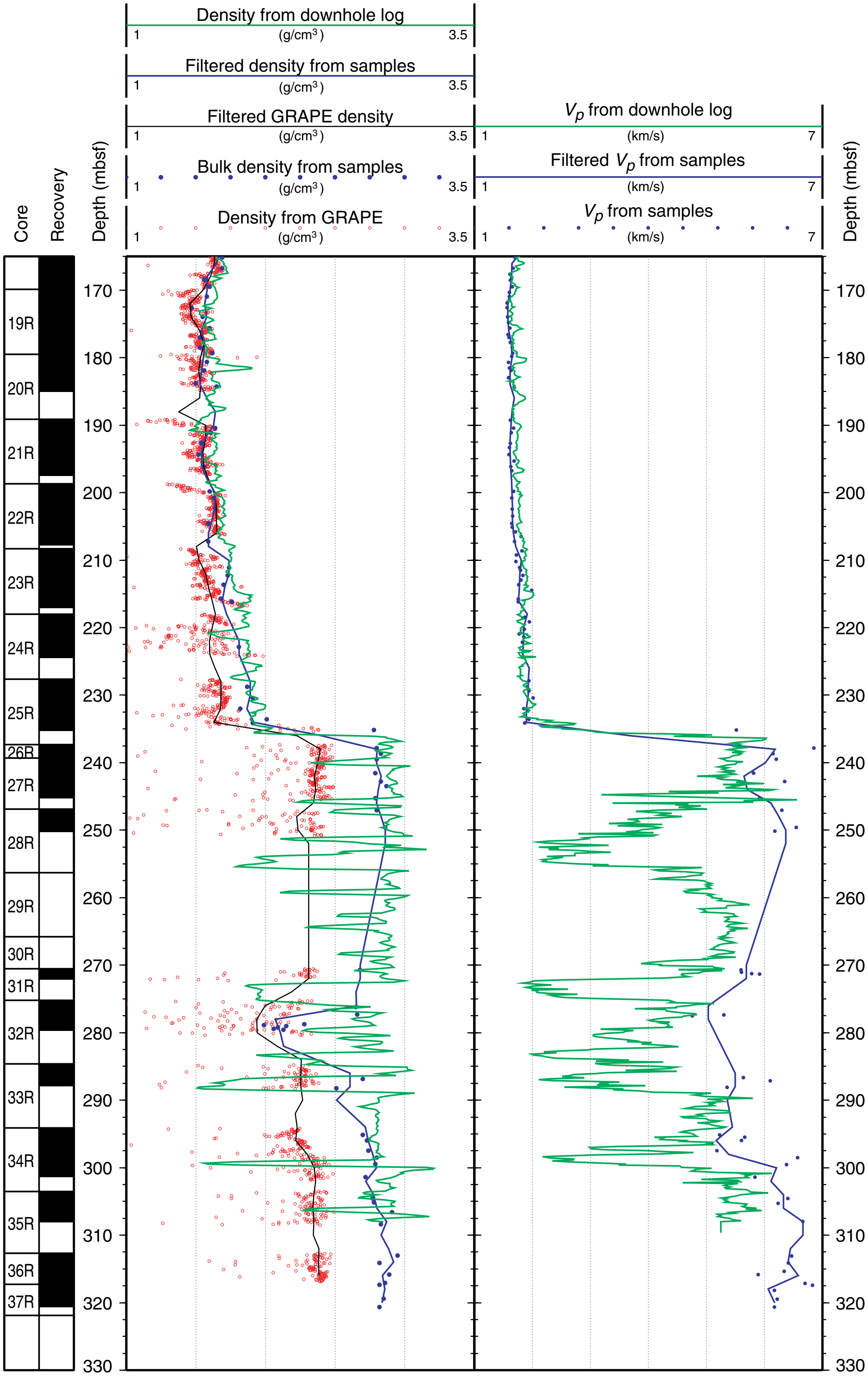

Figure F50. Comparison of depth vs. two-way traveltime (TWT) relationships. **A.** Site 1140 traveltimes based on the sum of transit times from the sonic tool agree very well with results from the well seismic tool (WST), which measures one-way traveltimes directly. TWTs from discrete samples are underestimated in basement because they are biased toward high values (Fig. **F49,** p. 86). **B.** TWTs for Site 1139 from the downhole sonic log and from discrete samples disagree strongly because of low data quality and data gaps. We acquired no WST data at Site 1139.

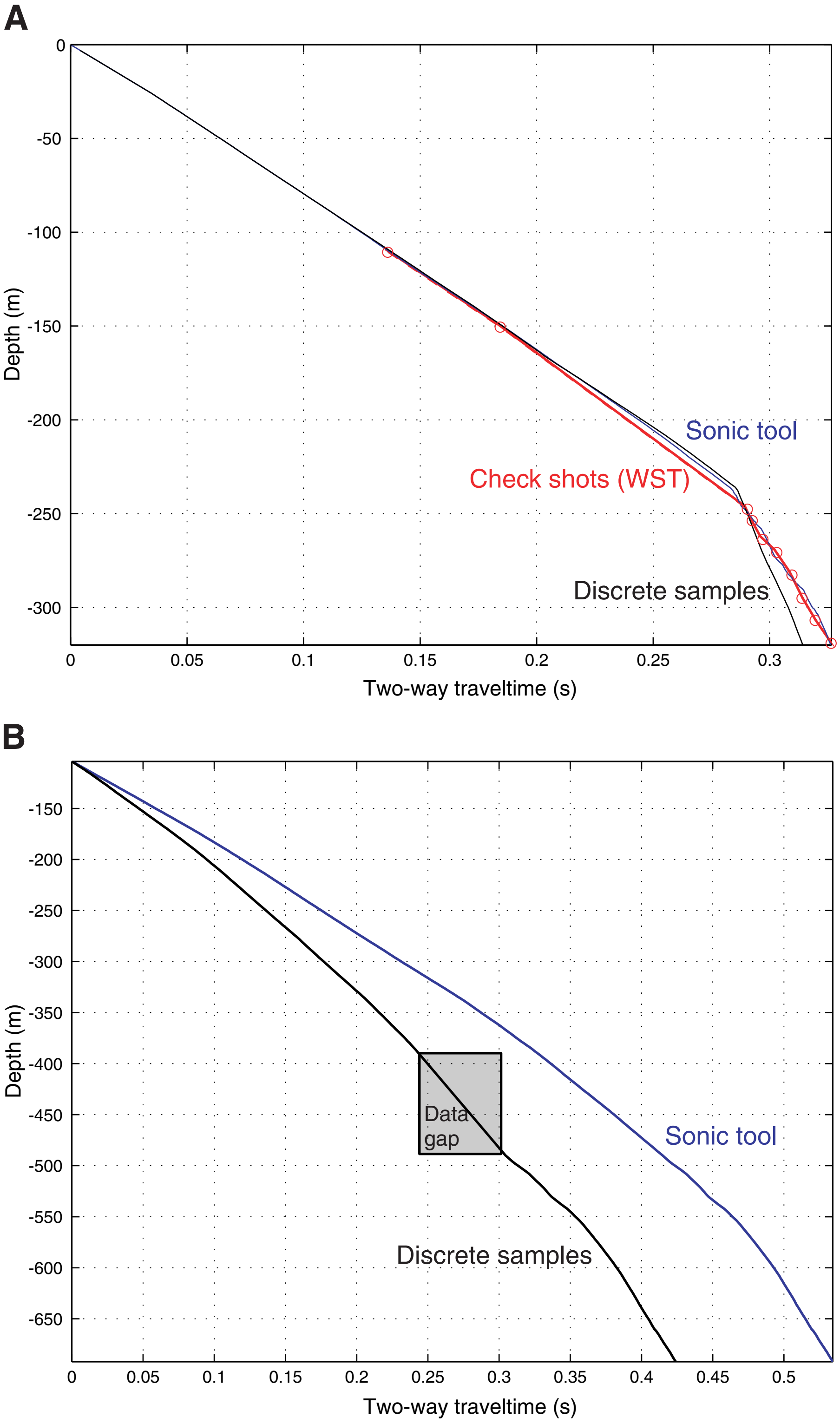

Figure F51. Composite of core recovery, lithostratigraphy, and age and (**A**) density and velocity as a function of depth, (**B**) density and velocity as a function of two-way traveltime (TWT), (**C**) impedance, (**D**) reflection coefficients without interbed multiples and transmission losses, (**E**) reflection coefficients with interbed multiples and transmission losses, and (**F**) synthetic seismograms based on (D) (black) and (E) (red) as a function of TWT. sbsf = seconds below seafloor. (**Figure shown on next page.**)

Figure F51. (Caption shown on previous page.)

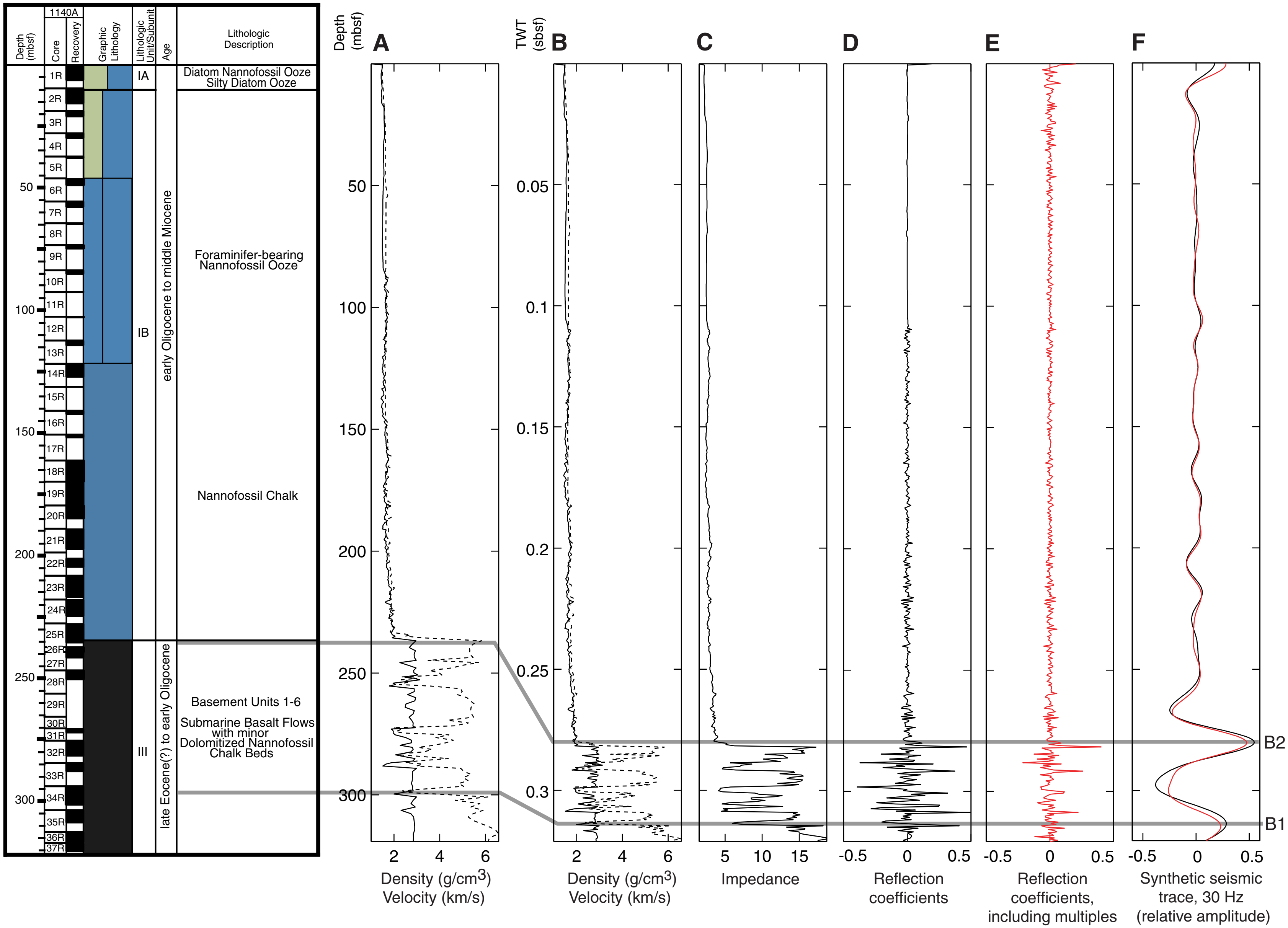

Figure F52. Portion of seismic reflection line 06 from *Marion Dufresne* cruise 109, across Site 1140, and a synthetic seismic trace from Figure F51, p. 89, including multiples and transmission losses. Reflections tied to the synthetic seismogram are labeled. B = Basement. The vertical exaggeration is ~16:1 at the seafloor.

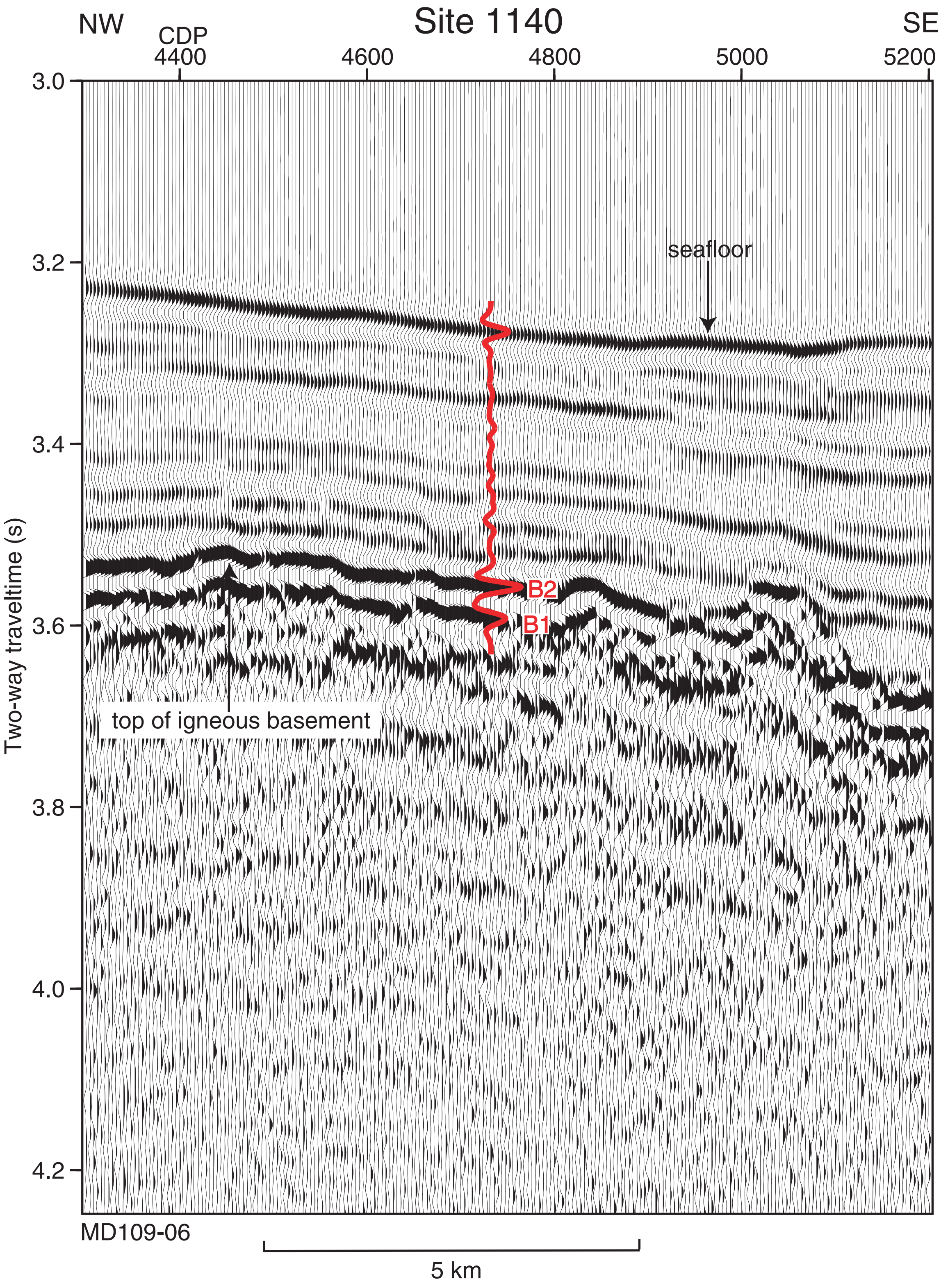

Figure F53. Logging data from Hole 1140A.

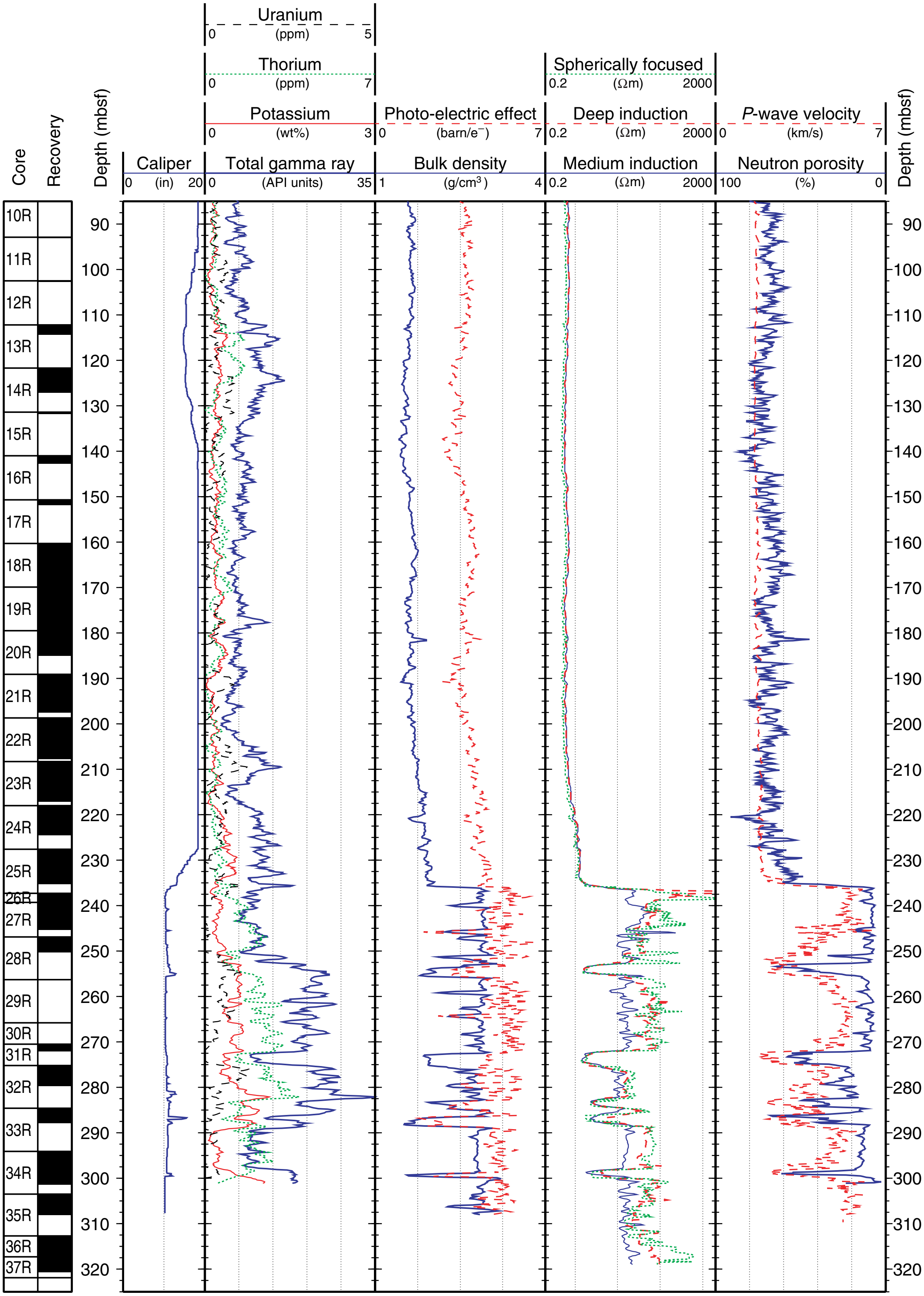

Figure F54. Comparison of densities determined from downhole logs, core samples, compressional wave velocities from downhole logs (lines) and discrete core samples (crosses), and natural gamma-ray data from the MST and from downhole.

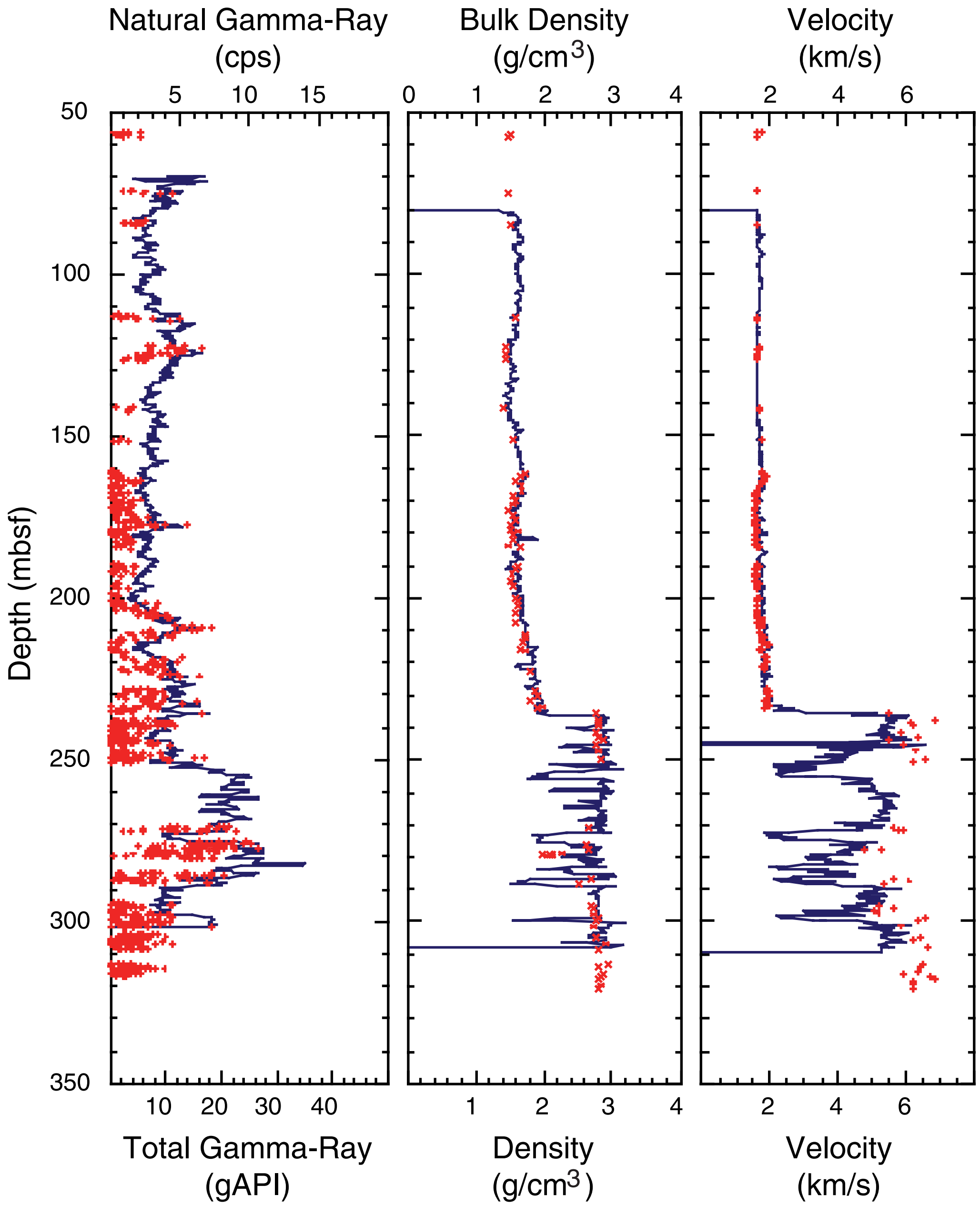

Figure F55. Composite of wireline logs at Site 1140 compared to the core-derived lithostratigraphy. The integrated interpretation of FMS images and standard logs enable clear identification of the displayed unit boundaries. The log-derived basement unit boundaries are given in Table T15, p. 120 (see "Physical Volcanology," p. 12). SGR = total gamma-ray signature. Shading = sedimentary regions with low density, resistivity, velocity, and high porosity. Other abbreviations are defined in Figure F15, p. 51.

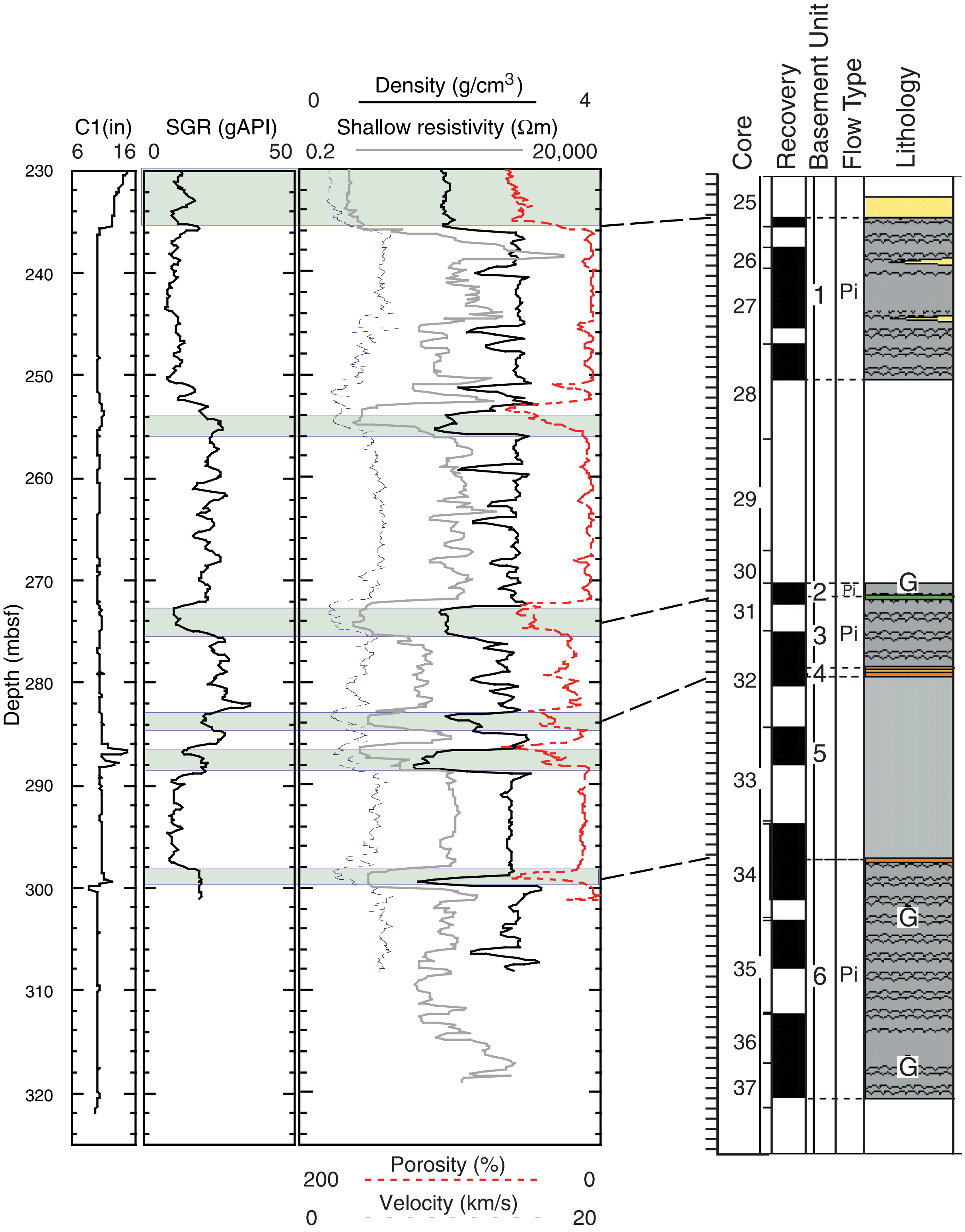

Figure F56. Crossplots of (**A**) shallow resistivity vs. compressional wave velocity and (**B**) density vs. porosity. The basalts in the igneous basement generally show the highest densities, resistivities, compressional wave velocities, and the lowest porosities. Sediments of lithologic basement Unit I (see "Lithostratigraphy," p. 3) exhibit low density, low resistivity, low velocity, and high porosity values, and are therefore distinct from the crystalline rocks. Sediments interbedded with pillow basalts show intermediate physical property values; however, the fields overlap and are not clearly distinguished. (Continued on next page.)

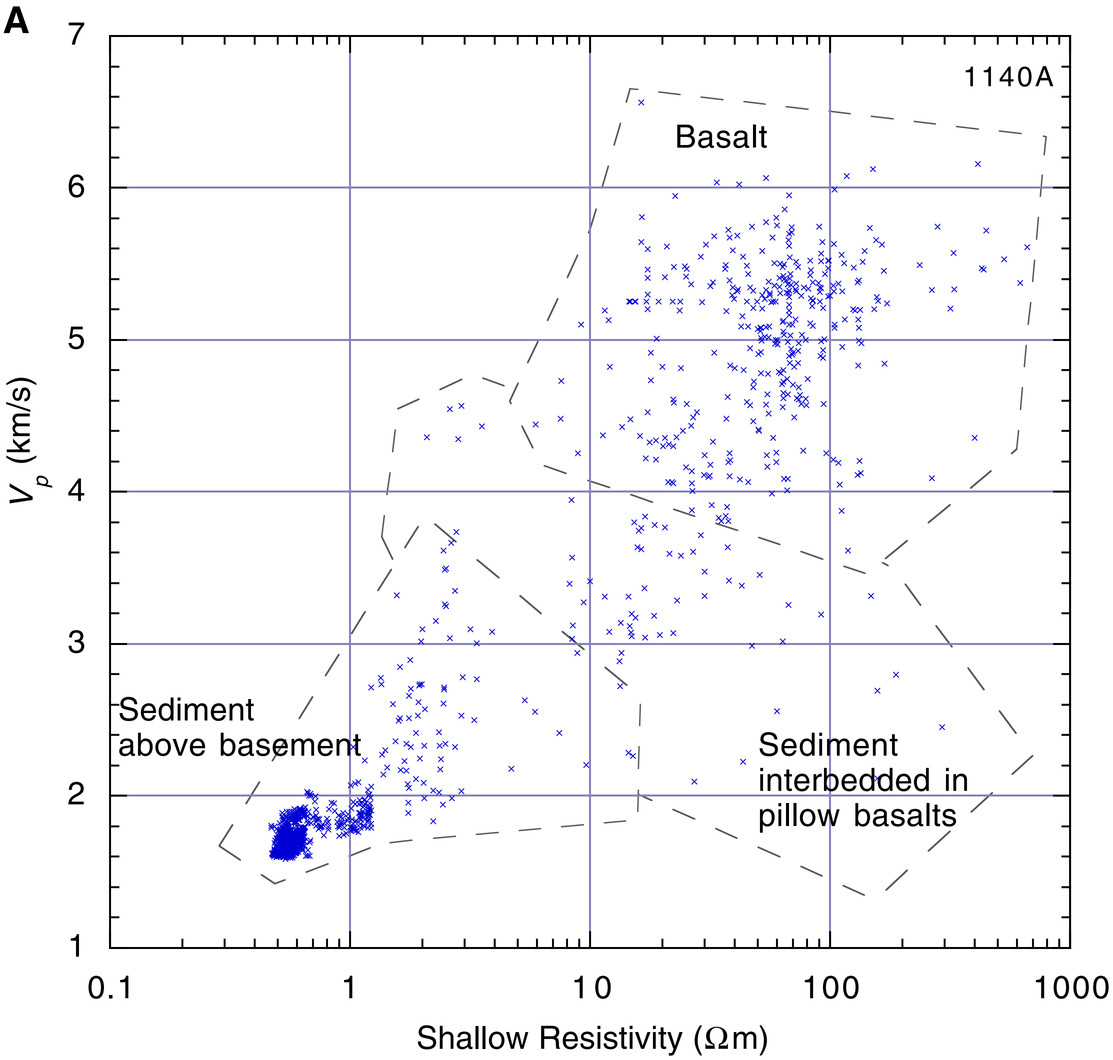

Figure F56 (continued).

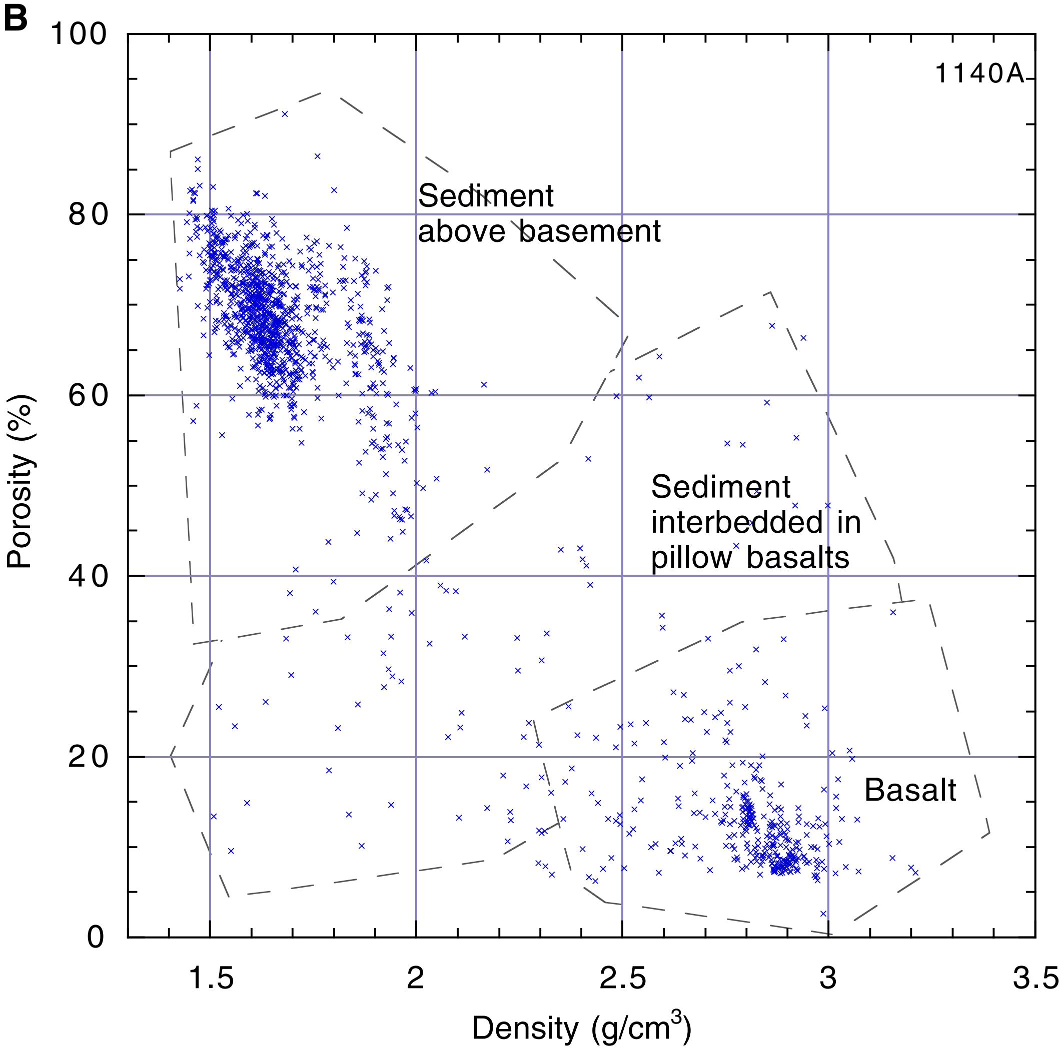

Figure F57. FMS image (from 262.5 to 267 mbsf) displaying typical pillow lava structures in basement Unit 2. Pillow rims are characterized by low resistive bands, and larger interstitial zones between individual pillows show larger irregular low resistive areas. Calipers C1 and C2 reflect the good hole condition. Horizontal exaggeration = 4.

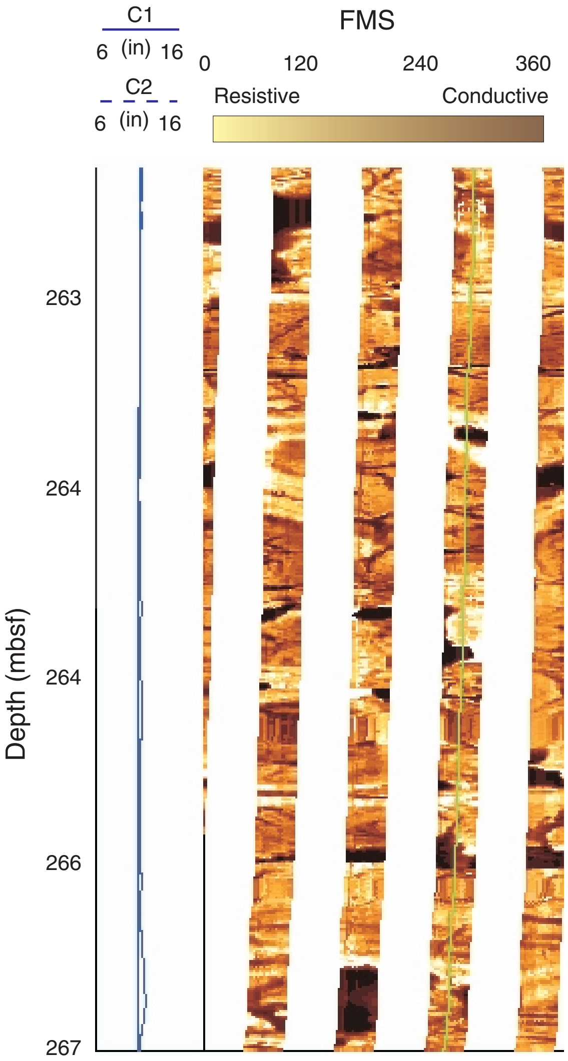

Figure F58. FMS image (from 270 to 276 mbsf) displaying basement Units 2 and 3. These units are separated by a ~2.5-m-thick sedimentary layer. Calipers C1 and C2 reflect the good hole condition. Horizontal exaggeration = 4.

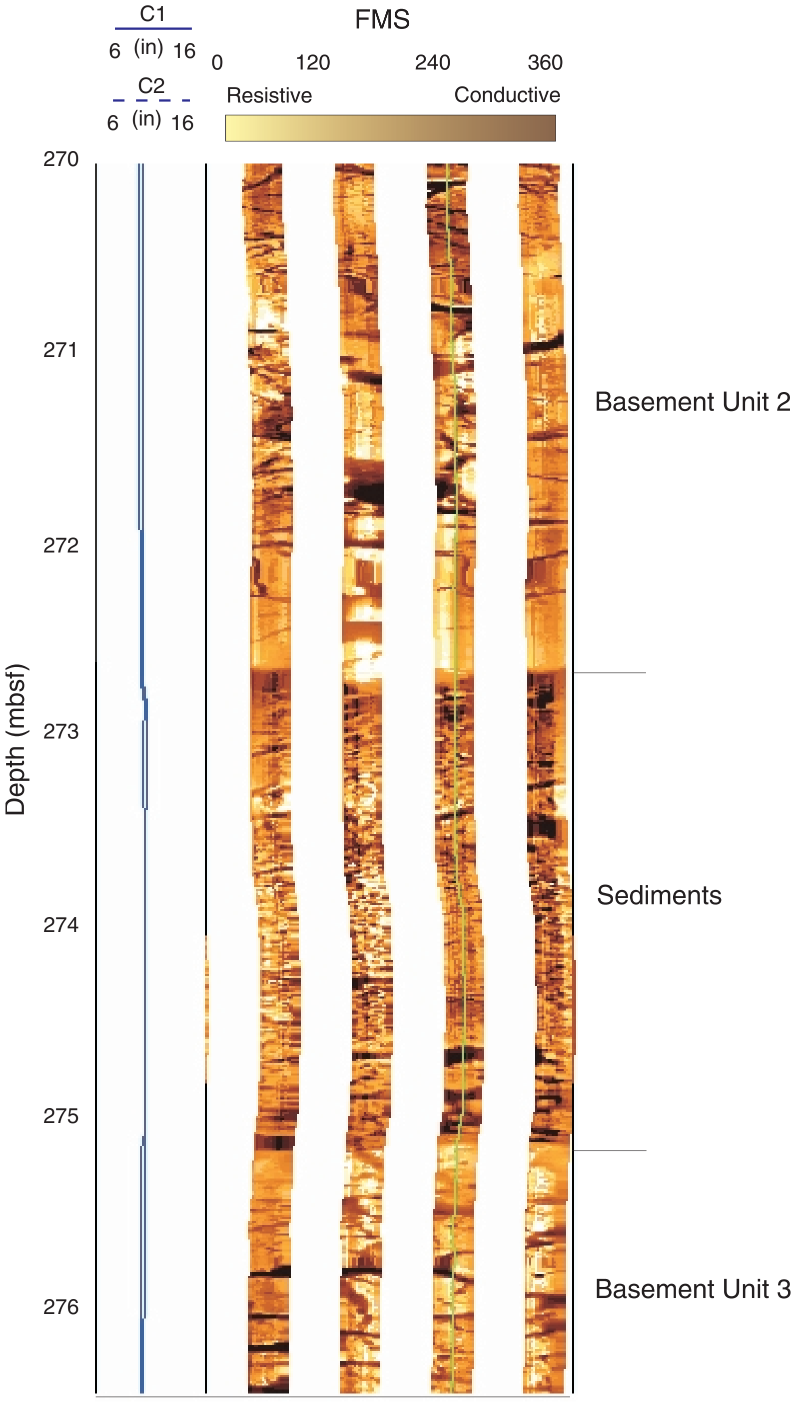

Figure F59. FMS image (from 282 to 288 mbsf) displaying two sedimentary layers with a intervening lava flow. The upper sediments (283–284.5 mbsf) correspond to basement Unit 4. The lower sedimentary layer is affected by hole breakouts, which underlines its weak or altered nature. Calipers C1 and C2 reflect the hole condition. Horizontal exaggeration = 4.

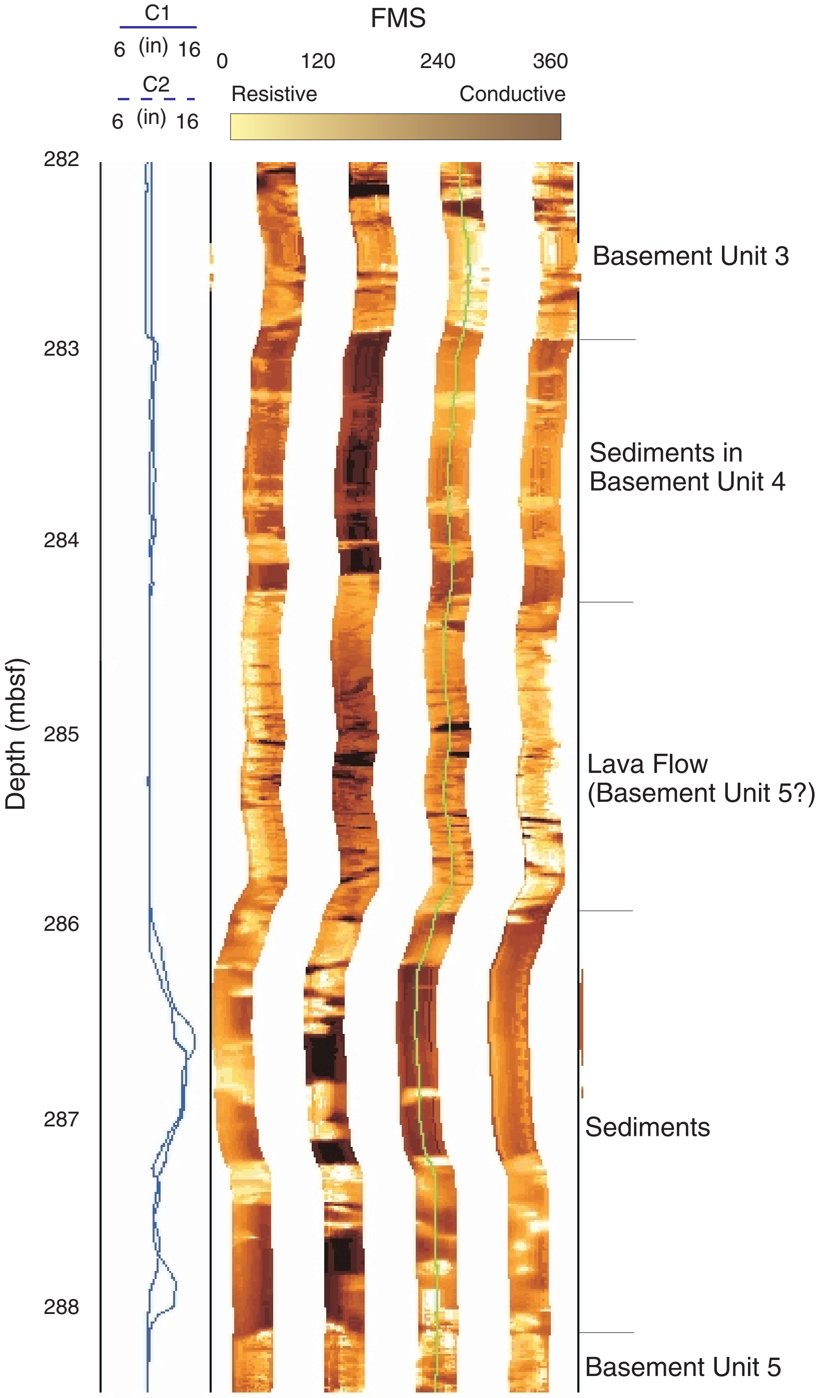

Figure F60. FMS image (from 294 to 300 mbsf) displaying the transition from basement Units 5–6. The dips of the planar fractures scatter around 240°. This FMS image is a good example of the massive lava flows. The near-vertical features between 296 and 298 mbsf correlate with features in the cores interpreted as filled pipe vesicles or late stage segregations (see "Alteration and Weathering," p. 19, and "Physical Volcanology," p. 12). Calipers C1 and C2 reflect the hole condition. Horizontal exaggeration = 4.

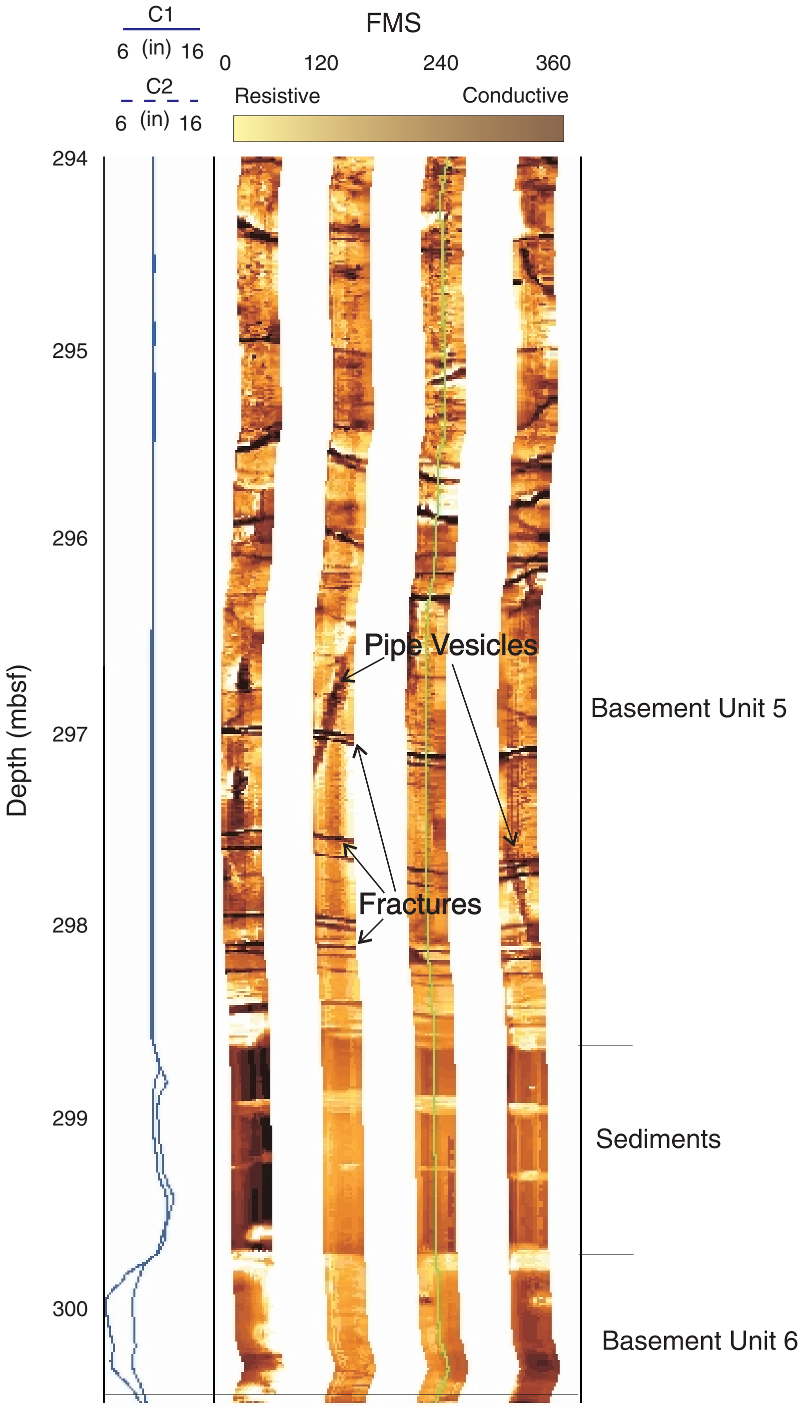

Table T1. Coring summary for Hole 1140.

				Length (m)		
Core	Date (Jan 1999)	Time (UTC)	Depth (mbsf)	Cored	Recovered	Recovery (%)
183-1140A-						
1R	22	2005	0.0-9.5	9.5	6.56	69.1
2R	22	2120	9.5-18.6	9.1	6.23	68.5
3R	22	2215	18.6-27.9	9.3	2.22	23.9
4R	22	2255	27.9-37.2	9.3	2.14	23.0
5R	22	2325	37.2-46.5	9.3	0.50	5.4
6R	23	0035	46.5-55.6	9.1	2.88	31.6
7R	23	0145	55.6-64.6	9.0	2.29	25.4
8R	23	0230	64.6-73.7	9.1	0.32	3.5
9R	23	0310	73.7-83.3	9.6	1.64	17.1
10R	23	0355	83.3-92.9	9.6	1.69	17.6
11R	23	0445	92.9-102.5	9.6	0.18	1.9
12R	23	0535	102.5-112.2	9.7	0.25	2.6
13R	23	0625	112.2-121.7	9.5	2.24	23.6
14R	23	0715	121.7-131.4	9.7	5.38	55.5
15R	23	0810	131.4-141.0	9.6	0.37	3.9
16R	23	0905	141.0-150.7	9.7	1.76	18.1
17R	23	0950	150.7-160.3	9.6	1.22	12.7
18R	23	1030	160.3-169.9	9.6	9.71	101.1
19R	23	1105	169.9-179.5	9.6	9.82	102.3
20R	23	1150	179.5-189.1	9.6	5.55	57.8
21R	23	1230	189.1-198.7	9.6	8.44	87.9
22R	23	1310	198.7-208.3	9.6	9.14	95.2
23R	23	1355	208.3-218.0	9.7	8.84	91.1
24R	23	1445	218.0-227.6	9.6	6.48	67.5
25R	23	1750	227.6-237.3	9.7	7.70	79.4
26R	23	2125	237.3-239.3	2.0	2.12	106
27R	24	0350	239.3-246.9	7.6	6.01	79.1
28R	24	0830	246.9-256.3	9.4	3.36	35.7
29R	24	1350	256.3-265.8	9.5	0.00	0.0
30R	24	1905	265.8-270.5	4.7	0.00	0.0
31R	25	0140	270.5-275.2	4.7	1.59	33.8
32R	25	0440	275.2-284.6	9.4	4.52	48.1
33R	25	0950	284.6-294.1	9.5	3.33	35.1
34R	25	1700	294.1-303.5	9.4	7.29	77.6
35R	26	0055	303.5-312.7	9.2	4.63	50.3
36R	26	0545	312.7-317.3	4.6	5.09	110.7
37R	26	0935	317.3-321.9	4.6	3.37	73.3
			Totals:	321.9	144.86	45.0

Note: UTC = Universal Time Coordinated. This table is also available in **ASCII format.**

Table T2. Expanded coring summary for Hole 1140A. (See table note. Continued on next three pages.)

Core	Date (Jan 1999)	Time (UTC)	Depth (mbsf)	Length (m)		Recovery (%)	Section	Length (m)		Section depth (mbsf)	Catwalk samples	Comment
				Cored	Recovered			Liner	Curated			
183-1140A-												
1R	22	2005	0.0-9.5	9.5	6.56	69.1						
							1	1.50	1.50	0.0-1.5		
							2	1.50	1.50	1.5-3.0		Other
							3	1.50	1.50	3.0-4.5		
							4	0.90	0.90	4.5-5.4	HS	Other
							5	1.02	0.66	5.4-6.06		Other
							CC(w/5)	0.14	0.14	6.06-6.2	PAL	
								6.56	6.20			
2R	22	2120	9.5-18.6	9.1	6.23	68.5						
							1	1.50	1.50	9.5-11.0		
							2	1.50	1.50	11.0-12.5		
							3	1.50	1.50	12.5-14.0	HS	
							4	1.51	1.53	14.0-15.53		
							CC(w/CC)	0.22	0.22	15.53-15.75	PAL	
								6.23	6.25			
3R	22	2215	18.6-27.9	9.3	2.22	23.9						
							1	1.50	1.50	18.6-20.1		
							2	0.54	0.54	20.1-20.64	HS	
							CC(w/2)	0.18	0.18	20.64-20.82	PAL	
								2.22	2.22			
4R	22	2255	27.9-37.2	9.3	2.14	23.0						
							1	1.50	1.50	27.9-29.4		
							2	0.48	0.48	29.4-29.88	HS	
							CC(w/2)	0.16	0.16	29.88-30.04	PAL	
								2.14	2.14			
5R	22	2325	37.2-46.5	9.3	0.5	5.4						
							CC(w/CC)	0.50	0.50	37.2-37.7	PAL	
								0.50	0.50			
6R	23	0035	46.5-55.6	9.1	2.88	31.6						
							1	1.50	1.50	46.5-48.0		
							2	1.20	1.20	48.0-49.2	HS	
							CC(w/2)	0.18	0.18	49.2-49.38	PAL	
								2.88	2.88			
7R	23	0145	55.6-64.6	9.0	2.29	25.4						
							1	1.50	1.50	55.6-57.1		
							2	0.57	0.57	57.1-57.67	HS	
							CC(w/2)	0.22	0.22	57.67-57.89	PAL	
								2.29	2.29			
8R	23	0230	64.6-73.7	9.1	0.32	3.5						
							CC(w/CC)	0.32	0.32	64.6-64.92	PAL	
								0.32	0.32			
9R	23	0310	73.7-83.3	9.6	1.64	17.1						
							1	1.42	1.42	73.7-75.12	HS	
							CC(w/CC)	0.22	0.22	75.12-75.34	PAL	
								1.64	1.64			
10R	23	0355	83.3-92.9	9.6	1.69	17.6						
							1	1.42	1.42	83.3-84.72	HS	
							CC(w/CC)	0.27	0.27	84.72-84.99	PAL	
								1.69	1.69			
11R	23	0445	92.9-102.5	9.6	0.18	1.9						
							CC(w/CC)	0.18	0.18	92.9-93.08	PAL	
								0.18	0.18			
12R	23	0535	102.5-112.2	9.7	0.25	2.6						
							CC(w/CC)	0.25	0.25	102.5-102.75	PAL	
								0.25	0.25			
13R	23	0625	112.2-121.7	9.5	2.24	23.6						
							1	1.50	1.50	112.2-113.7		
							2	0.50	0.50	113.7-114.2	HS	
							CC(w/2)	0.24	0.24	114.2-114.44	PAL	
								2.24	2.24			
14R	23	0715	121.7-131.4	9.7	5.38	55.5						
							1	1.50	1.50	121.7-123.2		
							2	1.50	1.50	123.2-124.7	HS	
							3	1.50	1.50	124.7-126.2		
							4	0.59	0.59	126.2-126.79		
							CC(w/4)	0.29	0.29	126.79-127.08	PAL	
								5.38	5.38			

Table T2 (continued).

Core	Date (Jan 1999)	Time (UTC)	Depth (mbsf)	Length (m)		Recovery (%)	Section	Length (m)		Section depth (mbsf)	Catwalk samples	Comment
				Cored	Recovered			Liner	Curated			
15R	23	0810	131.4-141	9.6	0.37	3.9						
							CC(w/CC)	0.37	0.37	131.4-131.77	PAL	
								0.37	0.37			
16R	23	0905	141-150.7	9.7	1.76	18.1						
							1	1.50	1.50	141.0-142.5	HS	
							CC(w/CC)	0.26	0.26	142.5-142.76	PAL	
								1.76	1.76			
17R	23	0950	150.7-160.3	9.6	1.22	12.7						
							1	1.01	1.01	150.7-151.71	HS	
							CC(w/1)	0.21	0.21	151.71-151.92	PAL	
								1.22	1.22			
18R	23	1030	160.3-169.9	9.6	9.71	101.1						
							1	1.50	1.50	160.3-161.8		
							2	1.50	1.50	161.8-163.3		
							3	1.50	1.50	163.3-164.8		
							4	1.50	1.50	164.8-166.3		
							5	1.50	1.50	166.3-167.8	HS	
							6	1.50	1.50	167.8-169.3		
							7	0.40	0.40	169.3-169.7		
							CC(w/7)	0.31	0.31	169.7-170.01	PAL	
								9.71	9.71			
19R	23	1105	169.9-179.5	9.6	9.82	102.3						
							1	1.50	1.50	169.9-171.4		
							2	1.50	1.50	171.4-172.9		
							3	1.50	1.50	172.9-174.4		
							4	1.50	1.50	174.4-175.9		
							5	1.50	1.50	175.9-177.4	HS	
							6	1.50	1.50	177.4-178.9		
							7	0.61	0.61	178.9-179.51		
							CC(w/7)	0.21	0.21	179.51-179.72	PAL	
								9.82	9.82			
20R	23	1150	179.5-189.1	9.6	5.55	57.8						
							1	1.50	1.50	179.5-181.0		
							2	1.50	1.50	181.0-182.5		
							3	1.50	1.50	182.5-184.0	HS	
							4	0.85	0.85	184.0-184.85		
							CC(w/4)	0.20	0.20	184.85-185.05	PAL	
								5.55	5.55			
21R	23	1230	189.1-198.7	9.6	8.44	87.9						
							1	1.50	1.50	189.1-190.6		
							2	1.50	1.50	190.6-192.1		
							3	1.50	1.50	192.1-193.6		
							4	1.50	1.50	193.6-195.1		
							5	1.50	1.50	195.1-196.6	HS	
							6	0.74	0.74	196.6-197.34		
							CC(w/6)	0.20	0.20	197.34-197.54	PAL	
								8.44	8.44			
22R	23	1310	198.7-208.3	9.6	9.14	95.2						
							1	1.50	1.50	198.7-200.2		
							2	1.50	1.50	200.2-201.7		
							3	1.50	1.50	201.7-203.2		
							4	1.50	1.50	203.2-204.7		
							5	1.50	1.50	204.7-206.2	HS	
							6	1.44	1.44	206.2-207.64		
							CC(w/CC)	0.20	0.20	207.64-207.84	PAL	
								9.14	9.14			
23R	23	1355	208.3-218	9.7	8.84	91.1						
							1	1.50	1.50	208.3-209.8		
							2	1.50	1.50	209.8-211.3		
							3	1.50	1.50	211.3-212.8		
							4	1.50	1.50	212.8-214.3		
							5	1.50	1.50	214.3-215.8	HS	
							6	1.05	1.05	215.8-216.85		
							CC(w/6)	0.29	0.29	216.85-217.14	PAL	
								8.84	8.84			
24R	23	1445	218.0-227.6	9.6	6.48	67.5						
							1	1.50	1.50	218.0-219.5		
							2	1.50	1.50	219.5-221.0		

Table T2 (continued).

Core	Date (Jan 1999)	Time (UTC)	Depth (mbsf)	Length (m)		Recovery (%)	Section	Length (m)		Section depth (mbsf)	Catwalk samples	Comment
				Cored	Recovered			Liner	Curated			
							3	1.50	1.50	221.0-222.5		
							4	1.00	1.00	222.5-223.5	HS	
							5	0.74	0.74	223.5-224.24		
							CC(w/5)	0.24	0.24	224.24-224.48	PAL	
								6.48	6.48			
25R	23	1750	227.6-237.3	9.7	7.70	79.4						
							1	1.50	1.50	227.6-229.1		
							2	1.50	1.50	229.1-230.6		
							3	1.50	1.50	230.6-232.1	HS	
							4	1.50	1.50	232.1-233.6		
							5	0.92	0.92	233.6-234.52	PAL	
							6	0.78	0.89	234.52-235.41		
								7.70	7.81			
26R	23	2125	237.3-239.3	2.0	2.12	106						
							1	0.79	1.19	237.3-238.49		
							2	1.33	1.12	238.49-239.61		
								2.12	2.31			
27R	24	0350	239.3-246.9	7.6	6.01	79.1						
							1	0.48	1.41	239.3-240.71		
							2	1.40	1.28	240.71-241.99		
							3	1.45	1.43	241.99-243.42		
							4	1.47	1.39	243.42-244.81		
							5	1.21	0.80	244.81-245.61		
								6.01	6.31			
28R	24	0830	246.9-256.3	9.4	3.36	35.7						
							1	0.54	1.42	246.9-248.32		
							2	1.47	1.03	248.32-249.35		
							3	1.35	1.50	249.35-250.85		
								3.36	3.95			
29R	24	1350	256.3-265.8	9.5	0.00	0.0						
30R	24	1905	265.8-270.5	4.7	0.00	0.0						
31R	25	0140	270.5-275.2	4.7	1.59	33.8						
							1	0.32	1.50	270.5-272.0		
							2	1.27	0.25	272.0-272.25		
								1.59	1.75			
32R	25	0440	275.2-284.6	9.4	4.52	48.1						
							1	0.39	1.50	275.2-276.7		
							2	1.35	1.50	276.7-278.2		
							3	1.32	1.46	278.2-279.66	PAL, HS	
							4	1.46	0.77	279.66-280.43		
								4.52	5.23			
33R	25	0950	284.6-294.1	9.5	3.33	35.1						
							1	0.33	1.42	284.6-286.02		
							2	1.50	1.36	286.02-287.38		
							3	1.50	0.96	287.38-288.34		
								3.33	3.74			
34R	25	1700	294.1-303.5	9.4	7.29	77.6						
							1	1.09	1.50	294.1-295.6		
							2	1.37	1.18	295.6-296.78		
							3	0.55	1.42	296.78-298.2		
							4	1.30	1.21	298.2-299.41		
							5	1.48	1.48	299.41-300.89		
							6	1.50	0.94	300.89-301.83		
								7.29	7.73			
35R	26	0055	303.5-312.7	9.2	4.63	50.3						
							1	0.70	1.47	303.5-304.97		
							2	0.94	1.50	304.97-306.47		
							3	1.57	1.44	306.47-307.91		
							4	1.42	0.6	307.91-308.51		
								4.63	5.01			
36R	26	0545	312.7-317.3	4.6	5.09	110.7						
							1	0.76	1.37	312.7-314.07		
							2	1.24	1.34	314.07-315.41		
							3	1.50	1.50	315.41-316.91		
							4	1.59	0.93	316.91-317.84		
								5.09	5.14			

Table T2 (continued).

Core	Date (Jan 1999)	Time (UTC)	Depth (mbsf)	Length (m)		Recovery (%)	Section	Length (m)		Section depth (mbsf)	Catwalk samples	Comment
				Cored	Recovered			Liner	Curated			
37R	26	0935	317.3-321.9	4.6	3.37	73.3						
							1	0.54	1.12	317.3-318.42		
							2	1.33	0.79	318.42-319.21		
							3	1.50	1.27	319.21-320.48		
							4	0.00	0.35	320.48-320.83		
								3.37	3.53			
			Totals:	321.9	144.86	45.0						

Note: UTC = Universal Time Coordinated. CC = core catcher (number in parenthesis indicates which section the core catcher is stored with), NS = all of the core catcher was used for paleontology sample. HS = headspace gas sample, PAL = paleontology sample. This table is also available in **ASCII format.**

Table T3. Summary of lithologic units at Site 1140.

Lithologic unit and subunit	Basement unit	Core interval	Depth (mbsf)	Thickness (m)	Age	Lithology	Interpretation
IA		1R-1, 0 cm to 2R-1, 61 cm	0.00–10.01	10.01	middle Miocene	Diatom nannofossil ooze and silty diatom ooze	Pelagically deposited sediment; bathyal depths (cold water)
IB		2R-1, 61 cm to 25R-5, 92 cm	10.01–234.52	224.51	middle Miocene to early Oligocene	Foraminifer-bearing nannofossil ooze and nannofossil chalk	Pelagically deposited sediment; bathyal depths
II	1–6	25R-5, 92 cm to 37R-4, 35 cm	234.52–321.90	87.38	early Oligocene to late Eocene(?)	Submarine pillow basalts with minor interbeds of dolomitized nannofossil chalk and dolomite	Submarine lava flows and pelagically deposited sediment; bathyal depths

Table T4. X-ray diffraction results, carbonate contents, and total and organic carbon contents expressed as $CaCO_3$ and C, respectively (see "**Organic and Inorganic Geochemistry**," p. 27) for Hole 1140A.

Core, section, interval (cm)	Depth (mbsf)	Minerals	$CaCO_3$ (wt%)	Carbon (wt%)	
				Total	Organic
Unit I					
183-1140A-					
1R-1, 12 cm	0.12	opal-A, quartz, sanidine, plagioclase?, clay, maghemite, (calcite)	2	0.23	0.03
1R-1, 90 cm	0.90	calcite, opal-A, (feldspar)	52	6.39	0.08
2R-1, 25 cm	9.75		23		
2R-1, 39 cm	9.89		27	3.73	0.51
2R-1, 90 cm	10.40	calcite, opal-A	73		
3R-1, 90 cm	19.50	calcite	83	10.08	0.07
4R-1, 90 cm	28.80	calcite, opal-A	71	8.53	0.02
5R-CC, 26 cm	37.46	calcite, (opal-A, feldspar)	77		
6R-1, 90 cm	47.40	calcite, (feldspar)	78		
7R-1, 90 cm	56.50	calcite, (opal-A)	72	8.76	0.09
8R-CC, 10 cm	64.70	calcite, (clay)	87	10.5	0
9R-1, 90 cm	74.60	calcite, (alkali feldspar)	75		
10R-1, 90 cm	84.19	calcite, clay, (alkali feldspar)	76	9.18	0.08
11R-CC, 6 cm	92.96	calcite	87		
12R-CC, 2 cm	102.51	calcite, (clay)	91	10.89	0
13R-1, 90 cm	113.09	calcite, (clay, feldspar)	81		
14R-1, 92 cm	122.60	calcite, opal-A, clay, alkali feldspar, (quartz)	51	6.16	0
15R-CC, 20 cm	131.58	calcite, (alkali feldspar, clay)			78
16R-1, 90 cm	141.89	calcite, (opal-A, alkali feldspar, clay)	64		
18R-1, 90 cm	161.19	calcite	90	10.81	0
19R-1, 90 cm	170.80	calcite, (clay)	73		
20R-1, 90 cm	180.39	calcite, (clay)	69		
21R-1, 90 cm	189.99	calcite, opal-A, (clay)	72	8.64	0.02
22R-1, 90 cm	199.60	calcite	88		
23R-1, 90 cm	209.19	calcite	84	10.04	0.01
24R-1, 90 cm	218.90	calcite, (clay, clinoptilolite, glauconite)	73		
25R-1, 90 cm	228.50	calcite, dolomite (<5%), clay, glauconite, (feldspar, chlorite)	68		
25R-5, 37 cm	233.97	calcite, dolomite (<10%), clay, (glauconite, chlorite, feldspar)	74	8.94	0
25R-5, 91 cm		dolomite (>95%), calcite			
32R3, 84 cm		dolomite, clay, (feldspar?)			

Note: Minerals in parentheses indicate the presence of only trace amounts.

Table T5. Hole 1140A basement units.

Unit	Rock type	Top (cm)	Depth (mbsf)		Unit thickness‡ (m)	Recovery (m)
			Curated*	Logging†		
		183-1140A-				
1	Pillow and massive basalt	25R-6, 0	234.52	235.8	17.6	12.46
2	Pillow basalt	31R-1, 0	270.50	253.4	19.3	1.27
3	Pillow basalt	31R-1, 134	271.84	272.7	10.3	3.44
4	Dolomite and dolomitic nannofossil chalk	32R-3, 43	278.63	283.0	1.3	1.00
5	Massive (and pillow?) basalt	32R-4, 0	279.66	284.3	14.3	7.86
6	Pillow and massive basalt	34R-4, 0	298.20	298.6	>24.0	17.37

Notes: * = based on curated lengths of recovered core. † = based on downhole logging data and core-log integration. ‡ = measured using logging data.

Table T6. Petrographic summary of Site 1140 igneous units with mineralogies.

Unit number	Rock type	Drilled thickness (m)	Pillow margins	Massive interiors			Thin sections (183-1140A-)
			Phenocrysts	Phenocrysts	Groundmass	Texture	
1	Aphyric basalt*	17.6	1%-5% PL 0%-5% OL	<1% PL <1% OL	PL, CPX, OL, OPQ, GL	Ophitic, intersertal, hypohyaline	26R-1, 5-8 cm; 26R-1, 84-86 cm; 27R-2, 0-5 cm; 27R-5, 10-12 cm; 28R-3, 29-32 cm
2	Porphyritic basalt	19.3		<17% PL <4% CPX <3% OL	PL, CPX, OL, OPQ, GL	Glomeroporphyritic with intersertal or hypohyaline groundmass	31R-1, 53-57 cm; 31R-2, 16-20 cm
3	Aphyric basalt	10.3		<1% PL <1% OL	PL, CPX, OL, OPQ, GL	Ophitic, intersertal, hypohyaline	32R-1, 58-60 cm
4	Dolomite	1.3					
5	Porphyritic basalt	14.3		<10% PL <1% OL	PL, CPX, OL, OPQ, GL	Ophitic, intersertal, hypohyaline	33R-2, 78-81 cm
6	Porphyritic basalt†	23.9	<7% PL <8% CPX <1% OL	<8% PL 0%-4% CPX	PL, CPX, OPQ, GL, OL	Glomeroporphyritic with intergranular, intersertal or hyalopilitic groundmass	34R-5, 3-6 cm; 35R-4, 49-50 cm; 36R-3, 119-121 cm; 36R-4, 86-89 cm; 37R-1, 46-49 cm; 37R-3, 104-107 cm

Notes: * = porphyritic in the pillow margins; † = the proportion of phenocrysts decreases downward and the basalt becomes locally aphyric. PL = plagioclase, CPX = clinopyroxene, OL = olivine, OPQ = opaque minerals (dominantly titanomagnetite), GL = glass.

Table T7. X-ray fluorescence analyses of major and trace elements for Site 1140 igneous units.

Hole:	1140A	1140A	1140A	1140A	1140A	1140A	1140A	1140A	1140A	1140A	1140A
Core, section:	26R-1	27R-2	28R-3	31R-1	32R-1	33R-2	34R-5	35R-4	36R-3	37R-1	37R-3
Interval (cm):	7-10	0-5	29-32	53-57	55-57	78-81	3-6	50-52	121-124	46-49	104-108
Piece:	1	1A	1B	3B	4	3	1A	4	1H	1C	2
Unit:	1	1	1	2	3	5	6	6	6	6	6
Rock type:	Basalt	Basalt	Basalt	Basalt	Basalt	Basalt	Basalt	Basalt	Basalt	Basalt	Basalt
Depth (mbsf):	237.37	240.71	249.64	271.03	275.75	286.80	299.44	308.41	316.62	317.76	320.25
Major element oxides (wt%):											
SiO_2	49.07	48.88	48.90	49.77	49.28	49.66	50.44	50.74	49.78	50.00	49.77
TiO_2	1.48	1.48	1.47	2.36	3.16	1.40	1.53	1.53	1.52	1.55	1.54
Al_2O_3	15.62	15.59	15.65	15.08	13.79	16.48	15.52	15.36	14.76	14.85	14.77
Fe_2O_3	12.93	12.78	12.67	14.34	14.85	11.90	11.78	10.85	13.14	13.32	13.20
MnO	0.19	0.18	0.18	0.20	0.19	0.16	0.19	0.18	0.21	0.20	0.29
MgO	6.77	8.12	7.87	5.54	6.18	7.94	6.86	7.55	7.31	6.71	6.29
CaO	12.71	11.92	12.11	11.02	10.00	11.45	12.63	12.25	12.41	12.47	12.37
Na_2O	2.11	2.06	2.06	2.24	2.46	2.09	2.26	2.30	2.20	2.21	2.23
K_2O	0.38	0.03	0.04	0.82	0.62	0.03	0.16	0.21	0.17	0.16	0.53
P_2O_5	0.10	0.09	0.09	0.26	0.45	0.12	0.14	0.14	0.14	0.13	0.14
Total:	101.34	101.13	101.03	101.62	100.96	101.23	101.50	101.10	101.62	101.57	101.11
LOI:	1.84	1.62	1.01	1.12	0.72	1.46	0.92	0.97	0.82	1.04	0.92
Mg# (0.8)*:	0.56	0.61	0.61	0.49	0.51	0.62	0.59	0.63	0.58	0.55	0.54
Trace elements (ppm):											
Rb	9.5	0.8	1	10.8	3.9	0.3	0.7	1.5	0.7	0.7	11.5
Ba	56	57	67	105	155	64	64	76	64	60	111
Sr	142	129	132	259	262	126	134	138	125	127	137
Ce	BD	BD	BD	5	28	BD	BD	BD	BD	BD	BD
Nb	4.8	4.4	4.7	14.6	22.9	5.1	5	5.3	5.3	5.2	5.7
Zr	87	86	88	169	239	81	83	82	80	82	82
Y	31	32	32	33	46	31	31	31	30	31	31
V	337	325	324	354	429	330	366	378	347	353	356
Cr	301	288	293	118	57	276	209	192	191	159	172
Ni	97	96	98	64	47	79	64	71	62	58	49
Cu	150	150	151	114	118	149	168	171	160	164	154
Zn	88	86	86	107	130	89	92	92	89	88	90
Normative mineralogy: Fe^{2+} = 0.8 Fe total											
Q	0.00	0.00	0.00	1.75	2.36	0.44	1.07	1.00	0.00	0.82	0.12
Or	2.21	0.18	0.21	4.82	3.67	0.18	0.94	1.24	1.00	0.94	3.13
Ab	17.78	17.40	17.41	18.85	20.84	17.62	18.96	19.36	18.49	18.59	18.80
An	31.92	33.15	33.33	28.51	24.80	35.37	31.56	30.91	29.70	29.96	28.71
Corundum	0.00	0.00	0.00	0.00	0.00	0.00	0.00	0.00	0.00	0.00	0.00
Nepheline	0.00	0.00	0.00	0.00	0.00	0.00	0.00	0.00	0.00	0.00	0.00
Leucite	0.00	0.00	0.00	0.00	0.00	0.00	0.00	0.00	0.00	0.00	0.00
Acmite	0.00	0.00	0.00	0.00	0.00	0.00	0.00	0.00	0.00	0.00	0.00
Na metasilicate	0.00	0.00	0.00	0.00	0.00	0.00	0.00	0.00	0.00	0.00	0.00
Wo (Di)	12.61	10.55	10.89	10.08	9.16	8.54	12.43	12.01	12.75	12.81	13.22
En (Di)	6.88	6.16	6.31	5.05	4.91	5.07	7.10	7.30	7.11	6.89	6.93
Fs (Di	5.27	3.88	4.07	4.80	3.94	3.02	4.78	4.03	5.13	5.48	5.90
En (Hy)	7.80	11.90	11.59	8.63	10.45	14.57	9.81	11.39	10.76	9.65	8.66
Fs (Hy)	5.98	7.49	7.46	8.20	8.40	8.70	6.61	6.29	7.77	7.68	7.37
Ol (Fo)	1.44	1.44	1.13	0.00	0.00	0.00	0.00	0.00	0.11	0.00	0.00
Ol (Fa)	1.22	1.00	0.81	0.00	0.00	0.00	0.00	0.00	0.08	0.00	0.00
Ilmenite	2.81	2.81	2.79	4.47	6.02	2.66	2.89	2.90	2.87	2.92	2.92
Magnetite	3.75	3.71	3.68	4.15	4.32	3.45	3.40	3.14	3.79	3.85	3.83
Apatite	0.22	0.20	0.20	0.57	0.99	0.26	0.30	0.31	0.30	0.27	0.31
Total:	99.88	99.87	99.87	99.87	99.85	99.87	99.87	99.86	99.87	99.88	99.88

Notes: LOI = loss on ignition at 1025°C for 4 hr. * = (Mg# = Mg/[Mg+Fe^{2+}]), where Fe^{2+} = 0.8 Fe total. BD = below detection limit.

Table T8. Secondary minerals within basement units in Hole 1140A identified by X-ray diffraction.

Core, section, interval (cm), piece	Depth (mbsf)	Description	XRD identification
183-1140A-			
26R-1, 81-82 (Piece 1)	238.11	Open space filling in glassy margin	Calcite
26R-1, 85-86 (Piece 2)	238.15	Baked sediment in glassy margin	Calcite
26R-2, 100-103 (Piece 7)	239.49	Open space filling in glassy margin	Calcite, dolomite
28R-2, 31-32 (Piece 2)	248.63	Open space filling in glassy margin	Dolomite, calcite
28R-2, 77-78 (Piece 5)	249.09	Open space filling in glassy margin	Dolomite, calcite
31R-2, 2-4 (Piece 1)	272.02	Vesicle filling	Phillipsite
32R-1, 1-3 (Piece 1)	275.21	Prismatic crystals in vein	Phillipsite, saponite, clinoptilolite?
32R-3, 82-85	279.02	Carbonate bed (Unit 4)	Dolomite
32R-4, 1-2 (Piece 1)	279.67	Black mineral and clay in vein	Saponite, nontronite, manganite, pyrolusite
33R-1, 127-130 (Piece 13)	285.87	Pink carbonate in vein	Calcite
33R-2, 3-5 (Piece 1)	286.05	Black mineral in carbonate vein	Calcite, manganite
33R-2, 99-100 (Piece 4C)	287.01	Clay in vein	Saponite, nontronite
34R-2, 0-2 (Piece 1A)	295.60	Sulfide and clay in vein	Pyrite, saponite, nontronite
34R-3, 60-61 (Piece 1C)	297.38	Green clay in vesicles	Saponite, nontronite
34R-3, 110-112 (Piece 4)	297.88	Brown clay in vesicles	Saponite, nontronite
36R-1, 40-40 (Piece 2C)	313.10	Fibrous carbonate vein	Aragonite

Table T9. Characteristic inclinations and natural remanent magnetization intensities of discrete basalt samples from Hole 1140A.

Core, section, interval (cm)	Basement unit	Inclination (°)	NRM intensity (A/m)	Depth (mbsf)	Demagnetization range (°C)
183-1140A-					
27R-2, 83–85	1	—	3.21	241.54	TH
28R-3, 20–22	1	—	6.45	249.55	TH
32R-1, 94–96	3	52	13.1	276.14	TH 230-590
34R-1, 139–141	5	51	11.2	295.49	TH 100-620
34R-5, 10–12	6	63	12.9	299.51	TH 200-590
36R-2, 128–130	6	—	16.2	315.35	TH

Notes: Inclination = characteristic inclination determined from progressive demagnetization. NRM = natural remanent magnetization. Demagnetization range = demagnetization method and characteristic inclination is determined from the component in this range. — = no characteristic direction available. TH = thermal demagnetization.

Table T10. Index properties data from Site 1140. (**See table note.** Continued on next page.)

Core, section, interval (cm)	Depth (mbsf)	Water content (%)		Density (g/cm³)			Porosity (%)	Void ratio
		Bulk	Dry	Bulk	Dry	Grain		
183-1140A-								
1-1, 126-128	1.26	45.4	83.2	1.49	0.81	2.40	66.1	1.95
1-2, 19-21	1.69	47.6	91.0	1.47	0.77	2.42	68.2	2.15
1-3, 138-140	4.38	47.8	91.5	1.43	0.75	2.23	66.6	1.99
1-4, 25-27	4.75	49.0	96.2	1.44	0.73	2.37	69.0	2.22
2-1, 124-126	10.74	39.7	65.9	1.56	0.94	2.40	60.7	1.54
2-2, 24-26	11.24	47.5	90.3	1.40	0.74	2.11	65.1	1.86
2-3, 36-38	12.86	46.2	85.8	1.48	0.80	2.41	66.8	2.02
2-4, 40-42	14.40	46.0	85.1	1.45	0.78	2.23	65.0	1.86
3-1, 113-115	19.73	40.8	68.9	1.62	0.96	2.72	64.6	1.83
3-2, 21-23	20.31	43.3	76.4	1.50	0.85	2.32	63.4	1.73
4-1, 129-131	29.19	37.2	59.2	1.62	1.02	2.46	58.7	1.42
4-2, 22-24	29.62	37.3	59.4	1.55	0.97	2.24	56.5	1.30
5-CC, 19-21	37.39	40.4	67.9	1.54	0.92	2.34	60.8	1.55
6-1, 129-131	47.79	41.9	72.2	1.56	0.90	2.49	63.7	1.75
6-2, 99-101	48.99	42.1	72.6	1.50	0.87	2.25	61.5	1.60
7-1, 117-119	56.77	46.2	85.8	1.52	0.82	2.63	68.8	2.20
7-2, 28-30	57.38	43.2	76.0	1.50	0.85	2.33	63.4	1.73
9-1, 113-115	74.83	45.4	83.3	1.49	0.81	2.38	66.0	1.94
10-1, 113-115	84.43	46.4	86.4	1.52	0.82	2.63	68.9	2.22
13-1, 96-98	113.16	41.2	70.1	1.61	0.95	2.70	64.8	1.84
14-1, 98-100	122.68	51.9	108.0	1.45	0.70	2.65	73.6	2.79
14-2, 143-145	124.63	53.2	113.5	1.45	0.68	2.72	75.1	3.01
14-3, 117-119	125.87	52.7	111.3	1.44	0.68	2.62	74.0	2.85
16-1, 21-23	141.21	54.7	120.8	1.41	0.64	2.61	75.5	3.08
17-1, 30-32	151.00	45.1	82.3	1.56	0.85	2.71	68.5	2.18
18-1, 100-102	161.30	36.4	57.3	1.74	1.11	2.92	62.0	1.63
18-2, 70-72	162.50	38.0	61.3	1.68	1.04	2.75	62.3	1.65
18-3, 72-74	164.02	42.7	74.5	1.60	0.91	2.73	66.5	1.99
18-4, 35-37	165.15	38.3	62.2	1.69	1.04	2.85	63.4	1.73
18-5, 43-45	166.73	38.5	62.6	1.69	1.04	2.85	63.5	1.74
18-6, 67-69	168.47	44.6	80.6	1.56	0.87	2.71	68.1	2.13
18-7, 16-18	169.46	42.2	73.0	1.60	0.93	2.71	65.9	1.93
19-1, 99-101	170.89	43.7	77.5	1.58	0.89	2.74	67.4	2.07
19-2, 115-117	172.55	50.4	101.7	1.47	0.73	2.66	72.5	2.64
19-3, 104-106	173.94	47.4	90.0	1.55	0.81	2.86	71.5	2.51
19-4, 117-119	175.57	43.2	76.1	1.60	0.91	2.82	67.7	2.09
19-5, 106-108	176.96	46.7	87.5	1.53	0.82	2.71	69.9	2.32
19-6, 106-108	178.46	47.4	90.2	1.53	0.81	2.79	71.1	2.46
19-7, 40-42	179.30	42.4	73.7	1.62	0.94	2.86	67.3	2.06
20-1, 114-116	180.64	44.3	79.5	1.58	0.88	2.78	68.4	2.16
20-2, 86-88	181.86	45.0	81.8	1.56	0.86	2.70	68.3	2.16
20-3, 130-132	183.80	50.4	101.5	1.50	0.75	2.85	73.8	2.82
20-4, 28-30	184.28	39.9	66.5	1.65	0.99	2.78	64.3	1.80
21-1, 134-136	190.44	39.2	64.5	1.64	1.00	2.69	62.9	1.70
21-2, 53-55	191.13	41.0	69.4	1.61	0.95	2.67	64.4	1.81
21-3, 56-58	192.66	46.5	87.1	1.54	0.83	2.76	70.1	2.35
21-4, 73-75	194.33	46.9	88.3	1.52	0.81	2.64	69.5	2.28
21-5, 106-108	196.16	43.3	76.5	1.56	0.88	2.61	66.0	1.95
22-1, 111-113	199.81	41.3	70.4	1.60	0.94	2.66	64.7	1.83
22-2, 52-54	200.72	40.4	67.8	1.63	0.97	2.72	64.3	1.80
22-3, 66-68	202.36	39.8	66.0	1.64	0.99	2.71	63.6	1.75
22-4, 131-133	204.51	42.4	73.7	1.59	0.92	2.70	66.0	1.94
22-6, 102-104	207.22	42.5	73.9	1.59	0.92	2.69	66.0	1.94
23-2, 124-126	211.04	34.6	53.0	1.74	1.14	2.75	58.7	1.42
23-3, 91-93	212.21	34.2	52.0	1.73	1.14	2.69	57.8	1.37
23-4, 82-84	213.62	36.8	58.2	1.70	1.07	2.75	61.0	1.56
23-5, 140-142	215.70	37.5	60.1	1.68	1.05	2.74	61.7	1.61
23-6, 36-38	216.16	33.1	49.4	1.76	1.18	2.71	56.7	1.31
24-4, 30-32	222.80	29.4	41.6	1.81	1.28	2.67	52.0	1.08
25-1, 114-116	228.74	26.8	36.7	1.87	1.37	2.69	49.1	0.96
25-2, 130-132	230.40	25.4	34.1	1.91	1.42	2.71	47.4	0.90
25-3, 133-135	231.93	30.2	43.2	1.82	1.27	2.75	53.7	1.16
25-4, 143-145	233.53	22.3	28.7	2.01	1.56	2.77	43.7	0.78
25-5, 47-49	234.07	26.5	36.0	1.91	1.41	2.78	49.4	0.98
25-6, 60-62	235.12	3.0	3.1	2.78	2.70	2.94	8.1	0.09
26-1, 51-53	237.81	2.2	2.2	2.80	2.73	2.91	5.9	0.06

Table T10 (continued).

Core, section, interval (cm)	Depth (mbsf)	Water content (%)		Density (g/cm^3)			Porosity (%)	Void ratio
		Bulk	Dry	Bulk	Dry	Grain		
26-2, 15-17	238.64	2.2	2.2	2.83	2.77	2.95	6.0	0.06
27-1, 14-16	239.44	1.9	2.0	2.80	2.74	2.90	5.2	0.06
27-2, 83-85	241.54	2.2	2.3	2.79	2.73	2.91	6.1	0.07
27-3, 75-77	242.74	2.0	2.1	2.83	2.77	2.94	5.6	0.06
27-4, 4-6	243.46	2.1	2.1	2.87	2.81	2.99	5.8	0.06
27-5, 41-43	245.22	2.0	2.1	2.79	2.74	2.90	5.6	0.06
28-1, 10-12	247.00	1.8	1.9	2.80	2.75	2.90	5.0	0.05
28-3, 20-22	249.55	1.6	1.6	2.86	2.82	2.95	4.3	0.05
31-1, 16-18	270.66	3.1	3.2	2.68	2.59	2.82	8.1	0.09
32-1, 94-96	276.14	5.8	6.2	2.65	2.49	2.93	15.0	0.18
32-2, 60-62	277.30	5.5	5.8	2.66	2.51	2.93	14.3	0.17
32-3, 50-52	278.70	13.9	16.2	2.28	1.96	2.84	31.0	0.45
32-3, 68-70	278.88	23.4	30.6	1.99	1.52	2.79	45.4	0.83
32-3, 82-84	279.02	17.8	21.7	2.15	1.77	2.83	37.4	0.60
32-3, 96-97	279.16	18.7	23.1	2.09	1.70	2.75	38.2	0.62
32-3, 120-122	279.40	21.5	27.4	2.06	1.62	2.85	43.3	0.76
32-3, 133-135	279.53	18.4	22.5	2.13	1.74	2.80	38.1	0.62
33-2, 80-82	286.82	4.2	4.4	2.70	2.59	2.91	11.2	0.13
33-3, 82-84	288.20	9.1	10.1	2.51	2.28	2.94	22.4	0.29
34-1, 101-103	295.11	5.1	5.4	2.70	2.56	2.96	13.5	0.16
34-2, 38-40	295.98	4.7	4.9	2.73	2.61	2.98	12.4	0.14
34-3, 71-73	297.49	3.6	3.7	2.74	2.64	2.92	9.5	0.11
34-4, 33-35	298.53	3.7	3.9	2.80	2.70	3.00	10.2	0.11
34-5, 5-7	299.46	2.6	2.7	2.79	2.72	2.92	7.1	0.08
34-6, 52-54	301.41	3.6	3.7	2.72	2.62	2.90	9.5	0.11
35-1, 105-107	304.55	2.8	2.9	2.77	2.70	2.92	7.7	0.08
35-2, 11-13	305.08	2.9	3.0	2.78	2.69	2.92	7.8	0.09
35-3, 12-14	306.59	1.9	2.0	2.91	2.85	3.02	5.5	0.06
35-4, 41-43	308.32	2.4	2.5	2.83	2.77	2.97	6.7	0.07
36-1, 35-37	313.05	2.1	2.2	2.95	2.89	3.07	6.1	0.07
36-2, 2-4	314.09	2.9	3.0	2.82	2.74	2.98	8.1	0.09
36-3, 44-46	315.85	1.6	1.6	2.89	2.84	2.98	4.5	0.05
36-4, 15-17	317.06	1.6	1.6	2.86	2.82	2.95	4.3	0.05
37-1, 8-10	317.38	2.0	2.0	2.82	2.77	2.93	5.4	0.06
37-3, 23-25	319.44	2.3	2.3	2.85	2.78	2.97	6.3	0.07
37-4, 16-18	320.64	2.2	2.2	2.82	2.76	2.93	5.9	0.06

Note: This table is also available in **ASCII format.**

Table T11. Compressional wave velocity from discrete measurements, Site 1140. (**See table note.** Continued on next page.)

Core, section, interval (cm)	Depth (mbsf)	Direction	Velocity (m/s)
183-1140A-			
1R-1, 127	1.27	LZ	1515
1R-1, 127	1.27	LY	1510
1R-1, 128	1.28	LX	1498
1R-2, 19	1.69	LZ	1521
1R-2, 19	1.69	LX	1491
1R-2, 19	1.69	LY	1520
1R-3, 138	4.38	LZ	1516
1R-3, 139	4.39	LX	1493
1R-3, 139	4.39	LY	1514
1R-4, 26	4.76	LZ	1524
1R-4, 26	4.76	LY	1516
2R-1, 37	9.87	LY	1526
2R-1, 37	9.87	LZ	1521
2R-1, 126	10.76	LZ	1518
2R-1, 126	10.76	LY	1523
2R-2, 25	11.25	LZ	1514
2R-3, 37	12.87	LZ	1518
2R-3, 37	12.87	LY	1519
2R-3, 89	13.39	LZ	1504
2R-3, 90	13.40	LY	1515
2R-4, 41	14.41	LY	1515
2R-4, 42	14.42	LZ	1520
2R-4, 118	15.18	LZ	1514
2R-4, 118	15.18	LY	1527
3R-1, 38	18.98	LZ	1517
3R-1, 39	18.99	LY	1519
3R-1, 113	19.73	LZ	1521
3R-1, 114	19.74	LY	1521
3R-2, 22	20.32	LY	1504
3R-2, 24	20.34	LZ	1512
4R-1, 47	28.37	LX	1617
4R-1, 130	29.20	LX	1641
4R-2, 23	29.63	LX	1630
5R-CC, 20	37.40	LX	1635
6R-1, 43	46.93	LX	1637
6R-1, 130	47.80	LX	1636
6R-2, 43	48.43	LX	1630
6R-2, 100	49.00	LX	1623
7R-1, 20	55.80	LX	1787
7R-1, 20	55.80	LX	1659
7R-2, 29	57.39	LX	1636
9R-1, 42	74.12	LX	1641
9R-1, 42	74.12	LX	1630
10R-1, 114	84.44	LX	1639
13R-1, 97	113.17	LX	1638
13R-2, 45	114.15	LX	1654
14R-1, 35	122.05	LX	1680
14R-1, 101	122.71	LX	1686
14R-2, 14	123.34	LX	1656
14R-2, 144	124.64	LX	1659
14R-3, 59	125.29	LX	1647
14R-3, 118	125.88	LX	1638
16R-1, 26	141.26	LX	1718
16R-1, 117	142.17	LX	1711
17R-1, 32	151.02	LX	1743
18R-1, 29	160.59	LX	1770
18R-1, 120	161.50	LX	1803
18R-2, 53	162.33	CY	1852
18R-2, 53	162.33	CZ	1920
18R-3, 21	163.51	CY	1802
18R-3, 21	163.51	CZ	1838
18R-3, 71	164.01	CY	1815
18R-3, 71	164.01	CZ	1796
18R-4, 36	165.16	CZ	1703
18R-5, 44	166.74	CY	1622
18R-5, 44	166.74	CZ	1670
18R-5, 130	167.60	CY	1583
18R-5, 130	167.60	CZ	1618
18R-6, 30	168.10	CY	1594
18R-6, 30	168.10	CZ	1648
18R-6, 68	168.48	CY	1606
18R-6, 68	168.48	CZ	1621
18R-7, 17	169.47	CY	1601
18R-7, 17	169.47	CZ	1657
19R-1, 41	170.31	CZ	1606
19R-1, 100	170.90	CZ	1604
19R-2, 46	171.86	CY	1569
19R-2, 46	171.86	CZ	1572
19R-2, 116	172.56	CY	1565
19R-2, 116	172.56	CZ	1572
19R-3, 105	173.95	CY	1570
19R-3, 105	173.95	CZ	1577
19R-4, 33	174.73	CY	1554
19R-4, 33	174.73	CZ	1590
19R-4, 117	175.57	CY	1602
19R-4, 117	175.57	CZ	1617
19R-5, 63	176.53	CY	1595
19R-5, 63	176.53	CZ	1587
19R-5, 107	176.97	CY	1581
19R-5, 107	176.97	CZ	1603
19R-6, 29	177.69	CY	1584
19R-6, 29	177.69	CZ	1625
19R-6, 107	178.47	CY	1617
19R-6, 107	178.47	CZ	1652
19R-7, 41	179.31	CY	1633
19R-7, 41	179.31	CZ	1660
20R-1, 29	179.79	CY	1619
20R-1, 29	179.79	CZ	1648
20R-1, 115	180.65	CY	1588
20R-1, 115	180.65	CZ	1596
20R-2, 50	181.50	CY	1593
20R-2, 50	181.50	CZ	1610
20R-2, 86	181.86	CY	1604
20R-2, 86	181.86	CZ	1639
20R-3, 46	182.96	CZ	1595
20R-3, 132	183.82	CY	1608
20R-4, 30	184.30	CY	1614
20R-4, 30	184.30	CZ	1691
21R-1, 16	189.26	CY	1621
21R-1, 16	189.26	CZ	1623
21R-1, 135	190.45	CY	1666
21R-1, 135	190.45	CZ	1677
21R-2, 54	191.14	CY	1598
21R-2, 54	191.14	CZ	1639
21R-3, 58	192.68	CY	1592
21R-3, 58	192.68	CZ	1625
21R-3, 120	193.30	CY	1578
21R-3, 120	193.30	CZ	1608
21R-4, 74	194.34	CY	1597
21R-4, 74	194.34	CZ	1600
21R-5, 21	195.31	CY	1645
21R-5, 21	195.31	CZ	1687
21R-5, 107	196.17	CY	1608
21R-5, 107	196.17	CZ	1634
21R-6, 17	196.77	CY	1609
21R-6, 17	196.77	CZ	1652
22R-1, 112	199.82	CY	1611
22R-1, 112	199.82	CZ	1681
22R-2, 53	200.73	CY	1611
22R-2, 53	200.73	CZ	1645
22R-3, 67	202.37	CY	1610
22R-3, 67	202.37	CZ	1655
22R-4, 21	203.41	CY	1628
22R-4, 21	203.41	CZ	1668
22R-4, 132	204.52	CY	1639

Table T11 (continued).

Core, section, interval (cm)	Depth (mbsf)	Direction	Velocity (m/s)
22R-4, 132	204.52	CZ	1650
22R-5, 39	205.09	CY	1643
22R-5, 39	205.09	CZ	1659
22R-5, 107	205.77	CY	1655
22R-5, 107	205.77	CZ	1713
22R-6, 23	206.43	CY	1741
22R-6, 23	206.43	CZ	1810
22R-6, 103	207.23	CY	1662
22R-6, 103	207.23	CZ	1694
23R-1, 31	208.61	CY	1729
23R-1, 31	208.61	CZ	1825
23R-1, 93	209.23	CZ	1731
23R-1, 93	209.23	CZ	1700
23R-2, 35	210.15	CY	1721
23R-2, 35	210.15	CZ	1721
23R-2, 125	211.05	CY	1759
23R-2, 125	211.05	CZ	1782
23R-3, 20	211.50	CZ	1799
23R-3, 92	212.22	CY	1798
23R-3, 92	212.22	CZ	1841
23R-4, 10	212.90	CY	1789
23R-4, 10	212.90	CZ	1806
23R-4, 83	213.63	CY	1767
23R-4, 83	213.63	CZ	1769
23R-5, 15	214.45	CY	1891
23R-5, 15	214.45	CZ	1990
23R-5, 141	215.71	CY	1731
23R-5, 141	215.71	CZ	1758
23R-6, 37	216.17	CY	1683
23R-6, 37	216.17	CZ	1760
24R-1, 39	218.39	CY	1892
24R-1, 39	218.39	CZ	1869
24R-1, 110	219.10	CY	1900
24R-1, 110	219.10	CZ	1950
24R-2, 68	220.18	CY	1872
24R-2, 68	220.18	CZ	1867
24R-2, 139	220.89	CY	1866
24R-2, 139	220.89	CZ	1775
24R-3, 39	221.39	CY	1873
24R-3, 39	221.39	CZ	1854
24R-3, 113	222.13	CY	1882
24R-3, 113	222.13	CZ	1832
25R-1, 27	227.87	CY	1952
25R-1, 27	227.87	CZ	1943
25R-1, 115	228.75	CY	2018
25R-1, 115	228.75	CZ	1910
25R-2, 27	229.37	CY	1956
25R-2, 27	229.37	CZ	1944
25R-2, 131	230.41	CY	1968
25R-2, 131	230.41	CZ	2019
25R-3, 137	231.97	CY	1893
25R-3, 137	231.97	CZ	1860
25R-4, 18	232.28	CY	1903
25R-4, 18	232.28	CZ	1928
25R-4, 145	233.55	CY	2013
25R-4, 145	233.55	CZ	1941
25R-5, 48	234.08	CY	1875
25R-5, 48	234.08	CZ	1870
25R-6, 61	235.13	MX	5518
26R-1, 52	237.82	MX	6859
26R-2, 16	238.65	MX	6149
27R-1, 15	239.45	MX	6212
27R-2, 84	241.55	MX	5819
27R-3, 76	242.75	MX	6350
27R-4, 5	243.47	MX	5484
27R-5, 42	245.23	MX	5917
28R-1, 11	247.01	MX	6303
28R-3, 21	249.56	MX	6551
28R-3, 73	250.08	MX	6188
31R-1, 17	270.67	MX	5599
31R-1, 50	271.00	MX	5606
31R-1, 70	271.20	MX	5783
31R-1, 82	271.32	MX	5918
32R-2, 61	277.31	MX	5304
32R-2, 77	277.47	MX	4758
33R-2, 61	286.63	MX	5637
33R-2, 105	287.07	MX	6103
33R-3, 66	288.04	MX	5362
34R-1, 102	295.12	MX	5233
34R-1, 140	295.50	MX	5665
34R-2, 39	295.99	MX	5608
34R-2, 87	296.47	MX	5099
34R-3, 72	297.50	MX	5182
34R-4, 34	298.54	MX	6574
34R-5, 11	299.52	MX	6386
34R-6, 53	301.42	MX	5838
35R-1, 103	304.53	MX	6409
35R-2, 25	305.22	MX	6241
35R-4, 4	307.95	MX	6665
36R-1, 36	313.06	MX	6474
36R-2, 3	314.10	MX	6420
36R-2, 129	315.36	MX	6346
36R-3, 45	315.86	MX	5898
36R-4, 20	317.11	MX	6703
37R-1, 9	317.39	MX	6829
37R-1, 90	318.20	MX	6177
37R-3, 24	319.45	MX	6227
37R-4, 17	320.65	MX	6180

Notes: Type of samples is denoted by prefix: L = split-core section with core liner, C = oriented cubes, M = oriented minicore, and no prefix = split core sections without core liner. The directions of the velocity measurements are represented by Z (along the core), Y (across the core), and X (into the core). This table is also available in **ASCII format.**

Table T12. Thermal conductivity values for Site 1140.

Core, section, interval (cm)	Depth (mbsf)	Thermal conductivity (W/[m·K])
183-1140A-		
2R-3, 75	13.25	0.67
3R-1, 75	19.35	0.82
4R-2, 24	29.64	0.90
6R-2, 60	48.60	0.92
7R-2, 28	57.38	0.96
9R-1, 75	74.45	0.93
10R-1, 75	84.05	0.90
13R-1, 75	112.95	0.96
14R-2, 75	123.95	0.87
15R-3, 75	141.75	0.81
16R-1, 75	151.30	0.79
17R-1, 60	164.15	0.96
18R-3, 85	173.65	0.98
19R-3, 75	183.25	0.91
20R-3, 75	192.85	0.95
22R-3, 75	202.45	0.97
23R-2, 75	210.55	0.85
25R-6, 50-64	235.09	1.71
26R-2, 60-78	239.18	1.76
27R-1, 118-140	240.59	1.51
27R-3, 45-66	242.55	2.06
28R-3, 112-124	250.53	1.49
31R-1, 95-107	271.51	1.47
32R-2, 32-50	277.11	1.78
33R-2, 33-47	286.42	1.61
33R-3, 10-25	287.56	1.55
34R-1, 111-122	295.27	1.58
34R-2, 92-109	296.61	1.49
34R-4, 70-80	298.95	2.15
35R-1, 1-15	303.58	1.68
35R-2, 60-70	305.62	1.58
36R-1, 122-137	314.00	1.71
36R-4, 30-43	317.28	1.68
37R-1, 18-40	317.59	1.72
37R-4, 12-19	320.64	1.73

Notes: Depth = bottom depth of sample interval. This table is also available in **ASCII format.**

Table T13. Carbon, nitrogen, sulfur, and hydrogen analyses of sediments from Site 1140.

Hole, core, section, interval (cm)	Depth (mbsf)	$CaCO_3$ (wt%)	IC (wt%)	OC (wt%)	N (wt%)	S (wt%)	H (wt%)
183-1140A-							
1R-1, 11–12	0.11-0.12	1.69	0.20	0.03	0.02	0.04	0.47
1R-1, 89–90	0.89-0.90	52.49	6.30	0.08	0.02	0.13	0.47
2R-1, 24–25	9.74-9.75	22.85	2.74				
2R-1, 38–39	9.88-9.89	26.76	3.21	0.51	0.06	0.22	0.85
2R-1, 89–90	10.39-10.40	72.54	8.71				
3R-1, 89–90	19.49-19.50	83.32	10.00	0.07	0.01	0.26	0.10
4R-1, 89–90	28.79-28.80	70.83	8.50	0.02	0.01	0.23	0.29
5R-CC, 25–26	37.45-37.46	76.58	9.19				
6R-1, 89–90	47.39-47.40	77.90	9.35				
7R-1, 89–90	56.49-56.50	72.25	8.67	0.09	BD	0.07	0.25
8R-CC, 9–10	64.69-64.70	87.46	10.50	BD	BD	0.10	0.08
9R-1, 89–90	74.59-74.60	75.09	9.01				
10R-1, 89–90	84.19-84.20	75.80	9.10	0.08	BD	0.10	0.19
11R-CC, 5–6	92.95-92.96	87.09	10.46				
12R-CC, 1–2	102.51-102.52	90.70	10.89	BD	BD	BD	BD
13R-1, 89–90	113.09-113.10	80.79	9.70				
14R-1, 89–90	122.59-122.60	51.30	6.16	BD	0.01	0.09	0.43
15R-CC, 18–20	131.58-131.60	77.92	9.35				
16R-1, 89–90	141.89-141.90	64.35	7.73				
18R-1, 89–90	161.19-161.20	90.06	10.81	BD	BD	0.06	0.06
19R-1, 89–90	170.79-170.80	72.97	8.76				
20R-1, 89–90	180.39-180.40	68.68	8.25				
21R-1, 89–90	189.99-190.00	71.75	8.61	0.02	0.01	0.04	0.24
22R-1, 89–90	199.59-199.60	87.69	10.53				
23R-1, 89–90	209.19-209.20	83.50	10.02	0.01	BD	BD	0.09
24R-1, 89–90	218.89-218.90	73.29	8.80				
25R-1, 89–90	228.49-228.50	67.62	8.12				
25R-5, 35–37	233.95-233.97	74.47	8.94	BD	BD	BD	0.25
32R-3, 82–85	279.02-279.05	85.645	10.282				

Note: This table is also available in **ASCII format.** BD = below detection limit.

Table T14. Carbon, nitrogen, sulfur, and hydrogen analyses of basalts from Site 1140.

Core, section, piece, interval (cm)	Depth (mbsf)	TC (wt%)	N (wt%)	S (wt%)	H (wt%)
183-1140A-					
26R-1 (Piece 1, 7–13)	237.37-237.40	0.14	0.00	0.01	0.17
27R-2 (Piece 1A, 0–9)	240.71-240.76	0.01	0.00	0.05	0.21
28R-3 (Piece 1B, 29–32)	249.64-249.67	0.02	0.00	0.04	0.14
31R-1 (Piece 3B, 53–71)	271.03-271.07	0.01	0.00	0.03	0.10
32R-1 (Piece 4, 55–60)	275.75-275.77	0.02	0.01	0.15	0.12
33R-2 (Piece 3, 78–82)	286.80-286.83	0.03	0.00	0.02	0.17
34R-5 (Piece 1A, 3–7)	299.44-299.47	0.01	0.00	0.03	0.09
35R-4 (Piece 4, 50–52)	308.41-308.43	0.03	0.00	0.04	0.08
36R-3 (Piece 1H, 121–124)	316.62-316.65	0.01	0.00	0.04	0.12
37R-1 (Piece 1C, 46–49)	317.76-317.79	0.02	0.01	0.05	0.11
37R-3 (Piece 2, 104–108)	320.25-320.29	0.08	0.01	0.00	0.05

Note:This table is also available in **ASCII format.**

Table T15. Shotpoints and the measured one-way traveltimes of the check-shot survey.

Depth (mbsf)	Depth (mbrf)	Transit time (ms)	Interval velocity (m/s)
97.7	2503.7	3370.26	1660.46
137.7	2543.7	3418.44	1830.26
234.7	2640.7	3524.44	5454.01
240.7	2646.7	3526.64	4546.31
250.8	2656.8	3531.08	2296.6
257.8	2663.8	3537.17	3678.02
269.7	2675.7	3543.64	5019.95
283.8	2689.8	3549.26	4173.91
295.5	2701.5	3554.87	3595.61
307.7	2713.7	3561.65	0

Table T16. Summary of logging operations.

Date (January 1999)	Time (UTC)	Logging operations
26	1800	Hole preparation complete, rig up wireline.
	0900	Rig into hole with HNGS-APS-HLDS-DITE(+TAP).
	2025	Uplog at 900 ft/hr from 322.5 mbsf to seafloor. Rig into hole to total depth.
	2155	Repeat uplog at 900 ft/hr from 322.5 to 227 mbsf. Rig out of hole.
	2330	Tool on rig floor.
27	0030	Rig-up NGT-LSS-FMS.
	0100	Rig into hole with NGT-LSS-FMS.
	0220	Uplog at 900 ft/hr from 322.5 mbsf to the end of pipe. Rig down hole for repeat run.
	0255	Repeat uplog at 900 ft/hr from 322.5 mbsf to end of pipe. Pull rig out of hole.
	0430	Tools back on rig floor.
	0530	Start rig-up WST.
	0555	Rig into hole with WST.
	0655	Performed multiple shots at ten stations; source offset is 49.0 m.
	0845	End of shots. Pull tool out of hole.
	0945	End of logging operations.

Note: UTC = Universal Time Coordinated. Drillers total depth = 2728.5 mbsf, water depth = 2406 mbrf, end of pipe = 80 mbsf. Tool acronyms are defined in Table T14, p. 93, in the "Explanatory Notes" chapter.

Table T17. Depths of basement unit boundaries and within unit structural and lithologic characteristics based on Formation MicroScanner data.

Unit	Rock type	Depth to top (mbsf)	Thickness (m)	Recovered in core (m)	Recovery (%)
1	Pillow basalt	235.8	4.6	3.52	77
1	Massive basalt	240.4	4.6	4.21	92
1	Pillow basalt	245.0	6.0	4.73	79
1	Basalt + sediments	251.0	2.4	0	0
2	Sediments	253.4	2.1	0	0
2	Pillow basalt	255.5	5.0	0	0
2	Massive basalt	260.5	1.3	0	0
2	Pillow basalt	261.8	10.9	1.27	12
3	Sediments	272.7	2.4	0.03	1
3	Pillow basalts	275.1	7.9	3.41	43
4	Sediments	283.0	1.3	1.00	77
5A	Pillow basalt	284.3	1.7	0.78*	46*
5B	Sediments	286.0	2.0	0	0
5C	Massive basalt	288.0	10.6	7.08*	67*
6	Sediments	298.6	1.1	0.05	5
6	Massive basalt	299.7	1.3	0.59	45
6	Pillow basalt	301.0	14.0	9.22	66
6	Massive basalt	315.0	3.0	3.22	107
6	Pillow basalt	318.0	>5.0	3.36	<67

Notes: The location of boundaries identified from FMS may change slightly with further data processing post cruise. * = It is not clear if any of Subunit 5A was recovered. The thickness calculated for Subunits 5A and 5C is based on the assumption that if there is a break in the lava flow, it might be in Section 183-1140A-33R-1, 36-39 cm. The altered layer (orange color) suggests a separation of basement Unit 5 into Subunits 5A and 5C. For more details, see "**Physical Volcanology,**" p. 12, and "**Igneous Petrology and Geochemistry**," p. 16.